

**COMPUTATIONAL AND EXPERIMENTAL INVESTIGATION OF
REINFORCED POLYMERS FOR MATERIAL EXTRUSION
ADDITIVE MANUFACTURING**

A Thesis
Presented to
The Academic Faculty

by

Narumi Watanabe

In Partial Fulfillment
of the Requirements for the Degree
Master of Science in Mechanical Engineering in the
George W. Woodruff School of Mechanical Engineering

Georgia Institute of Technology
December 2016

COPYRIGHT 2016 BY NARUMI WATANABE

**COMPUTATIONAL AND EXPERIMENTAL INVESTIGATION OF
REINFORCED POLYMERS FOR MATERIAL EXTRUSION
ADDITIVE MANUFACTURING**

Approved by:

Dr. David W. Rosen, Co-Chair
George W. Woodruff School of Mechanical Engineering
Georgia Institute of Technology

Dr. Meisha L. Shofner, Co-Chair
School of Materials Science and Engineering
Georgia Institute of Technology

Dr. Suresh K. Sitaraman
George W. Woodruff School of Mechanical Engineering
Georgia Institute of Technology

Date Approved: December 9, 2016

To my family and Brian

ACKNOWLEDGEMENTS

I would like to thank my advisors, Dr. David W. Rosen and Dr. Meisha L. Shofner, for their guidance and support over the past two years. The completion of my Master's thesis would not have been possible without their encouragement and confidence in my abilities. I would also like to thank my committee member, Dr. Suresh K. Sitaraman, for his time and feedback.

I would like to acknowledge IMERYS Filtration & Performance Additives for their financial support and Dr. Neil Treat for providing valuable guidance and resources for this research.

I would also like to thank Dr. Rosen's and Dr. Shofner's lab members, Dr. Mahmoud Dinar, Emily Fitzharris, J.T. Hansen, Jonathan Holmes, Chad Hume, Cameron Irvin, Dr. Namin Jeong, Dr. Jane Kang, Matt Orr, Dr. Sang-in Park, Paula Xian, Ying Zhang, Changxuan Zhao and Xiayun Zhao, for their supports and friendships. Thank you for making the office an enjoyable place to work and best of luck with your future endeavors.

In addition, I would like to express my appreciation to Dr. Donggang Yao for allowing me to use his capillary rheometer, Dr. Shannon Yee and Dr. Thomas Bougher for allowing me to use their transient plane source thermal constants analyzer at the Heat Lab, and Dr. Jason Nadler and Katie Copenhaver for allowing me to use a dilatometer at the Georgia Tech Research Institute.

Finally, I wish to express my endless gratitude to my family and friends for their unconditional love and support. I am extremely grateful to my mother, my father, my

brother and my boyfriend for believing in me and teaching me to live my life without regrets.

TABLE OF CONTENTS

	Page
ACKNOWLEDGEMENTS	IV
LIST OF TABLES	X
LIST OF FIGURES	XII
LIST OF ABBREVIATIONS.....	XVI
SUMMARY	XVII
CHAPTER 1 INTRODUCTION AND MOTIVATION	1
1.1 Introduction.....	1
1.2 Motivation.....	4
1.3 Research Question and Hypothesis.....	6
1.4 Organization of This Thesis.....	7
CHAPTER 2 MATERIAL EXTRUSION ADDITIVE MANUFACTURING TECHNOLOGY AND LITERATURE REVIEW	8
2.1 Introduction.....	8
2.2 Material Extrusion Additive Manufacturing Technology	8
2.2.1 Basic Principles.....	8
2.2.2 Additive Manufacturing Machine.....	9
2.2.3 Materials and Costs.....	11
2.2.3.1 Materials	11
2.2.3.2 Material Costs.....	16
2.3 Material Extrusion Additive Manufacturing with Polypropylene	17
2.4 Process Modeling of Material Extrusion Additive Manufacturing	21

2.4.1	Material Flow	21
2.4.2	Melt Properties.....	23
2.4.3	Pressure Drop.....	24
2.4.4	Road Deposition and Spreading.....	25
2.4.5	Road Cooling and Bonding.....	28
2.5	Mechanical Properties.....	29
2.6	Summary.....	34
CHAPTER 3 MATERIAL PROCESSING, MATERIAL COMPOSITIONS AND MATERIAL CHARACTERIZATIONS		35
3.1	Introduction.....	35
3.2	Material Processing.....	35
3.3	Material Compositions.....	39
3.4	Material Characterizations	41
3.4.1	Viscosity	41
3.4.2	Coefficient of Thermal Expansion.....	43
3.4.3	Thermal Conductivity	47
3.5	Summary.....	50
CHAPTER 4 MATERIAL EXTRUSION PROCESS SIMULATION MODELS		52
4.1	Introduction.....	52
4.2	Process Simulation Model Development.....	52
4.2.1	Melt Flow in the Liquefier Chamber	54
4.2.2	Extrusion through the Nozzle	57
4.2.3	Die Swell at the Nozzle Exit.....	60

4.2.4	First Layer Deposition and Cooling.....	66
4.2.5	Second Layer Deposition and Cooling	75
4.2.6	Residual Stress/Warpage	80
4.3	Parametric Studies and Validations of Warpage Process Simulation Model	83
4.3.1	Geometry Discrepancies between Simulation Models and Experiments ...	83
4.3.2	Process Variable Settings.....	86
4.3.2.1	Deposition Temperature	87
4.3.2.2	Deposition Speed.....	89
4.3.2.3	Layer Height	91
4.3.3	Material Properties.....	92
4.3.3.1	Coefficient of Thermal Expansion	93
4.3.3.2	Thermal Conductivity.....	94
4.4	Summary.....	95
CHAPTER 5 MECHANICAL PROPERTY ANISOTROPY AND BONDING		
STRENGTH.....		
5.1	Introduction.....	97
5.2	Scanning Electron Microscope (SEM)	97
5.3	Mechanical Property Anisotropy	99
5.3.1	Deposition Temperature.....	102
5.3.2	Layer Height	108
5.4	Summary.....	113
CHAPTER 6 CLOSURE AND CONTRIBUTIONS		
6.1	Introduction.....	115

6.2	Answering the Research Questions	115
6.2.1	Research Question 1	115
6.2.2	Research Question 2	117
6.3	Contributions	119
6.4	Future Work.....	120
	REFERENCES	121

LIST OF TABLES

	Page
Table 2.1 Key characteristics of Stratasys commercially available thermoplastics	12
Table 2.2 Key characteristics of other available thermoplastics.....	14
Table 2.3 Costs of thermoplastics in pellets and filaments.....	16
Table 2.4 Characteristic shrinkages of thermoplastics	19
Table 2.5 CTE and thermal conductivity for ABS with and without carbon fiber reinforcement	20
Table 2.6 Part distortions of bar specimens printed with ABS with and without carbon fiber reinforcement.....	20
Table 3.1 Process variable settings for polypropylene filament extrusion	38
Table 3.2 Test specimens and percent crystallinities of candidate neat polypropylenes..	40
Table 3.3 Viscosity expressions of Polypropylenes C and C1	42
Table 4.1 Process variable settings	54
Table 4.2 Process variable settings for parametric studies	86
Table 4.3 Experimental and simulation model warpage with varying deposition temperature	88
Table 4.4 Caliper and optical comparator warpage measurements	89
Table 4.5 Experimental and simulation model warpage with varying deposition speed..	90
Table 4.6 Experimental and simulation model warpage with varying layer height	92
Table 4.7 Material properties for parametric studies	93
Table 4.8 Simulation model warpage with varying coefficient of thermal expansion	94
Table 4.9 Simulation model warpage with varying thermal conductivity	95

Table 5.1 Process variable settings for mechanical property anisotropy..... 102

LIST OF FIGURES

	Page
Figure 1.1 Schematic of material extrusion additive manufacturing system.....	3
Figure 1.2 Schematic representation of molecules fabricated parts of (a) amorphous thermoplastics and (b) semi-crystalline thermoplastics	5
Figure 2.1 (a) HYREL System 30M machine with (b) close-up of extrusion head	11
Figure 2.2 Liquefier divided into three zones	24
Figure 2.3 Cross-section of several bonded roads showing key dimensions.....	26
Figure 2.4 Geometry of surface tension forces for a newly deposited filament.....	27
Figure 2.5 Specimens for mechanical property testing.....	31
Figure 2.6 Tensile test results	32
Figure 2.7 Failure surfaces of (a) V-0 specimen and (b) P-0 specimen	33
Figure 3.1 Filament extrusion process	37
Figure 3.2 Water bath and take-up system.....	37
Figure 3.3 Polypropylene filament	38
Figure 3.4 Test specimen	39
Figure 3.5 Viscosity surface plot of Polypropylene C.....	43
Figure 3.6 Viscosity surface plot of Polypropylene C1	43
Figure 3.7 Dilatometer test specimen	44
Figure 3.8 Coefficients of linear thermal expansion of Polypropylenes C and C1	46
Figure 3.9 Coefficients of linear thermal expansion of Polypropylenes D and D1-D3....	46
Figure 3.10 Hot Disk TPS 2500 S	48
Figure 3.11 Kapton-insulated Hot Disk sensor.....	48

Figure 3.12 Thermal conductivity experimental set-up.....	48
Figure 3.13 Thermal conductivities of Polypropylenes C and C1	49
Figure 3.14 Thermal conductivities of Polypropylenes D and D1-D3	50
Figure 4.1 Overview of material process simulation models	53
Figure 4.2 HYREL System 30M machine liquefier chamber and nozzle	54
Figure 4.3 Geometry, mesh and boundary conditions of liquefier chamber	56
Figure 4.4 Temperature contour plot of melt flow in the liquefier chamber	57
Figure 4.5 Geometry, mesh and boundary conditions of extrusion through the nozzle ...	58
Figure 4.6 Pressure contour plot of the nozzle from a simulation model.....	59
Figure 4.7 Pressure drop in the nozzle from an analytical model.....	60
Figure 4.8 Geometry, mesh and boundary conditions of die swell at the nozzle exit	62
Figure 4.9 Temperature contour plot of die swell at the nozzle exit	63
Figure 4.10 Die swell ratio calculation from a simulation model.....	64
Figure 4.11 Die swell ratio calculations from experiments	65
Figure 4.12 Geometry, mesh and boundary conditions before the first layer deposition.	68
Figure 4.13 Geometry, mesh and boundary conditions before the first layer cooling.....	69
Figure 4.14 Temperature distribution and deposited filament shape during the first layer deposition.....	70
Figure 4.15 Differences between the current and Bellini's simulation models.....	72
Figure 4.16 Temperature distribution during the first layer cooling	74
Figure 4.17 Temperature profiles of an ABS part measured using an infrared camera ...	75
Figure 4.18 Geometry, mesh and boundary conditions before the second layer deposition	76

Figure 4.19 Geometry, mesh and boundary conditions before the first and second layer cooling.....	77
Figure 4.20 Temperature distribution and deposited filament shape during the second layer deposition.....	79
Figure 4.21 Temperature distribution during the two-layer cooling.....	80
Figure 4.22 Geometry, mesh and boundary conditions before the residual stress/warpage simulation.....	82
Figure 4.23 Residual stress at steady-state	82
Figure 4.24 Warpage at steady-state from (a) a simulation model and (b) an experiment.....	82
Figure 4.25 Geometry differences in simulation models and experiments	84
Figure 4.26 Example plot of warpage vs. deposition length.....	85
Figure 4.27 Plot of warpage vs. number of layers from simulation models.....	86
Figure 4.28 Plot of experimental warpage with varying deposition temperature.....	87
Figure 4.29 Part warpage measurement using an optical comparator	89
Figure 4.30 Plot of experimental warpage with varying deposition speed.....	90
Figure 4.31 Plot of experimental warpage with varying layer height.....	91
Figure 5.1 SEM images of (a) Polypropylene D2 and (b) Polypropylene D1	98
Figure 5.2 Anisotropy test specimen with dimensions (Units in mm)	99
Figure 5.3 Anisotropy test specimens: (a) 0° fill angle and (b) 90° fill angle	100
Figure 5.4 Stress-strain curve of Polypropylene D2 with a 0° fill angle	101
Figure 5.5 Stress-strain curve of Polypropylene D2 with a 90° fill angle	101
Figure 5.6 Tensile stress at yield point with various deposition temperatures	103

Figure 5.7 Tensile stress at filament failure point with various deposition temperatures	104
Figure 5.8 Tensile nominal strain at filament failure point with various deposition temperatures	105
Figure 5.9 Modulus of elasticity with various deposition temperatures	106
Figure 5.10 Type V test specimen dimensions (Units in mm)	107
Figure 5.11 Temperature distributions from process simulation models with various fill angles and deposition temperatures	108
Figure 5.12 Tensile stress at yield point with various layer heights	109
Figure 5.13 Tensile stress at filament failure point with various layer heights	110
Figure 5.14 Tensile nominal strain at filament failure point with various layer heights	111
Figure 5.15 Modulus of elasticity with various layer heights	112
Figure 5.16 Temperature distributions from process simulation models with various fill angles and deposition temperatures	113

LIST OF ABBREVIATIONS

ABS	Acrylonitrile- <i>co</i> -Butadiene- <i>co</i> -Styrene
ANOVA	Analysis of Variance
ASA	Acrylonitrile Styrene Acrylate
CAD	Computer Aided Design
CTE	Coefficient of Thermal Expansion
FDA	Food and Drug Administration
FDM	Fused Deposition Modeling
FST	Flame, Smoke and Toxicity
PC	Polycarbonate
PET	Polyethylene Terephthalate
PETT	Polyethylene- <i>co</i> -Trimethylene Terephthalate
PLA	Polylactic Acid
PMMA	Polymethyl Methacrylate
POM	Polyoxymethylene
PPSF / PPSU	Polyphenylsulfone
SEM	Scanning Electron Microscope
TPC	Thermoplastic Copolyester
TPE	Thermoplastic Elastomer
TPU	Thermoplastic Polyurethane

SUMMARY

Among the most widely used additive manufacturing technologies is the material extrusion based process, in which a filament of thermoplastic material is liquefied and extruded through a nozzle to build a three-dimensional object in a layer-upon-layer fashion. One of the challenges of this technology is the limited availability of materials. In order to expand the portfolio of available materials, while reducing the cost of existing material productions, polypropylene-based polymers and composite materials for material extrusion additive manufacturing are investigated. However, since polypropylene is a semi-crystalline thermoplastic, a three-dimensional part fabricated with this material has a tendency to warp.

In this thesis, material extrusion process simulation models are developed that are capable of predicting the temperature distributions, deposited filament shapes, residual stresses and warpages/deformations of fabricated parts. An alternative to reduce warpage of polypropylene parts is to create composite materials by combining with additives. Therefore, these process simulation models support the development of new materials by predicting part warpages quickly and cost effectively without the need of iterative experiments.

These material extrusion process simulation models can be applied to both the quality and performance of fabricated parts, such as warpage and mechanical property anisotropy. The correlations between process variable settings on additive manufacturing machines and material properties of polypropylene-based composite materials on warpage characteristics are determined. In addition, the correlations between mechanical

property anisotropy and the bonding quality of extruded filaments are examined experimentally by producing tensile property data of fabricated parts with different fill angles. The efficacy of the process simulation models are then evaluated by comparing the experimental and simulation model results.

CHAPTER 1

INTRODUCTION AND MOTIVATION

1.1 Introduction

Additive manufacturing describes a technology that builds three-dimensional objects by adding materials in a layer-upon-layer fashion. This technology has been described as revolutionizing product development and manufacturing, since process steps and time are reduced using additive manufacturing [1]. Once a model is generated using a three-dimensional Computer Aided Design (CAD) system, an additive manufacturing machine reads the CAD data to fabricate a three-dimensional object using an additive approach, with each layer being a thin cross-section of the model. A direct part fabrication with additive manufacturing is a single-step process regardless of the complexity of the part, which eliminates the need for process planning. In addition, due to the fact that computers are used throughout, this technology accelerates the product development process.

Advancements in additive manufacturing have had a great impact in the design and manufacturing of products. Flexibility in design limitations is allowed in additive manufacturing, although they are often imposed by conventional manufacturing processes. Unique capabilities of additive manufacturing processes include the ability to create customized parts and adding improved functionalities such as complex geometries. With additive manufacturing technologies, products can be printed using multiple materials to achieve unique mechanical and/or electrical properties, which are not achievable using traditional processes. These additive manufacturing capabilities, along

with many others, allow and will continue to allow companies to drive significant changes within their supply chains.

Today, the role of additive manufacturing technologies in engineering product development processes seems to improve the current operations of the companies using unique capabilities of additive manufacturing processes. Examples include quicker turnaround time, reduction in number of parts and the ability to create customized parts. The design phase of the product development process is accelerated with the use of additive manufacturing. During the design stage, multiple iterations of design alternatives are necessary to finally select the final design of a product. Additive manufacturing technologies allow companies to reduce the time required during this stage because prototypes of products with potential designs can be created and tested rapidly and cost-effectively. Another capability of additive manufacturing processes is the ability to produce parts with complex geometries. Doing so leads to reduction in number of parts, then to decrease in assembly time and manufacturing cost. The productivity of the companies can also be enhanced using additive manufacturing technologies because it has the ability to create customized tools that are being used during testing and assembly on the shop floor. The ability to customize part geometry for customers has proven to be beneficial especially in the field of medical technology. Examples include fabrications of dental crowns, Align Technology's Invisalign aligners and Siemens' hearing aid shells [2, 3]. These devices are produced on a large scale, although they are customized to requirements of each customer. Currently, the engineering product development process is still an extremely long process, but this can be improved with the aid of additive manufacturing technologies.

Among the most widely used additive manufacturing technologies is the material extrusion based process, commonly referred to as Fused Deposition Modeling (FDM) [4]. This technology was developed by Stratasys, Ltd., and the initial patent was awarded to

its founder, Scott Crump, over two decades ago [5]. Material extrusion additive manufacturing technology can be described simply as a process where material contained in a liquefier chamber is forced out through a nozzle by applying pressure [1]. One type of feedstock of material extrusion additive manufacturing consists of a filament of thermoplastic material, which is heated and liquefied or melted in a liquefier chamber. The solid portion of the filament acts as a piston to push the liquefied material through a nozzle, and as the material is deposited onto a build platform, the nozzle traces the cross-section pattern of each layer in a horizontal x-y plane. In a solid part, each filament bonds to the adjacent, previously extruded filaments and solidifies to create a solid structure. Once a layer is completed, the build platform moves downwards in the vertical z direction so that the next layer can be deposited. This process is repeated until the build is completed. The schematic of an extrusion head of a material extrusion additive manufacturing system is shown in Figure 1.1.

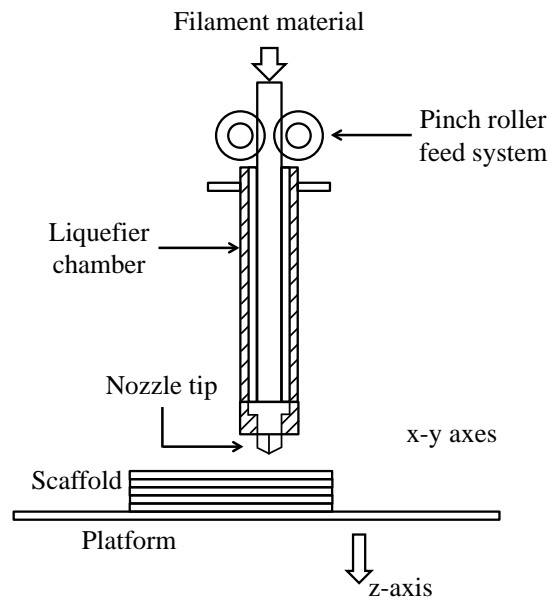


Figure 1.1 Schematic of material extrusion additive manufacturing system

1.2 Motivation

The role of additive manufacturing technologies in engineering product development processes can greatly change the future. A possible eventual outcome is more company contributions with smaller supply chains. Many companies today work with a large number of suppliers who supply parts of a final product. As more companies adopt additive manufacturing technologies, their supply chains can be simplified, which allows companies to reduce costs by removing redundancies between themselves and suppliers.

The advancements that will be made in the field of additive manufacturing will affect the future success of additive manufacturing technologies. However, various challenges arise that need to be overcome first, such as limited availability of materials. This has already been an important point of focus by many researchers, and growth in the current limitations will hopefully shape the future of additive manufacturing adoptions. As mentioned previously, many of the part geometries that are unachievable using conventional manufacturing processes can be realized. As different material compositions are investigated, additive manufacturing technology will be improved even further by expanding the portfolio of available materials, leading to improved part properties.

In this thesis, reinforced polymers for material extrusion additive manufacturing are investigated, in order to support the advancements in developing new materials, reducing the cost of existing material productions and expanding the applications of novel materials. Polypropylene, a widely used thermoplastic that is inexpensive and flexible compared to acrylonitrile-*co*-butadiene-*co*-styrene (ABS), is the material of interest of this research. Polypropylene also offers high flexibility and durability, and is suitable for a broad area of applications, such as containers, packaging and bottle caps [6]. However, polypropylene is a semi-crystalline thermoplastic unlike ABS, which is an

amorphous thermoplastic, and there are processing issues associated with material extrusion of polypropylene. As shown in Figure 1.2, the molecules in semi-crystalline thermoplastics are drawn together and ordered during the crystallization process, so they shrink more compared to amorphous thermoplastics. This causes parts that are fabricated with polypropylene to warp more and detach from the build platform, compared to those with ABS.

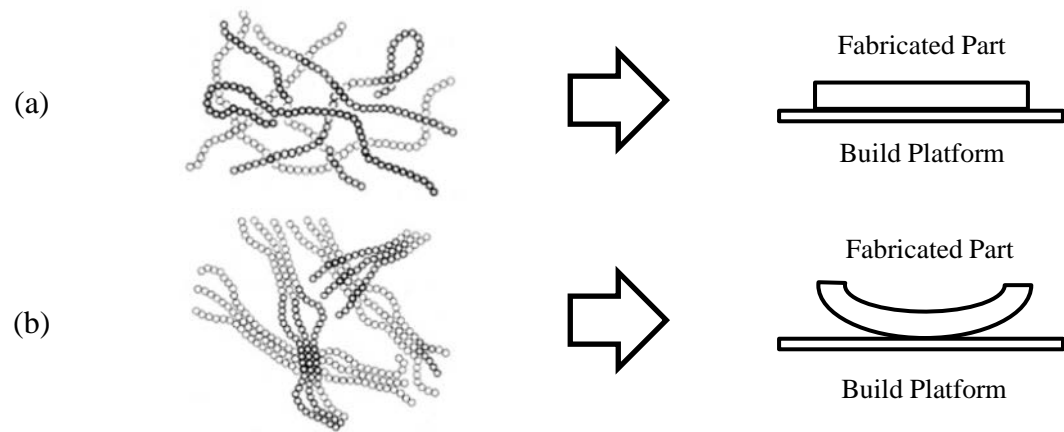


Figure 1.2 Schematic representation of molecules fabricated parts of (a) amorphous thermoplastics and (b) semi-crystalline thermoplastics

Alternatives to reduce warpage are to investigate polypropylenes with reduced crystallinity and/or create polypropylene-based composite materials by combining polypropylene with additives. Several types of additives exist, such as particles, fibers and agents that affect viscosity and thermal conductivity. Although this allows for a large variety of possible composite materials, trying to create new materials requires a vast amount of effort and time and can be expensive. In order to make this process quicker and more cost effective, computational methods are required instead of solely relying on iterative experiments. Therefore, the objective of this thesis is to develop material

extrusion process simulation models that are capable of predicting the temperature distributions, deposited filament shapes, residual stresses and warpages/deformations of fabricated parts, where the inputs are material properties, process variable settings and process conditions.

1.3 Research Question and Hypothesis

The goal of this research is to investigate the capability of polypropylene-based composite materials in material extrusion additive manufacturing computationally and experimentally. The quality and performance of fabricated parts, such as warpage and mechanical property anisotropy, are examined with material extrusion process simulation models. These predictions are compared with experimental results to evaluate the models' efficacy. In order to achieve this goal, this thesis seeks to answer the following research questions:

Research Question 1:

Which process variable settings on material extrusion additive manufacturing machines and material properties of polypropylene-based composite materials affect the warpage and deformation characteristics of the fabricated parts?

Hypothesis 1:

By developing material extrusion process simulation models, the correlations between process variable settings and material properties, and warpage and deformation characteristics can be determined.

Research Question 2:

Which process variable settings on material extrusion additive manufacturing machines affect the bonding quality of the extruded filaments?

Hypothesis 2:

Producing tensile property data of fabricated parts with different fill angles will allow mechanical property anisotropy and filament bonding performance to be correlated. The experimental results are compared to process simulation model results to determine the models' efficacy.

1.4 Organization of This Thesis

This thesis is organized in the following manner. In Chapter 1, the introduction and motivation for this work, as well as the research questions this thesis seeks to address were provided. In Chapter 2, background information discussing material extrusion additive manufacturing technology, as well as literature reviews on process modeling are presented. In Chapter 3, material processing, material compositions and material characterizations of polypropylene-based materials are described. In Chapter 4, the development and validation of material extrusion process simulation models are presented. The parametric studies of warpage/deformation simulation model are also detailed in this chapter. In Chapter 5, mechanical property anisotropy and its correlations to the bonding quality of extruded filaments are investigated. In Chapter 6, the research questions and hypotheses are reviewed and the contributions resulting from this thesis are discussed. The conclusions of this work and suggestions for future work are also outlined.

CHAPTER 2

MATERIAL EXTRUSION ADDITIVE MANUFACTURING TECHNOLOGY AND LITERATURE REVIEW

2.1 Introduction

Chapter 2 introduces background information and literature review of material extrusion additive manufacturing. Section 2.2 contains the basic principles, machines and materials that are available for material extrusion additive manufacturing technology. Section 2.3 is concerned with processing issues associated with material extrusion of polypropylene, which is the material of interest of this thesis. Section 2.4 surveys literature on the topic of process modeling of material extrusion additive manufacturing. Section 2.5 is concerned with mechanical properties of fabricated parts and some experimental results are presented to demonstrate their anisotropic properties.

2.2 Material Extrusion Additive Manufacturing Technology

2.2.1 Basic Principles

As stated in the previous chapter, material extrusion additive manufacturing describes a technology that uses extrusion to form three-dimensional parts. The basic principles of this technology that are common to any extrusion-based system are discussed in this section [1].

- 1) Material Loading – A thermoplastic filament is fed into the liquefier chamber as a continuous supply of material for the liquification process.

- 2) Liquification – Heat is applied to the chamber using heat coils in order to melt the filament to a semi-liquid state.
- 3) Extrusion – The shape and size of the extruded filament are determined by the extrusion nozzle. For example, with a nozzle with a large diameter, the three-dimensional part could be fabricated more quickly but high precision cannot be achieved. A fabrication of a large part with features and wall thicknesses with at least twice the nozzle diameter is more suitable with material extrusion additive manufacturing.
- 4) Solidification – The extruded filament ideally remains the same shape and size during solidification. However, it shrinks upon cooling, which may cause distortion of the part. One way to minimize this is to keep the temperature gradient between the chamber and the surrounding atmosphere to a minimum.
- 5) Bonding – During and after deposition, sufficient residual heat energy to activate the surfaces of the filament and adjacent regions is required to cause bonding. If sufficient energy is not supplied to the material by the extrusion head, a distinct boundary between new and previously deposited filament is created. In contrast, too much energy results in a poorly defined part as well.

2.2.2 Additive Manufacturing Machine

The material extrusion additive manufacturing machine that is used in this research is called HYREL System 30M from HYREL 3D [7]. This is a versatile material extrusion machine, which is capable of fabricating high quality parts and supporting research and development of extrusion materials and technologies. The hardware and

software are meant to be open, enabling users to have complete control over the extrusion process. The additive manufacturing machine and a close-up of the extrusion head are shown in Figures 2.1 a and b, respectively. Both the X and Y stages of this machine are cantilevered off of a beam that is driven by the Z stage. The platform moves side-to-side in the X direction, while the extrusion head translates front-to-back along the Y axis.

Some of the adjustability is illustrated in Figure 2.1 b. The force exerted by the filament drive system on the filament is adjustable using the set-screws labelled “Roller tension adjustments.” Additionally, one of the drive rollers is spring-mounted, which enables a constant normal force to be exerted on the filament even if the filament diameter varies. This facilitates material development research, since the requirements on making uniform filaments are not as stringent as for filament production. Another example is the nozzle cooling fan. This can be turned on or off, which is useful if deposited filaments can be cooled to solidify quickly, when that is important for quality part production. One setting that is not adjustable on this machine is the build chamber temperature. Although this capability is not available on this machine, the build chamber can often be heated on commercial machines, which is a good means for reducing thermal gradients of extruded filaments, allowing for more consistent dimensional accuracy of fabricated parts.

All told, the HYREL System 30M machine consists of over twenty adjustable settings, in both software and hardware, which can be fine-tuned to facilitate deposition of a wide range of materials. However, material extrusion machines vary in their achievable process variables, such as layer thickness and nozzle dimensions. The phenomena that are observed on the materials and parts printed on the HYREL machine

will apply to other material extrusion machines, but the phenomena will be scaled up and down depending upon the process variables.

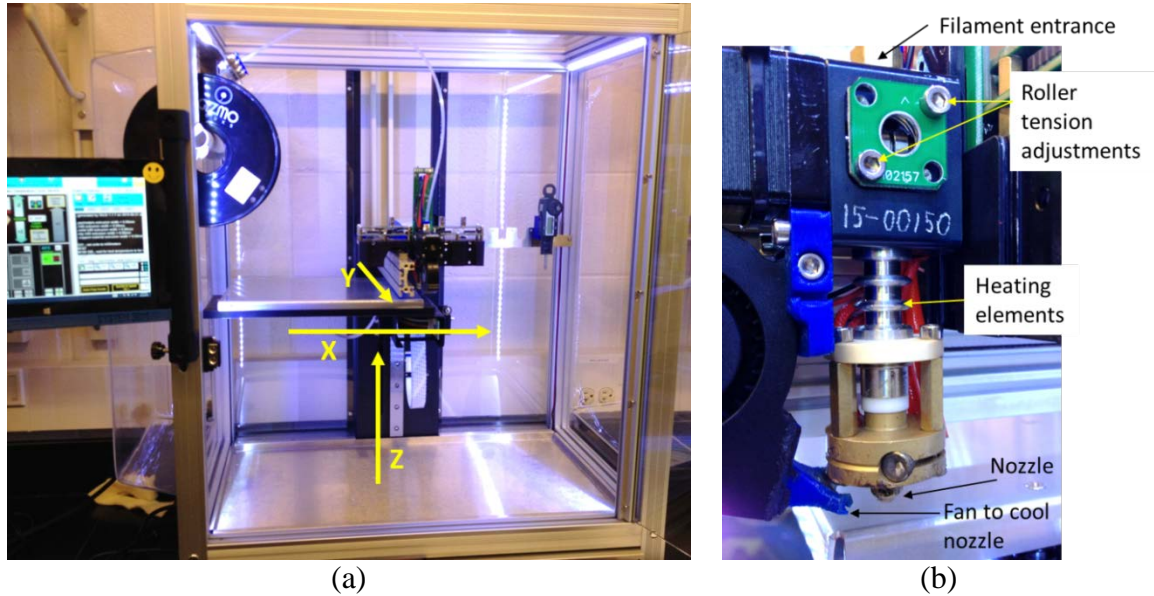


Figure 2.1 (a) HYREL System 30M machine with (b) close-up of extrusion head

2.2.3 Materials and Costs

2.2.3.1 *Materials*

There is a variety of material options for material extrusion additive manufacturing technology, each with unique characteristics designed to meet the application needs. Several types of thermoplastics are commercially available to be used on high-end Stratasys FDM machines and their key characteristics are summarized in Table 2.1.

Table 2.1 Key characteristics of Stratasys commercially available thermoplastics [8]

Material	Key Characteristics
ABS-M30™ / ABS <i>plus</i> ™	Versatile / Tough
ABSi™	Translucent
ABS-M30i™	Biocompatible
ABS-ESD7™	Electrostatic discharge resistant
ASA	UV stable
Nylon 12	Strong (high fatigue resistance)
PC	Strong (tension)
PC-ABS	Strong (impact)
PC-ISO™	Biocompatible
PPSF / PPSU	Resistant (thermal/chemical)
ULTEM™ 9085	Mechanically well-rounded / FST certification
ULTEM™ 1010	Food-safety / Biocompatible / Highest heat resistance

ABS is the most widely used material in material extrusion additive manufacturing, and it has been the basis for this technology for many years. Today, there are five versions of ABS, each mechanically superior to the original ABS formulation [1, 8-10]. ABS-M30™ is the most popular material in the material extrusion process due to good material properties as well as simple post-processing. This material formulation is for the Fortus™ additive manufacturing machines, and is also known as ABS*plus*™ for the Dimension® additive manufacturing machines. An advantage of ABSi™ is translucency, and this material formulation should be selected to fabricate see-through parts. ABS-M30i™ complies with stringent regulations and is classified as biocompatible, so it can be used for products that come in contact with skin, food and medications. A key characteristic of ABS-ESD7™ is that it is electrostatic discharge resistant. Since this material formulation prevents a buildup of static electricity, it is

suitable for applications where a static charge can damage products or impair performance.

The other commercially available materials in case the ABS material formulations do not fulfill the application requirements are: acrylonitrile styrene acrylate (ASA), Nylon 12, polycarbonate (PC), polyphenylsulfone (PPSF/PPSU), ULTEM™ 9085 and ULTEM™ 1010 [1, 8-10]. With ASA, a UV-stable thermoplastic, it is possible to build parts that will not degrade with prolonged exposure to sunlight. Nylon 12 is ideal for aerospace and automotive applications that demand high fatigue resistance. Parts fabricated with this material are the toughest in the material extrusion additive manufacturing industry, and exhibit 100 to 300 percent better elongation at break and superior fatigue resistance compared to other materials available in this technology. PC is the most widely used industrial thermoplastic, and PC-based materials provide higher tensile and flexural properties. Variations of this material are PC-ABS and PC-ISO™. PC-ABS gives the most desirable properties of both PC and ABS materials, such as the mechanical properties and heat resistance of PC and the flexural strength of ABS. PC-ISO™ is another biocompatible material and is certified for use in medical, pharmaceutical and food-packaging industries. If the parts need to withstand severe heat and exposure to chemicals, then an option would be to use PPSF/PPSU that has excellent heat and chemical resistance. ULTEM™ 9085 is suitable for use in aerospace, automotive and military applications due to its favorable flame, smoke and toxicity (FST) rating and high strength-to-weight ratio. This material also has well-rounded thermal, mechanical and chemical properties that make it superior in most categories compared to other commercially available materials. Lastly, ULTEM™ 1010 offers the highest heat

resistance, chemical resistance and tensile strength of any commercially available thermoplastics for material extrusion additive manufacturing technology. With the lowest coefficient of thermal expansion, this material also offers excellent thermal stability.

Aside from the materials available on high-end material extrusion additive manufacturing machines, there are more materials used among additive manufacturing enthusiasts. They are introduced below and their key characteristics are listed in Table 2.2.

Table 2.2 Key characteristics of other available thermoplastics [6, 11, 12]

Material	Key Characteristics
PLA	Environmentally friendly / Biodegradable / High strength / Impact resistance
PET	High strength / High stiffness / Lightweight / Recyclable / FDA approved
PETG	High strength / High flexibility / Durability / Lightweight
PETT	High strength / High stiffness / Lightweight / Transparency / Biocompatible
TPE / TPU	Extreme flexibility
TPC	Extreme flexibility / Heat resistance / Chemical resistance / UV resistance
POM / Acetal	High stiffness / Low friction / Wear resistance
PMMA / Acrylic	Transparency / High impact resistance / High stiffness

Polylactic acid (PLA) is one of the two most widely used materials among material extrusion additive manufacturing enthusiasts, with the other being ABS [6, 11, 12]. It is one of the most environmentally friendly thermoplastics available. Since it is a biodegradable thermoplastic that is made from renewable resources, such as corn starch

and sugar cane, less energy is required to process this material compared to traditional, petroleum-based thermoplastics.

Polyethylene terephthalate (PET) is considered as an alternative to ABS and PLA due to its high strength [6, 11, 12]. It is also recyclable and has been approved by the U.S. Food and Drug Administration (FDA) for use in food containers. A blend of PET and Glycerol, PETG, offers high strength, flexibility and durability, and has good inter-layer adhesion for improved surface finish. Polyethylene-*co*-trimethylene terephthalate (PETT) is a clear, high stiffness thermoplastic whose main characteristics are high strength, transparency and biocompatibility.

Thermoplastic elastomer (TPE), especially thermoplastic polyurethane (TPU), is a flexible material that feels like rubber with its high elastic characteristics [6, 11, 12]. This material can fabricate parts that must bend in order to fulfill its functionality, such as springs and stoppers. Other advantages include good adhesion to the build platform and inter-layer bonding. Thermoplastic copolyester (TPC) is another flexible, rubber-like material, and it offers excellent heat, chemical and UV resistances.

Polyoxymethylene (POM), also known as acetal, is ideal for applications that require precision parts [6]. Due to its high stiffness, low friction and wear resistant characteristics, this material is suitable for parts with mechanical functions, such as gearwheels and ball bearings. Polymethyl methacrylate (PMMA), widely known as acrylic, is another material used by additive manufacturing enthusiasts due to its transparency, high impact resistance and high stiffness.

2.2.3.2 Material Costs

One of the reasons for polypropylene being the material of interest of this thesis is its reduced cost. Therefore, the costs of the materials discussed in Section 2.2.3.1 and that of polypropylene need to be compared. They are listed in descending order by pellet cost in Table 2.3, although those of PETT and TPC were not found.

Table 2.3 Costs of thermoplastics in pellets and filaments [6, 13-20]

Material	Pellet Cost [dollars/kg]	Filament Cost [dollars/kg]
PPSF / PPSU	30.00	355
ULTEM™ 1010	20.00	190
ULTEM™ 9085	20.00	300
Nylon 12	7.00 - 7.50	40
TPE / TPU	4.75 - 5.24	26 - 56
ASA	3.52	52
PC	3.43 - 3.63	28 - 50
PMMA / Acrylic	2.75 - 2.86	34
PET	2.60 - 2.71	62 - 81
POM / Acetal	2.53 - 2.75	30 - 50
PETG	2.51 - 2.73	22 - 50
ABS	2.40 - 2.46	22 - 27
PLA	1.98 - 2.20	23 - 43
PP	1.41 - 1.80	33 - 63
PETT	-	59 - 66
TPC	-	39

Table 2.3 shows that the pellet cost of polypropylene is indeed the lowest among the available materials in material extrusion technology. The most commonly used material, ABS, is also on the lower end of this list but polypropylene costs even less. One reason for this is due to the difference in the types of thermoplastics for ABS and polypropylene. ABS is an engineering thermoplastic, which means that it holds excellent

mechanical and thermal properties but they tend to be more expensive over commodity thermoplastics, such as polypropylene [21].

The pellet costs do not directly correlate to filament costs, but a huge markup is observed from Table 2.3. The commonly used materials range in price from \$22 to \$50 for a kilogram of filaments, depending on the quality and manufacturer. This is approximately ten times the cost of the thermoplastic pellets used to make the filaments. Of course, there are added costs over the original materials that need to be accounted for, such as equipment costs. In addition, the diameter tolerances on good quality filaments are tight, and producing filaments that meet the quality standards consistently requires good process control and good equipment. However, according to engineers at 3D printing companies, the filament costs are still artificially inflated even after taking these added costs into account [22].

2.3 Material Extrusion Additive Manufacturing with Polypropylene

Polypropylene can be categorized into three types: homopolymer, random copolymer and impact copolymer [23]. Homopolymer polypropylenes are the most commonly used polypropylene material in these three categories, and they only contain propylene monomers in the semi-crystalline solid form. Random copolymers refer to ethylene/propylene copolymers that are made by copolymerizing propylene with small amounts of ethylene. The ethylene content significantly affects the properties of the polymer chains, and thermoplastics with better impact properties, decreased melting temperature and enhanced flexibility are achieved. Impact copolymers are mixtures of

homopolymer polypropylenes and random copolymers that have the overall ethylene contents of approximately 6-15%.

Although there are advantages to using polypropylene in additive manufacturing, including cost reduction, there are processing issues associated with material extrusion of this material. Amorphous thermoplastics, like ABS, are more suitable for material extrusion additive manufacturing process than semi-crystalline thermoplastics, like polypropylene, since amorphous thermoplastics have no distinct melting temperatures [1]. Although they soften and viscosity decreases as temperature is increased, the viscosity of amorphous thermoplastics is sufficiently high that their shape is mostly maintained after extrusion.

Following deposition, the material begins to cool and shrink. Data for mold shrinkage values for several thermoplastics are presented in Table 2.4. Although these data are normally used for sizing molds for injection molding, these values provide a relative understanding of shrinkage for these materials. The data presented in Table 2.4 indicate that polypropylene has a higher shrinkage value than ABS. This result is expected because ABS is an amorphous thermoplastic and polypropylene is a semi-crystalline thermoplastic. The molecules in semi-crystalline thermoplastics are drawn together and ordered during the crystallization process. Therefore, semi-crystalline thermoplastics have higher characteristic shrinkage values compared to amorphous thermoplastics. This property correlates to the warpage of fabricated parts. Since polypropylene shrinks more compared to ABS, it causes parts fabricated with polypropylene to warp more and detach from the build platform, compared to those with ABS.

Table 2.4 Characteristic shrinkages of thermoplastics [24, 25]

Material	Shrinkage [mm/mm]
PMMA / Acrylic	0.002 - 0.008
ABS	0.004 - 0.007
PC	0.005 - 0.007
Nylon 12	0.008 - 0.020
PP	0.010 - 0.030
POM / Acetal	0.018 - 0.023

Love et al. at Oak Ridge National Laboratory demonstrated that the warping and distortion of the part during deposition decreased drastically by introducing carbon fiber into the polymer feedstock, which in this case was ABS [26]. The carbon fiber additions decreased the coefficient of thermal expansion (CTE) and increased thermal conductivity of the material, which resulted in a profound impact on the geometric accuracy of fabricated parts. A decrease in CTE led to a decrease in the strain the part experienced as it cooled from the deposition temperature to ambient temperature. In addition, an increase in the thermal conductivity led to a decrease in thermal gradients throughout the part. The CTE and thermal conductivity values for ABS with and without the reinforcement are summarized in Table 2.5. This shows that the CTE of the reinforced material parallel to the deposition direction was reduced and its thermal conductivity was increased, but the values did not change significantly for the reinforced material perpendicular to the deposition direction compared to the neat ABS.

Table 2.5 CTE and thermal conductivity for ABS with and without carbon fiber reinforcement [26]

Material	CTE [$\mu\text{m}/\text{m}\cdot^\circ\text{C}$]	Thermal Conductivity [$\text{W}/\text{m}\cdot^\circ\text{C}$]
ABS	87.32 ± 6.17	0.177
ABS/CF 13% parallel to deposition	9.85 ± 0.84	0.397
ABS/CF 13% perpendicular to deposition	106.30	0.156

Three sets of bar specimens were fabricated to demonstrate the effects of CTE and thermal conductivity on the geometric distortion [26]. The specimen dimensions were: length = 102.0 mm, width = 5.0 mm and thickness of 7.6 mm. The first bar specimen was fabricated with ABS on a Stratasys uPrint, which had a temperature-controlled build chamber. The second specimen was fabricated with ABS on a Solidoodle, which had a heated build platform but not a build chamber. The third specimen was fabricated with ABS with carbon fiber reinforcement on a Solidoodle. The end deflections were measured for each specimen and the results are summarized in Table 2.6. The carbon fiber reinforced material demonstrated less warpage compared to either of the neat ABS specimens.

Table 2.6 Part distortions of bar specimens printed with ABS with and without carbon fiber reinforcement [26]

Materials	Additive Manufacturing Machine	End Deflection	
		End 1 [mm]	End 2 [mm]
ABS	uPrint	5.18	2.09
ABS	Solidoodle	18.2	5.86
ABS/CF	Solidoodle	1.92	0.79

The researchers at Oak Ridge National Laboratory used ABS as the base material of the reinforced material. However, it was shown in Table 2.4 that the shrinkage value of polypropylene is higher than that of ABS, which means that polypropylene parts warp even more than ABS parts. Therefore, creating polypropylene-based composite materials by combining polypropylene with additives in order to reduce warpage is a critical aspect of supporting the advancements in developing new materials.

2.4 Process Modeling of Material Extrusion Additive Manufacturing

In this section, analytical models of the material extrusion process are investigated in order to better understand the relationships among the physical quantities that control the flow of material during this process.

2.4.1 Material Flow

Material flow through the nozzle is similar to capillary flow and is controlled by the pressure drop between the chamber and the surrounding atmosphere. However, the extrusion process used for additive manufacturing differs from most conventional extrusion processes. A simple model can be developed of material flow through the liquefier. Mass flow through a nozzle is related to pressure drop, nozzle geometry and material viscosity. A simple volumetric flow rate model provides a good starting point. The subscript f will be used to denote variables related to the filament fed into the extruder and r will denote variables associated with roads being deposited. The volumetric flow rate into the liquefier is [27, 28]:

$$Q = v_f \pi r_f^2 \quad (2.1)$$

where v_f is the filament feed velocity and r_f is the radius of the filament. At the nozzle, the volumetric flow rate, Q , is:

$$Q = v_r WH \quad (2.2)$$

where v_r is the deposition velocity, W is the width of the deposited road and H is its height, assuming that the deposited filament has more of a rectangular shape than circular [27]. By equating the flow rates, the feed velocity can be determined by assuming that the deposition velocity is given:

$$v_f = \frac{v_r WH}{\pi r_f^2} \quad (2.3)$$

Feed rate can be related to motor drive speed through [27, 28]:

$$v_f = \omega_p R_p \quad (2.4)$$

where ω_p is the angular velocity of the pinch rollers and R_p is the pinch roller radius.

The force required to push the filament through the extrusion head can be determined if the pressure drop, ΔP , through the liquefier can be estimated [28]:

$$F = \Delta P A \quad (2.5)$$

where A is the cross sectional area of the filament. Pressure drop will be discussed in a later section. With the force determined, the torque and power required to drive the filament can be computed [28]:

$$\Gamma = FR_p \quad (2.6)$$

$$P_{mot} = \omega_p \Gamma \quad (2.7)$$

This model assumes that one motor drives the pinch rollers through a gear train.

When driving the filament through the extruder, it is important to avoid buckling of the filament. This occurs if the driving force exceeds the liquefier's ability to melt the material and extrude it through the nozzle. For neat thermoplastic filaments, buckling is typically not an issue, but this becomes important as the material becomes more brittle by, for example, the addition of filler materials.

2.4.2 Melt Properties

Although it is convenient to consider the liquification and extrusion process to be isothermal, temperature variations occur throughout the process. Therefore, material properties need to be considered as a function of temperature in this case [4].

Viscosity controls much of the material's behavior through the liquefier. The approach used here begins with the assumption that material extrusion materials are shear-thinning and follow a power-law viscosity model as shown in Equation (2.8):

$$\eta = K(\dot{\gamma})^{n-1} \quad (2.8)$$

where η is viscosity, $\dot{\gamma}$ is shear rate and K and n are power-law fit parameters [28, 29]. In order to account for the temperature dependence of viscosity, Bellini et al. [28] suggested separating the viscosity expression into temperature and shear-rate dependent terms as follows in Equation (2.9):

$$\eta = H(T)\eta_{T_o}(\dot{\gamma}) \quad (2.9)$$

The latter shear-rate dependent term is typically taken as the power-law expression evaluated at a reference temperature, T_α . The temperature dependent term is typically assumed to be described by an Arrhenius model as shown in Equation (2.10):

$$H(T) = e^{\left[\alpha\left(\frac{1}{T} - \frac{1}{T_\alpha}\right)\right]} \quad (2.10)$$

where α is the activation energy [28].

2.4.3 Pressure Drop

The pressure drop through the liquefier can be determined through a momentum flux balance approach [28, 29]. To aid model development, it is important to divide the liquefier into three regions and determine quantities in each region. Figure 2.2 shows the liquefier divided into the cylindrical barrel, the conical nozzle and exit region.

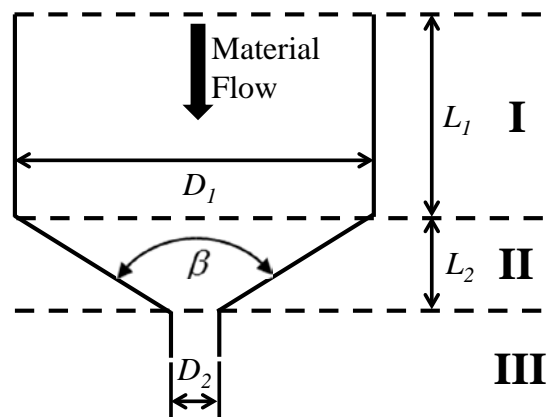


Figure 2.2 Liquefier divided into three zones

Considering a fluid element in each region, the pressure drop in each region can be determined through application of the power law. Non-isothermal conditions are assumed; temperature difference effects on viscosity are captured in the terms that are based on Equation (2.10). Note that the overall pressure drop is the sum of the pressure drops in each region:

$$\Delta P = \Delta P_1 + \Delta P_2 + \Delta P_3 \quad (2.11)$$

Each pressure drop term is given as [4, 28]:

$$\Delta P_1 = 2L_1 \left(\frac{v}{\phi}\right)^{\frac{1}{m}} \left(\frac{m+3}{\left(\frac{D_1}{2}\right)^{m+1}}\right)^{\frac{1}{m}} e^{\left[\alpha\left(\frac{1}{T}-\frac{1}{T_\alpha}\right)\right]} \quad (2.12)$$

$$\Delta P_2 = \frac{2m}{3 \tan\left(\frac{\beta}{2}\right)} \left(\frac{1}{D_2^{\frac{3}{m}}} - \frac{1}{D_1^{\frac{3}{m}}}\right) \left(\left(\frac{D_1}{2}\right)^2 (m+3) 2^{m+3}\right)^{\frac{1}{m}} e^{\left[\alpha\left(\frac{1}{T}-\frac{1}{T_\alpha}\right)\right]} \quad (2.13)$$

$$\Delta P_3 = 2L_2 \left(\frac{v}{\phi}\right)^{\frac{1}{m}} \left(\frac{(m+3)\left(\frac{D_1}{2}\right)^2}{\left(\frac{D_2}{2}\right)^{m+3}}\right)^{\frac{1}{m}} e^{\left[\alpha\left(\frac{1}{T}-\frac{1}{T_\alpha}\right)\right]} \quad (2.14)$$

which are complicated functions of liquefier dimensions, temperatures and power law fitting terms.

2.4.4 Road Deposition and Spreading

The behavior of a filament deposited on top of another filament is the result of complex interactions among many physical phenomena. Although related to road cooling

and bonding, it is informative to consider the filament spreading behavior and observe the shape of solidified roads before delving into the complications of cooling and bonding.

The final shape of a solidified road is influenced by several phenomena and actions: the initial extruded shape as related to the stand-off distance between the nozzle and previous layer, the deposition temperature, the build chamber temperature, the local temperature distribution, thermal properties of the filament material and local cooling characteristics (convection rates, influence of radiation, etc.). Several research groups have characterized and modeled road shape, pore size and bonding [30-32]. A micrograph of the cross-section of several roads is shown in Figure 2.3 [30], where W is the filament width, H is the layer thickness and $2y$ indicates the neck length between adjacent filaments. This group demonstrated that neck radius varied with height in a fabricated part, ranging from $y = 75.4 \mu\text{m}$ at the bottom layers to $y = 50.9 \mu\text{m}$ at top layers of a 30-layer part with $0.25 \mu\text{m}$ layer thickness. These differences were attributed to mainly the repeated application of thermal energy when subsequent layers were deposited on existing layers, causing bottom layers to be at higher temperatures for longer periods of time.

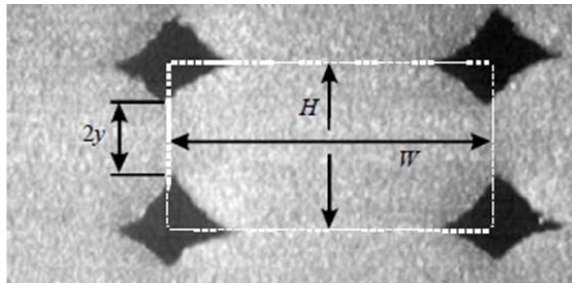


Figure 2.3 Cross-section of several bonded roads showing key dimensions [30]

Locally, road spreading represents a competition between surface tension (resists spreading), wetting, sintering to neighboring roads and gravity-driven creep. Furthermore, the filament is cooling rapidly and solidifying while spreading occurs. Understanding these phenomena and their interactions is critically important in understanding final road and part shapes and providing insight into how the process may be controlled.

To date due to many complications, no one has developed an engineering model that adequately predicts road shape and neck size. The basis for model development is illustrated in Figure 2.4 [4], which shows the geometry of the surface tension forces caused by the various interfaces (LV: liquid-vapor, SL: solid-liquid, SV: solid-vapor). It is assumed that a road is deposited onto a previous road that has a radius of curvature, R . The solid-liquid contact angle is denoted as θ .

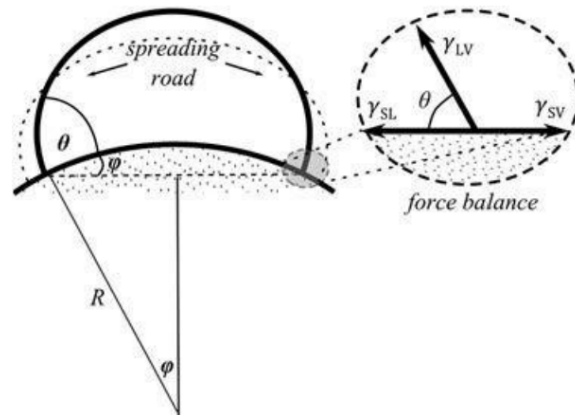


Figure 2.4 Geometry of surface tension forces for a newly deposited filament [4]

2.4.5 Road Cooling and Bonding

Bonding quality among filaments is critical for a part's mechanical properties. Despite twenty years of research, no good predictive models of filament bonding have been developed and experimentally validated. However, an understanding of many of the important phenomena and relationships can be gained in a qualitative sense.

Bonding is thought to occur among roads due to the viscous sintering (also known as viscous flow sintering) mechanism. Solid state sintering may also play a role when the local temperature is above the material's glass transition temperature. Some researchers have applied Frenkel and Newtonian sintering models to predict neck growth through molecular diffusion and viscous flow. Typical approaches to model building involve fitting to experimental data or to surface tension. As a result, it is difficult to objectively validate models of sintering for this process.

A number of researchers have developed models of heat transfer to predict temperature distributions in roads, layers and/or parts. Some have developed limited models to quantify the "bonding potential" of roads by tracking the total amount of time that a point on a road is high enough for sintering. However, since the bonding potential is not a physical quantity, the value of these investigations is limited to mostly qualitative understanding of the influence of different phenomena. Most two-dimensional models demonstrate that the temperature differences across the cross-section of a road are negligible, so others have adopted a lumped capacity model that yields a one-dimensional transient heat transfer model (along the filament) that admits an analytical solution [4]. Although this is convenient, it is insufficient to deal with more complex process simulations.

Two research groups have attempted some experimental validation of heat transfer models. This is accomplished by embedding thermocouples in the build platform and monitoring temperatures as filaments are deposited on the platform and on subsequent layers. Results from Bellini et al. [28] showed that the lumped capacity model agreed with experiments better for short times and higher temperatures, while two-dimensional numerical models were better for lower temperatures and longer investigation times. The other research group [30] built 15 and 30-layer small parts. As stated in [4], “experiments showed that the temperature of a road increases almost instantaneously when a melt layer is deposited on top of it followed by a rapid decay, on a time scale of ~2 seconds, back below the glass transition temperature to a few degrees above the build environment temperature.” Notably, even after 30 layers were deposited, the thermocouple indicated that it was above the build environment temperature.

In summary, given the complexity of the extrusion and part-building processes, it is not clear what the ideal process variable settings for quality part building are. One approach is to explore the construction of high fidelity process models that can simulate the fabrication of reasonably sized parts and predict filament bonding.

2.5 Mechanical Properties

Mechanical properties of parts fabricated using material extrusion are of great interest. Also of interest is to reduce the anisotropy inherent in these parts. As is well recognized, properties are much higher for parts built in the XY plane, compared to properties in the Z direction, since Z direction properties depend entirely on filament bond strength. In this process, bonds are weaker than filaments. In this section, the

relationships between process variable settings and mechanical properties will be discussed.

Experimental verification of some of the modeling and simulation methods has been performed, to some extent, by several research groups. Sun et al. [30] showed that a correlation exists among road-to-road neck radius and flexural strength of test specimens. Rodriguez et al. [33] quantified the effects of mesostructure (road deposition pattern and pore size) on tensile strength and compared with monofilament strength. They also related process variables to pore size and mesostructure in order to identify process settings that maximize part strength through an understanding of bonding potential [34]. However, none of these researchers succeeded in modeling the material extrusion process well enough to predict mesostructures or mechanical properties.

Some example results will be presented that illustrate the orientation dependence of mechanical properties. Researchers built three sets of parts in a Dimension system from Stratasys with the ABS-M30 material, as shown in Figure 2.5 [35]. Specimen dimensions were: length = 150 mm, height = 20 mm and thickness = 4 mm. The first set, denoted, H-XX, were tensile test specimens built horizontally, where H-0 indicates that the specimen was oriented along the X axis, its height along Y and its thickness in the Z direction. Specimens labelled V-XX were called “vertical,” meaning that the height dimension (20 mm dimension) was oriented along the Z axis. Finally, the specimens labelled P-XX (for “perpendicular”) had their length dimension oriented along the Z axis.

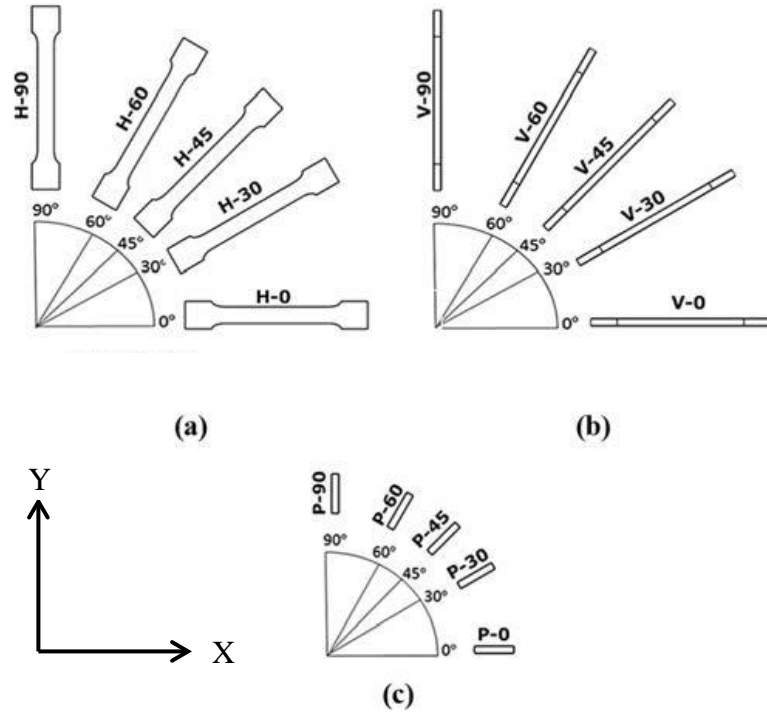


Figure 2.5 Specimens for mechanical property testing [35]

Tensile tests indicated anisotropic properties as seen in Figure 2.6, particularly for tensile strength. The perpendicular parts were the weakest, as expected, since their strength was primarily dependent on bond strength between layers. Additionally, for the perpendicular specimens, the high surface roughness caused by layer boundaries and internal pores may have acted as stress concentrations and fracture initiation sites, which caused lower strength. The modulus of elasticity was fairly uniform across all sets of specimens and all orientations. It is important to note that elongation at break is highly dependent on orientation, as reported by Stratasys on their ABS-M30 specification sheet [36]. They reported elongation results of 7% for XZ orientation (corresponds to V in the paper), while ZX orientations (P in the paper) exhibited elongation of only 2%. This

indicated that while P specimens may be stiff, they failed much earlier (lower load, less strain) than parts in other orientations.

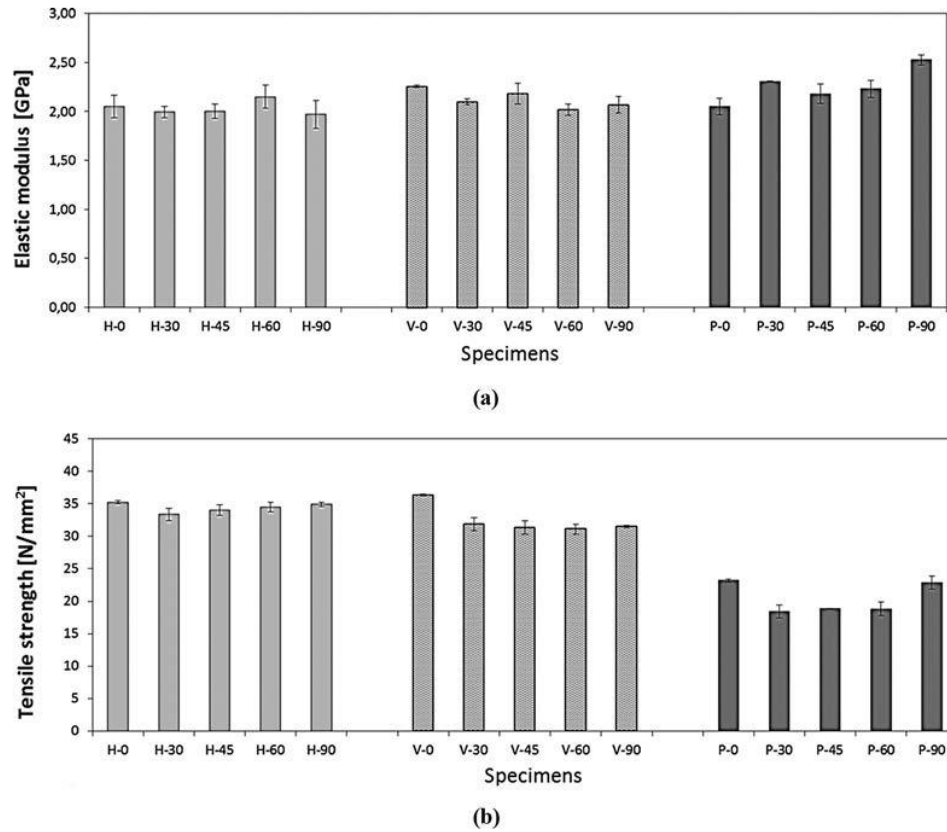


Figure 2.6 Tensile test results [35]

It is instructive to examine micrographs of failure surfaces of these specimens since the road deposition pattern becomes evident. Figure 2.7 shows failure surfaces for the V-0 and P-0 specimens. What is particularly evident is that failure for P-0 occurred between layers, since the deposition pattern of internal roads is apparent, with pores between the roads and the failure surface flat. The road deposition pattern is also evident in the V-0 specimen. The contours that define part surfaces and the oriented roads that fill the interior (which are oriented at 45 degree angles) are clearly seen. Also, the deposition

pattern for interior roads alternated between 45 degrees and 135 degrees on subsequent layers. What is not observed in the tensile results in Figure 2.6 is a strengthening or stiffening for the H-45 or V-45 specimens, which would indicate a contribution to mechanical properties from these internal roads.

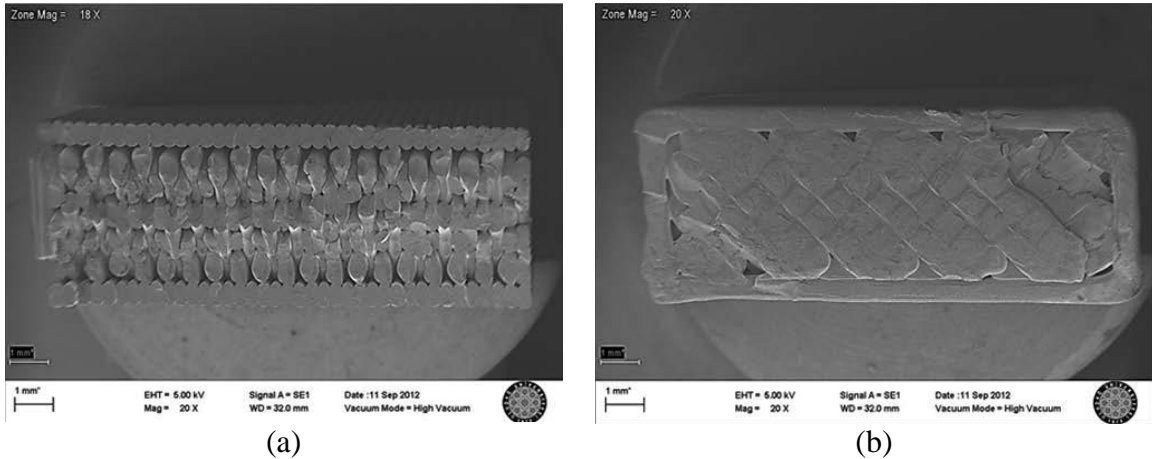


Figure 2.7 Failure surfaces of (a) V-0 specimen and (b) P-0 specimen [35]

An interesting comparison can be made between tensile specimens from today's prototyping material extrusion additive manufacturing machine [35] and material extrusion technology from ~2000 [33]. Yield strength and modulus of elasticity for specimens fabricated on an FDM-2000 machine in the standard Stratasys ABS material were 24.4 MPa and 1,986 MPa, respectively. These compare with the H-0 results from [35] of 35.0 MPa and 2,000 MPa, respectively. As can be seen, tensile strength has improved considerably. The improvement in tensile strength can be attributed to improvements in build parameters that reduce defects, and possibly better thermal management in build chambers and improvements in materials.

2.6 Summary

This chapter presented the background knowledge relevant to studying the material extrusion additive manufacturing process. There are several materials that are available for this technology, but polypropylene is the cheapest among all of them in terms of the cost of pellet. This supports the motivation of this thesis, which is to reduce the cost of existing material productions while supporting the advancements in developing new materials. However, there are processing issues associated with material extrusion of polypropylene due to its high shrinkage value that causes final parts to warp and detach from the build platform. The literature review on processing modeling of the material extrusion process revealed that analytical models were investigated by researchers, but there has been limited success on development of process models that can predict road shapes and filament bonding. In addition, the mechanical properties of final parts are of great interest, and the relationships between process variable settings and mechanical properties were discussed. The investigations on the correlations between mechanical property anisotropy and filament bond quality of polypropylene parts are detailed in Chapter 5 of this thesis.

CHAPTER 3

MATERIAL PROCESSING, MATERIAL COMPOSITIONS AND MATERIAL CHARACTERIZATIONS

3.1 Introduction

Chapter 3 focuses on material processing, material compositions and material characterizations of polypropylene-based materials, including neat polymers and their composite materials. Section 3.2 details the material processing methods in material extrusion, which are filament extrusion and test specimen fabrication. Section 3.3 introduces the candidate materials that were investigated in this research. Section 3.4 contains material characterization procedures and experimental data discussions. The three topics covered in this section are: viscosity, coefficient of thermal expansion and thermal conductivity.

3.2 Material Processing

Feedstock for material extrusion additive manufacturing consists of an extruded filament of thermoplastic material with a diameter of approximately 1.75 mm. The materials that were investigated in this research were supplied in pellets. Therefore, the productions of filaments on an extruder were required prior to being used as feedstocks on additive manufacturing machines to fabricate parts.

The equipment used during filament extrusion process is presented in Figure 3.1. The pellets are first fed in the hopper, they are melted and as the screw rotates the melted

polypropylene gets pushed along the extruder, then the filament finally comes out of the die. In this research, filaments were extruded using a 3/4" single screw extruder with an L/D ratio of 25:1 attached to a Brabender Intelli-Torque system. A general purpose screw with a compression ratio of 3:1 was used. There were three heating zones along the barrel of the extruder, and the die was a vertical rod die with interchangeable nozzles. A rod die nozzle with an L/D ratio of 3:1 and an orifice size of 3/16" (4.76 mm) was used to produce filaments of approximately 1.75 mm diameter. A water bath was built and positioned in between the extruder and take-up system in order to cool down the filament and minimize the filament diameter variations. This is critical because without it, controlling the dimensional accuracy of the filament was challenging. For this water bath, two acrylic rods were fixed onto a plastic container, and the rods were enclosed by two PVC tubes so that the tubes rotated as the filament was pulled by the take-up system. The rotations of the PVC tubes were critical aspects of producing filaments with a fairly consistent diameter. The close-up image of water bath and take-up system is illustrated in Figure 3.2.

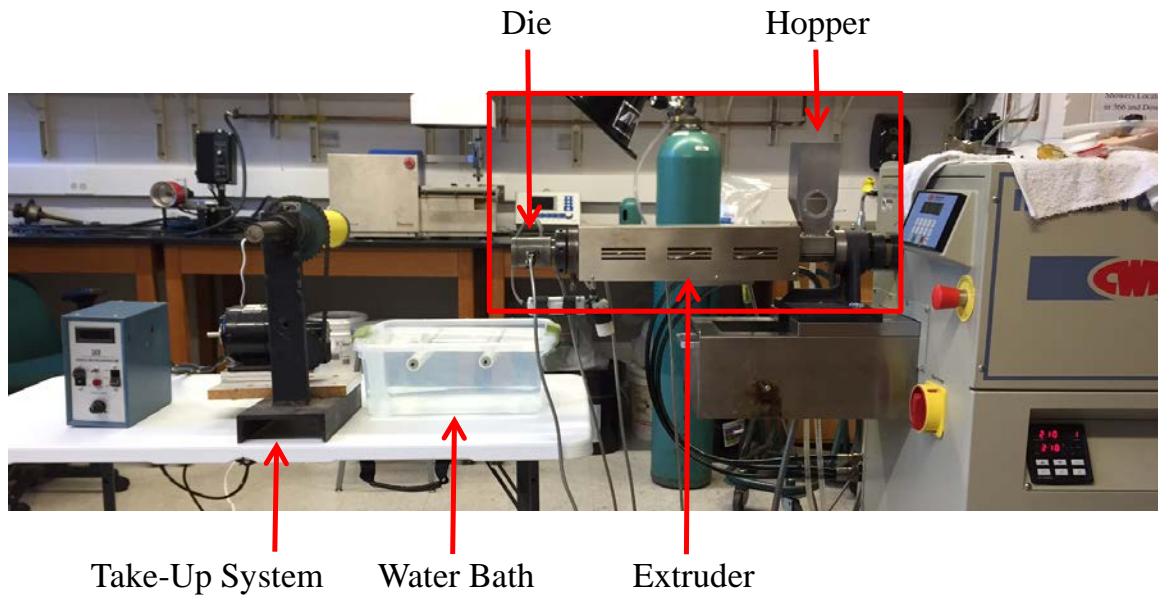


Figure 3.1 Filament extrusion process

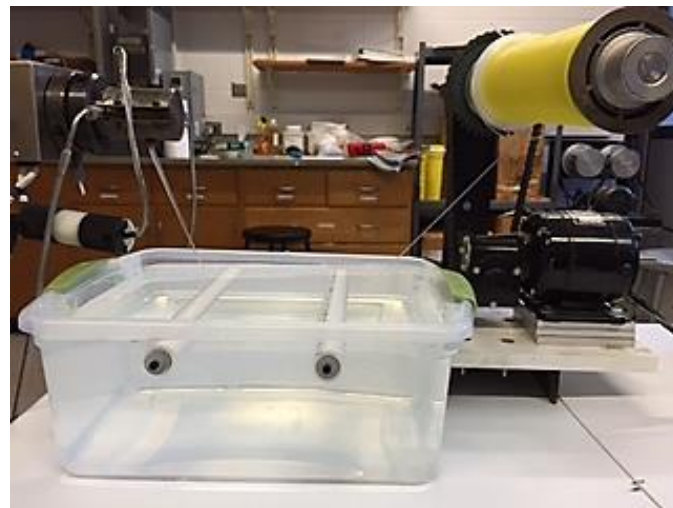


Figure 3.2 Water bath and take-up system

Several filament extrusion trials, with various process variable settings, were required to attain the desired filaments with 1.75 mm diameter. There were three adjustable parameters, which were extruder and die temperatures, extruder screw speed

and take-up speed. It was determined that the temperatures and extruder screw speed were directly correlated to filament diameter, whereas take-up speed was indirectly correlated to filament diameter. The process variable settings differed between each material that was investigated in this study, but the ranges of those settings adopted for the extrusion of polypropylene filaments are depicted in Table 3.1.

Table 3.1 Process variable settings for polypropylene filament extrusion

Parameter	Filament Extrusion
Extruder and die temperatures	140 - 180 °C
Extruder screw speed	35 - 45 rpm
Take-up speed	50 rpm

The output of this process is a filament of polypropylene with a diameter of approximately 1.75 mm, as shown in Figure 3.3. This extruded filament was then used as feedstock in the material extrusion additive manufacturing machine to fabricate a test specimen with a rectangular base measuring 30 mm x 20 mm and a height of 2.5 mm as shown in Figure 3.4.

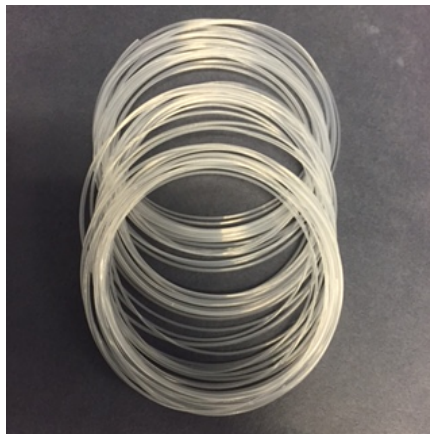


Figure 3.3 Polypropylene filament

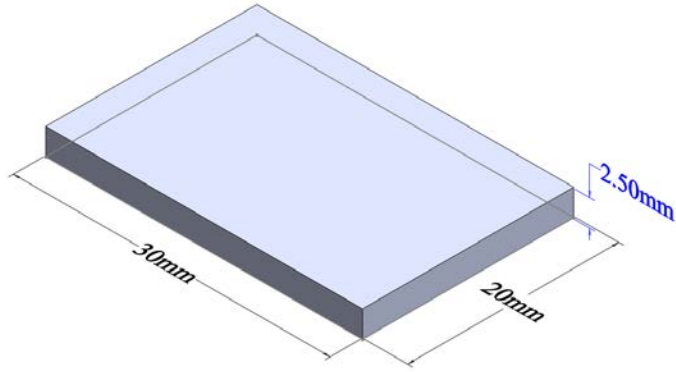












Figure 3.4 Test specimen

3.3 Material Compositions

During this research, ten different neat polypropylene-based polymers were investigated. Out of those, test specimens shown in Figure 3.4 were successfully fabricated on a material extrusion additive manufacturing machine (HYREL System 30M from HYREL 3D) with five of the polypropylenes (Polypropylenes A through E). The top and side views of the test specimen as well as percent crystallinity of Polypropylenes A through E are presented in Table 3.2.

Table 3.2 Test specimens and percent crystallinities of candidate neat polypropylenes

Polypropylene	Test Specimen		% Crystallinity
Polypropylene A			52
Polypropylene B			39
Polypropylene C			34
Polypropylene D			13
Polypropylene E			10

Since polypropylene is a semi-crystalline thermoplastic polymer, it experiences a higher degree of shrinkage upon cooling than ABS, which is an amorphous thermoplastic polymer. This increased shrinkage led to increased part warpage, so polypropylene polymers with varying levels of crystallinity were explored. Table 3.2 shows that warpage was indeed related to the percent crystallinity of the material. Polypropylene A had the highest percent crystallinity and its test specimen showed the most warpage. In fact, the part fabrication with Polypropylene A could not be completed since it detached from the build platform completely during the fabrication process. In contrast, Polypropylene D and E had the lowest percent crystallinity and their test specimens showed the least warpage.

Another alternative to reduce warpage was to create polypropylene-based composite materials by combining polypropylene with additives. Several types of

additives exist, such as particles, fibers and agents that affect viscosity and thermal conductivity. One composite material (Polypropylene C1) was created with Polypropylene C as the base material, and three composite materials (Polypropylenes D1 through D3) were created with Polypropylene D as the base material. Test specimens were fabricated with these composite materials as well, but no significant differences in warpage were observed with respect to each other.

3.4 Material Characterizations

3.4.1 Viscosity

A combined theoretical and experimental approach was taken to characterize the flow characteristics of the materials, where a known model for the viscosity was compared to experimental viscosity data obtained from a capillary rheometer. Rheology is the study of deformation of the material under the influence of stresses, and a capillary rheometer is an apparatus designed to determine the rheological properties of polymer melts [37].

Experiments were conducted on a capillary rheometer (Dynisco LCR7001 [38]), which extruded a polymer through a capillary die with a circular orifice using a plunger, to obtain viscosity data at various temperatures (210, 220, 230 and 240 °C) and shear rates (5 - 10,000 s⁻¹). The L/D ratio of the capillary die was 40 with a length of 20 mm and a diameter of 0.5 mm. Two experimental runs were conducted at each temperature, with a total of eight experimental runs for each material. Using the power-law viscosity model and Arrhenius model discussed in Section 2.4.2, a viscosity expression as a function of temperature and shear rate was determined for each material. The calculated

constants as well as the viscosity expression of Polypropylenes C and C1 are listed in Table 3.3.

Table 3.3 Viscosity expressions of Polypropylenes C and C1

	Polypropylene C	Polypropylene C1
Reference temperature (T_α)	230 °C (503.15 K)	230 °C (503.15 K)
Activation energy (α)	1318.9	2299.5
K	3346.4	4280.3
$n - 1$	-0.54	-0.56
Viscosity expression	$\eta = e^{[1318.9(\frac{1}{T} - \frac{1}{503.15})]} 3346.4(\dot{\gamma})^{-0.54}$	$\eta = e^{[2299.5(\frac{1}{T} - \frac{1}{503.15})]} 4280.3(\dot{\gamma})^{-0.56}$

The resultant viscosity surface plots were created at shear rates representative of the material extrusion process (100 to 10,000 s⁻¹) and temperatures from 200 °C to 260 °C. The viscosity surface plots as well as the capillary rheometer experimental data of Polypropylenes C and C1 are presented in Figure 3.5 and Figure 3.6, respectively. Both of these surface plots show that viscosity decreases as temperature and shear rate increase. The viscosity range of Polypropylene C1 was also larger compared to that of Polypropylene C, but the two polymers demonstrated similar shear-thinning characteristics.

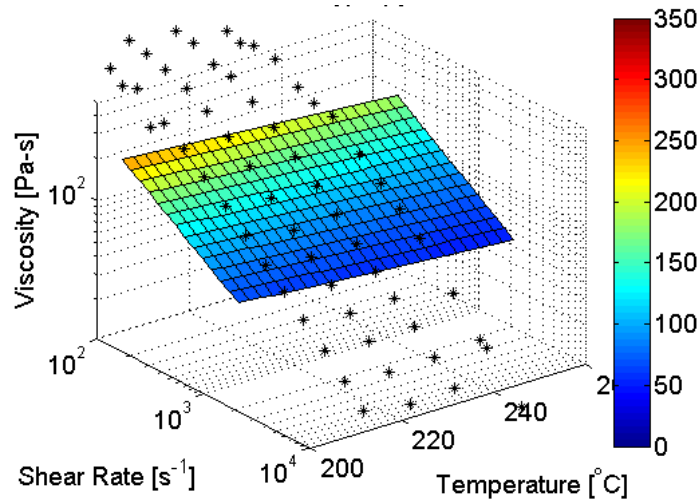


Figure 3.5 Viscosity surface plot of Polypropylene C

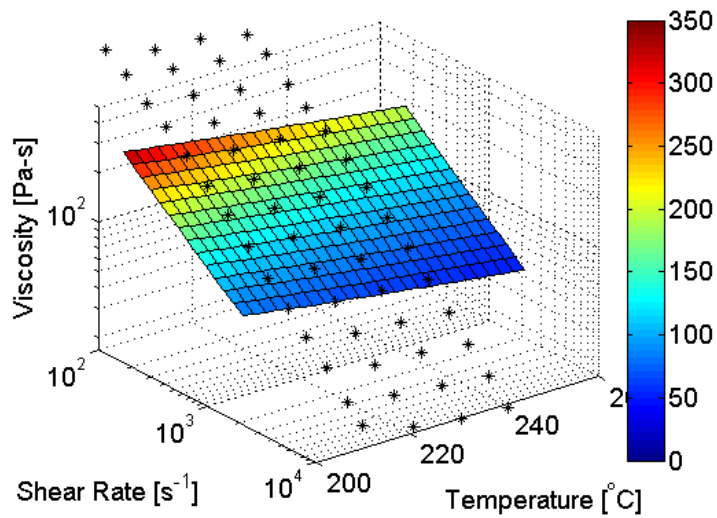


Figure 3.6 Viscosity surface plot of Polypropylene C1

3.4.2 Coefficient of Thermal Expansion

Another material property that was examined in this research was the coefficient of linear thermal expansion, since it was demonstrated to affect the geometric accuracy of

fabricated parts as they were subjected to temperature changes as discussed in Section 2.3.

A vertical push-rod dilatometer (Linseis L75 Platinum Series [39]) was used to measure the change in length of a specimen relative to that of the holder as a function of temperature, following procedures described in ASTM E228-11 [40]. The dilatometer test specimen is shown in Figure 3.7. During the test specimen fabrication, the filament was deposited along the length (20 mm dimension) for every layer to accurately measure the linear thermal expansion that the material experiences during material extrusion process. Three specimens were tested to measure the change in length for the temperature range of 20 °C to 90 °C for each material, and a constant heating rate of 5 °C/min was used. The maximum temperature used in the dilatometer experiment was much lower than a typical deposition temperature in material extrusion process, because the dilatometer test specimen deformed significantly at a higher temperature and the experiments could not be performed.

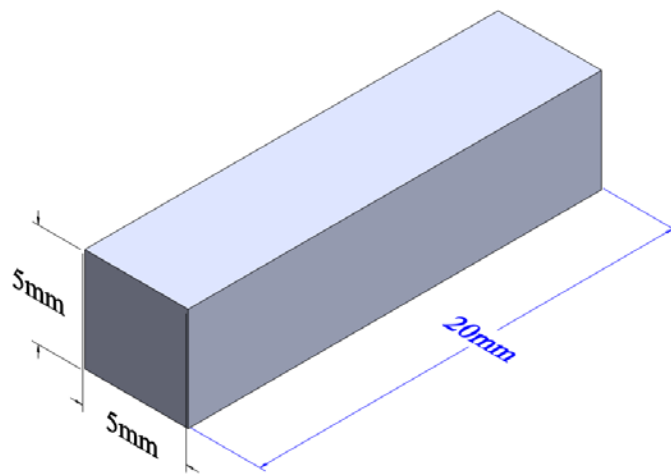


Figure 3.7 Dilatometer test specimen

The linear thermal expansion behavior and the coefficients of linear thermal expansion of neat polypropylenes and their composite materials were calculated from the measured data. Linear thermal expansion, $\frac{\Delta L}{L_0}$, refers to the change in length relative to the original length of the specimen accompanying a change in temperature as shown in Equation (3.1):

$$\frac{\Delta L}{L_0} = \frac{L_1 - L_0}{L_0} \quad (3.1)$$

where L_0 is the original length of specimen at temperature T_0 , L_1 is the length of specimen at temperature T_1 , and ΔL is the change in length of specimen between two temperatures.

The ratio between the expansion and the temperature difference that is causing it is referred to as the mean coefficient of thermal expansion, α_m , for the temperature range between T_0 and T_1 as shown in Equation (3.2). It is determined for a sequence of temperature ranges and is presented as a function of temperature.

$$\alpha_m = \frac{1}{L_0} \frac{\Delta L}{\Delta T} \quad (3.2)$$

The experimental results of coefficient of linear thermal expansion as a function of temperature for Polypropylenes C and C1 are presented in Figure 3.8 and those for Polypropylenes D and D1 through D3 are presented in Figure 3.9. The plots show that the neat polypropylenes have higher CTE values than polypropylene-based composite materials. As discussed in Section 2.3, researchers at Oak Ridge National Laboratory observed that one of the reasons the carbon fiber-reinforced ABS parts did not warp as

much as non-reinforced ABS parts was because the carbon fiber additions decreased the CTE [26]. The experimental results shown below agree with this phenomenon because part warpage was observed in the test specimens fabricated with neat polypropylenes as shown in Table 3.2. However, when the same test specimens were fabricated with polypropylene-based composite materials, warpage was not observed, presumably due to decreased shrinkage.

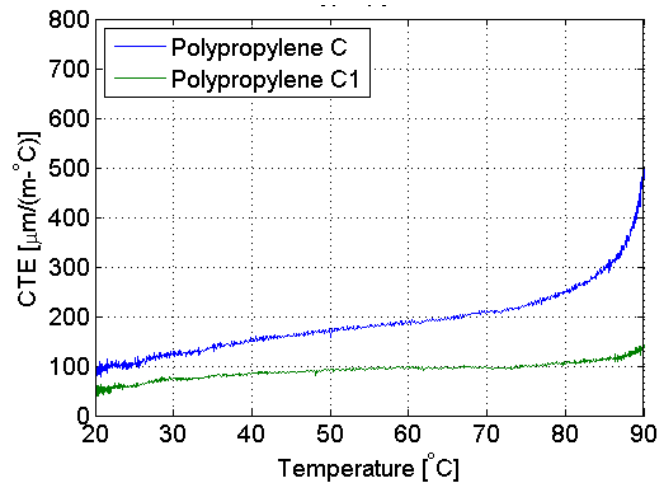


Figure 3.8 Coefficients of linear thermal expansion of Polypropylenes C and C1

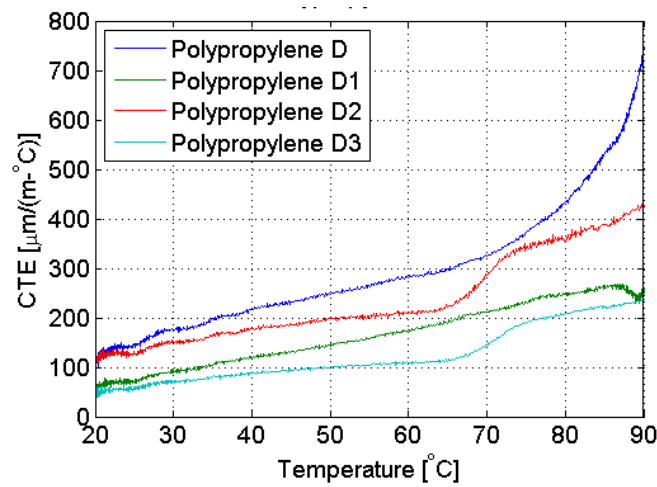


Figure 3.9 Coefficients of linear thermal expansion of Polypropylenes D and D1-D3

3.4.3 Thermal Conductivity

Differences in bonding quality between the extruded filaments were also observed with various materials. In order to examine the cause of these differences, thermal conductivity was considered. Since thermal conductivity is the property of a material to conduct heat, heat transfer occurs at a slower rate across materials with lower thermal conductivity than those with higher thermal conductivity. Therefore, it was hypothesized that the bonding quality will improve as thermal conductivity was increased. The thermal conductivities of neat polypropylenes and their composite materials were measured according to the transient plane heat source method using an instrument called Hot Disk TPS 2500S and a Kapton-insulated sensor as shown in Figure 3.10 and Figure 3.11, respectively. The Hot Disk sensor consisted of a nickel foil in the shape of a double spiral, which was sandwiched between two thin layers of Kapton [41]. Since the sample needed to be larger than the diameter of the Hot Disk sensor in each direction in order to get accurate measurements, the sensor was immersed in a beaker filled with a thermoplastic in this case as shown in Figure 3.12. The experiment was conducted inside of an environmental chamber, which allowed measurement over a temperature range of -50 °C to 200 °C.

During the measurement, an electrical current was passed through the sensor, and the resulting heat was dissipated through the sample. The temperature increase of the sensor as a function of time was recorded simultaneously. Three measurements were taken at each temperature, and the transient temperature profile was analyzed using the Hot Disk software to determine the thermal conductivity of the sample.



Figure 3.10 Hot Disk TPS 2500 S



Figure 3.11 Kapton-insulated Hot Disk sensor [41]



Figure 3.12 Thermal conductivity experimental set-up

The thermal conductivities as a function of temperature for Polypropylenes C and C1 are presented in Figure 3.13 and those for Polypropylenes D and D1 through D3 are presented in Figure 3.14. These plots showed that the thermal conductivities of these materials did not vary drastically with temperature over the temperature range used in the

experiment. In addition, a typical range of thermal conductivity of polypropylene is 0.12 to 0.22 W/(m·°C) [42]. The experimental data of the neat polypropylenes (Polypropylenes C and D) agreed with these values. Polypropylenes C1, D1 and D2 were also similar in values and they were between 0.1 and 0.3 W/(m·°C), which suggested that the additives in these polypropylene-based composite materials did not affect thermal conductivity. However, Polypropylene D3 had a higher thermal conductivity of approximately 0.6 W/(m·°C). These experiments were conducted in order to gain insights on the correlations between thermal conductivity and bonding. This investigation will be discussed in Chapter 5.

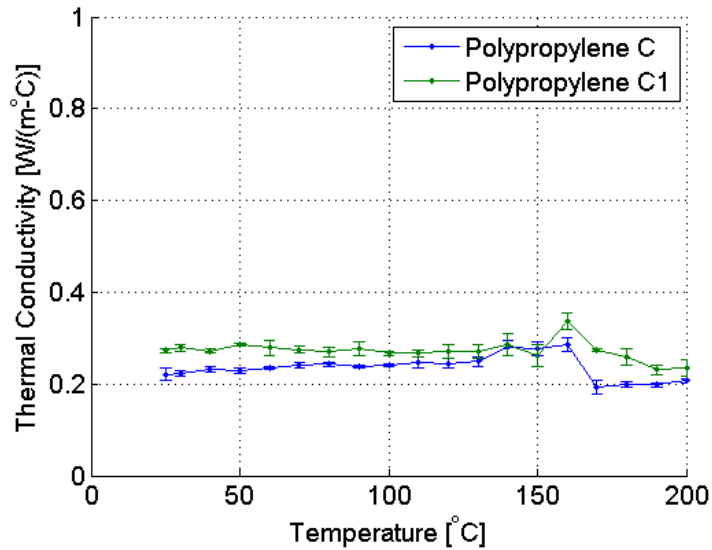


Figure 3.13 Thermal conductivities of Polypropylenes C and C1

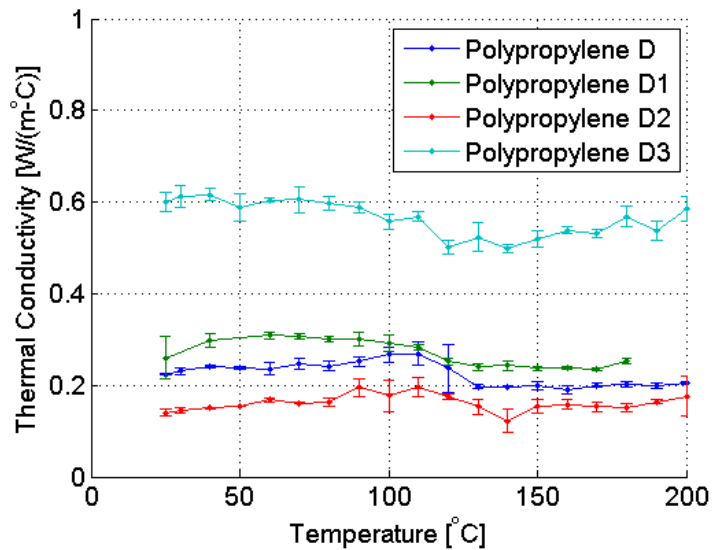


Figure 3.14 Thermal conductivities of Polypropylenes D and D1-D3

3.5 Summary

This chapter presented the material processing required in material extrusion technology to produce filaments from pellets so that they can be fed into additive manufacturing machines to fabricate parts. The equipment used during filament production process and the significance of the water bath in order to control the dimensional accuracy of the filaments were discussed. There were originally ten types of neat polypropylene-based polymers in this study. From these materials, two neat polymers were selected and their composite materials were also produced. Experiments were performed to characterize these materials, in particular viscosity, coefficient of thermal expansion and thermal conductivity. The power-law and Arrhenius viscosity models were compared to experimental viscosity data obtained from a capillary rheometer to create a viscosity expression as a function of temperature and shear rate for each material. The coefficient of thermal expansion data were obtained experimentally,

and it was shown that those of the neat polypropylene-based polymers were higher than those of their composite materials. This agreed with the discoveries by researchers at Oak Ridge National Laboratory that a decrease in CTE resulted in less part warpage. The thermal conductivities of polypropylenes were also measured. The additives in Polypropylenes C1, D1 and D2 had almost no effects on thermal conductivity compared to neat polypropylene-based polymers, but the additive in Polypropylene D3 increased its value significantly. These material characterizations are critical steps in understanding the effects of material properties on the quality and performance of the final parts in additive manufacturing. The data discussed in this chapter are applied and investigated further in subsequent chapters of this thesis.

CHAPTER 4

MATERIAL EXTRUSION PROCESS SIMULATION MODELS

4.1 Introduction

Chapter 4 details the development of two-dimensional material extrusion process simulation models using ANSYS® Polyflow and Mechanical. Section 4.2 presents simulation models for the six stages of material extrusion process: melt flow in the liquefier chamber, extrusion through the nozzle, die swell at the nozzle exit, first layer deposition and cooling, second layer deposition and two-layer cooling and warpage. The validation methods of these models are also discussed in this section. Section 4.3 contains the parametric studies of the warpage simulation model. The effects of varying process variable settings on material extrusion additive manufacturing machines and material properties of polypropylene-based composite materials on part warpage are investigated.

4.2 Process Simulation Model Development

Two-dimensional material extrusion process simulation models that can be exercised on new material formulations and process variable settings were developed using ANSYS® Polyflow and Mechanical. These process simulation models have the capability of predicting temperature distributions, deposited filament shapes, residual stresses and warpages/deformations of fabricated parts, where the inputs are material properties, process variable settings and process conditions. The overview of these process simulation models is presented in Figure 4.1.

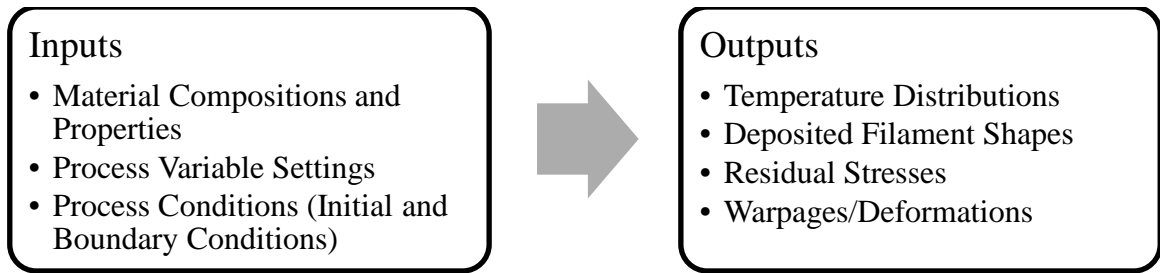
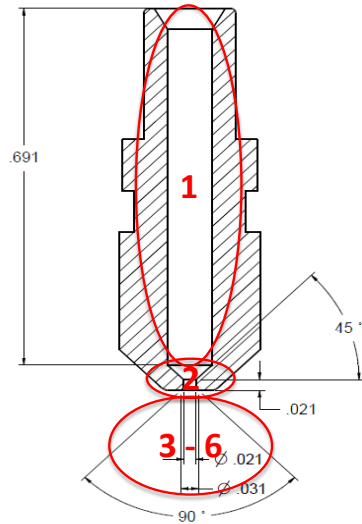


Figure 4.1 Overview of material process simulation models

The entire material extrusion additive manufacturing process was divided up into six stages in order to capture the thermal processes experienced at each stage. These regions are labeled on the drawing of liquefier chamber and nozzle of the HYREL System 30M machine in Figure 4.2 [7]. Due to limited capability of ANSYS® Polyflow and Mechanical, it was challenging to combine six process simulation models into one continuous model. Therefore, several simulations were developed, and these sequential simulations were linked to one another through the temperature profiles developed in previous steps. Polypropylene C was selected as a model system for study in this section. The process variable settings that are representative of the material extrusion process were selected as well and used as inputs to the simulation models. These values are presented in Table 4.1.



1. Melt Flow in the Liquefier Chamber
2. Extrusion through the Nozzle
3. Die Swell at the Nozzle Exit
4. Layer 1 Deposition / Cooling
5. Layer 2 Deposition / Layers 1 & 2 Cooling
6. Residual Stress / Warpage

Figure 4.2 HYREL System 30M machine liquefier chamber and nozzle

Table 4.1 Process variable settings

Process Variable Settings	Simulation Model Input Values
Deposition Temperature	220 °C
Deposition Speed	20 mm/s
Layer Height	0.2 mm

4.2.1 Melt Flow in the Liquefier Chamber

The first stage of the material extrusion process was the melt flow in the liquefier chamber. The purpose of this simulation was to determine the temperature contour plot of the thermoplastic filament in the liquefier chamber to verify that it reached a desired temperature at the liquefier exit. The geometry and mesh were created in ANSYS® Polyflow and those along with boundary conditions are shown in Figure 4.3. The coarse mesh was selected since this simulation model was only to verify that the thermoplastic filament reached the desired temperature, which was 220 °C in this case. This resulted in 42 nodes and 20 elements. This was a two-dimensional axisymmetric, steady-state, non-

isothermal problem, so the flow and thermal boundary conditions were labeled at every boundary. The top and bottom boundaries represented the entrance and exit of the liquefier chamber, respectively. The left boundary was the axis of symmetry, and the right boundary represented the liquefier chamber wall.

At the entrance, a volumetric flow rate of $2 \times 10^{-9} \text{ m}^3/\text{s}$ was applied as the flow boundary condition. This value was obtained from Equation (2.2), assuming a deposition speed of 20 mm/s and a layer height of 0.2 mm. Since the enclosure of HYREL System 30M machine was not temperature-controlled, a room temperature of 20 °C was used as the thermal boundary condition. At the liquefier chamber wall, zero wall velocity, also known as no-slip condition, was selected as the flow boundary condition. There were no normal and tangential velocities due to the adherence of melt to the liquefier chamber wall. A constant heat flux density, q_c , as the thermal boundary condition was a result of the heating element and it was calculated using Equation (4.1):

$$q_c = \frac{\dot{m}c_p\Delta T}{A} \quad (4.1)$$

where \dot{m} is the mass flow rate, c_p is the specific heat, ΔT is the temperature difference between the entrance and exit of the liquefier chamber and A is the surface area of the liquefier chamber [43]. At the exit, the outflow conditions were selected because there were no normal forces acting perpendicular to the surface and the direction of the flow must be perpendicular to the same surface.

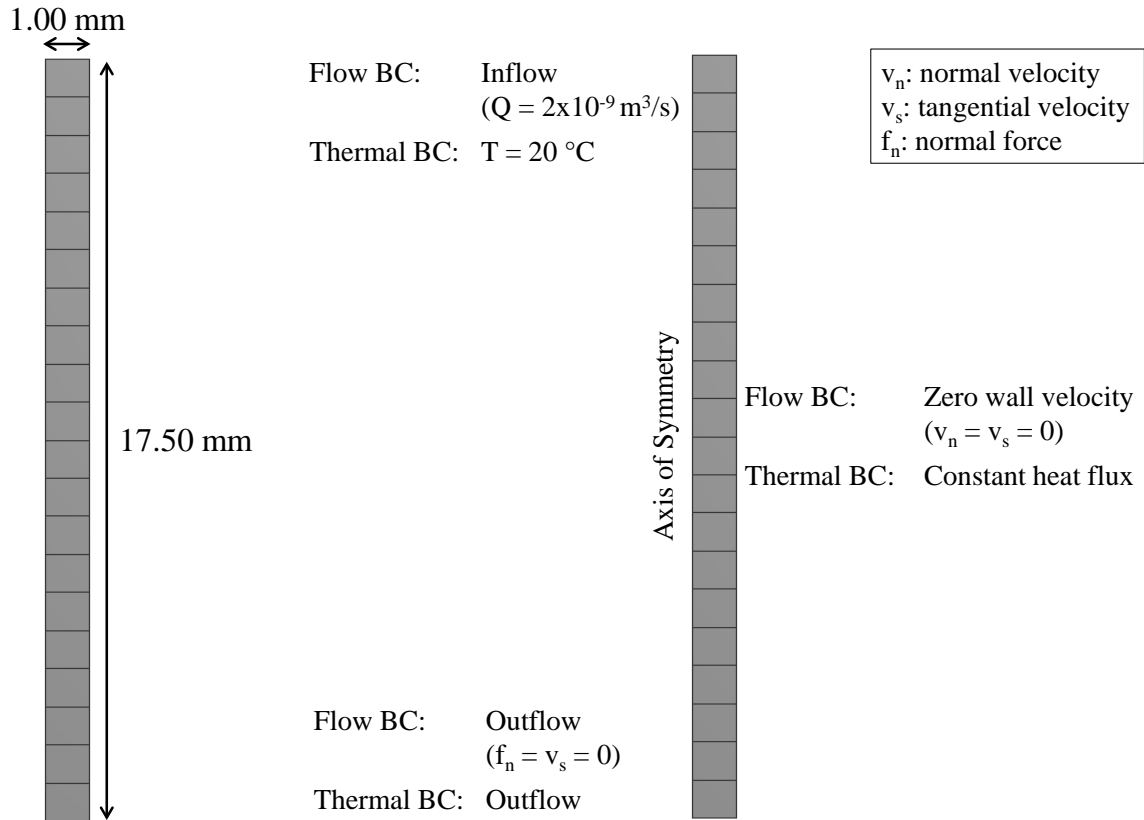


Figure 4.3 Geometry, mesh and boundary conditions of liquefier chamber

The temperature contour plot of melt flow in the liquefier chamber is shown in Figure 4.4. This represented the cross section of the whole liquefier with axis of symmetry in the center. The temperature at the liquefier entrance was $20 \text{ }^\circ\text{C}$, which was equal to the thermal boundary condition. The desired temperature of $220 \text{ }^\circ\text{C}$ was indeed achieved before the melt flow reached the exit. In addition, the melting temperature of this material was $151 \text{ }^\circ\text{C}$, and this temperature contour plot showed that almost a half of the material in the liquefier chamber was above this temperature.

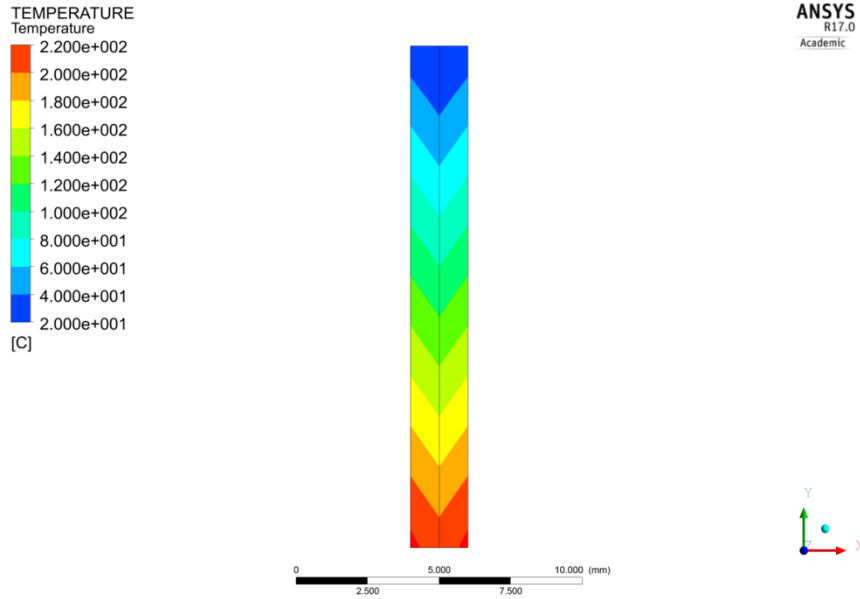


Figure 4.4 Temperature contour plot of melt flow in the liquefier chamber

4.2.2 Extrusion through the Nozzle

The second stage of the material extrusion process was extrusion through the nozzle. The geometry, mesh and boundary conditions are shown in Figure 4.5. The mesh was refined in the conical section of the nozzle in order to capture the changes in the flow in that region. This resulted in 644 nodes and 582 elements. This was a two-dimensional axisymmetric, steady-state, isothermal problem, so only a flow boundary condition was labeled at every boundary. The top and bottom boundaries represented the entrance and exit of the nozzle, respectively, and the nozzle entrance was equivalent to the liquefier exit in Figure 4.3 and Figure 4.4. The left boundary was the axis of symmetry and the right boundary represented the nozzle wall. The flow boundary conditions were the same as those for melt flow in the liquefier chamber in Section 4.2.1.

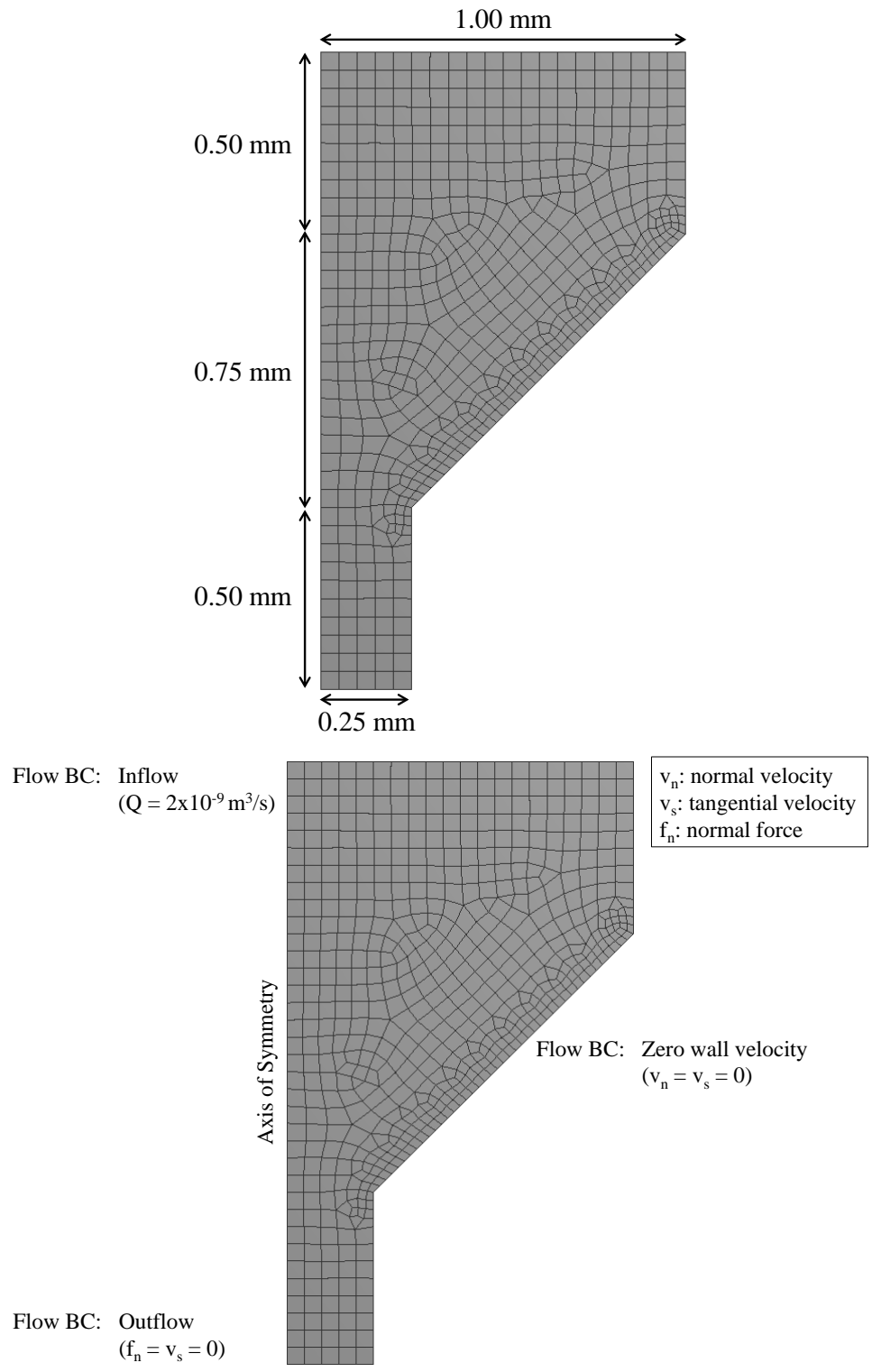


Figure 4.5 Geometry, mesh and boundary conditions of extrusion through the nozzle

The pressure contour plot of the entire nozzle with axis of symmetry in the center is shown in Figure 4.6. This depicted that the pressure drop between the entrance and exit of the nozzle was 2.61×10^5 Pa. The pressure drop was also calculated using an analytical model presented in Section 2.4.3. The surface plot of pressure drop as a function of deposition speed and layer height is shown in Figure 4.7. The pressure drop at a deposition speed of 20 mm/s and a layer height of 0.2 mm, which were the process variable settings used in this simulation model, was calculated to be 2.44×10^5 Pa. This resulted in a percent difference of 7.0% between the simulation model and analytical model. The pressure drop obtained with the two models matched well and showed the validity of the simulation model. This model that is capable of calculating the pressure drop of a thermoplastic melt in a nozzle is critical in predicting the buckling of a filament according to Equation (2.5).

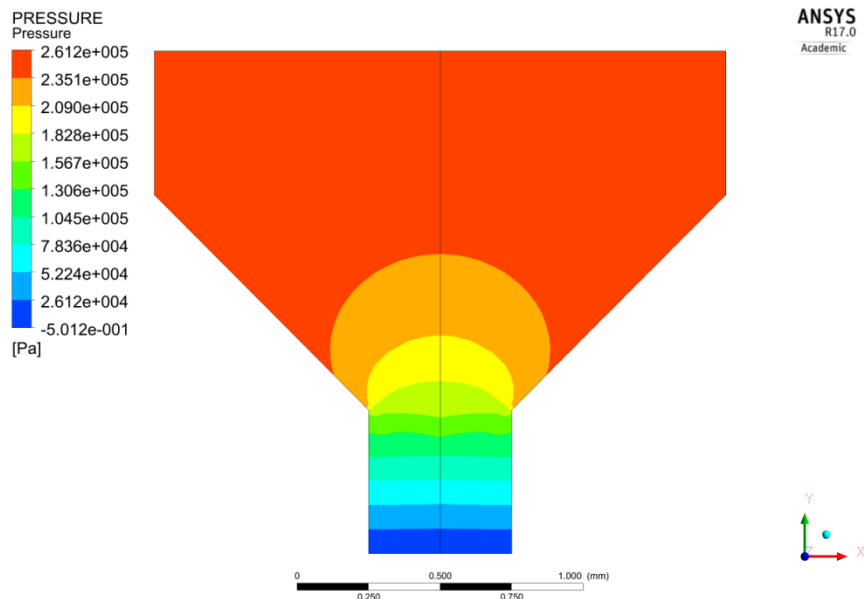


Figure 4.6 Pressure contour plot of the nozzle from a simulation model

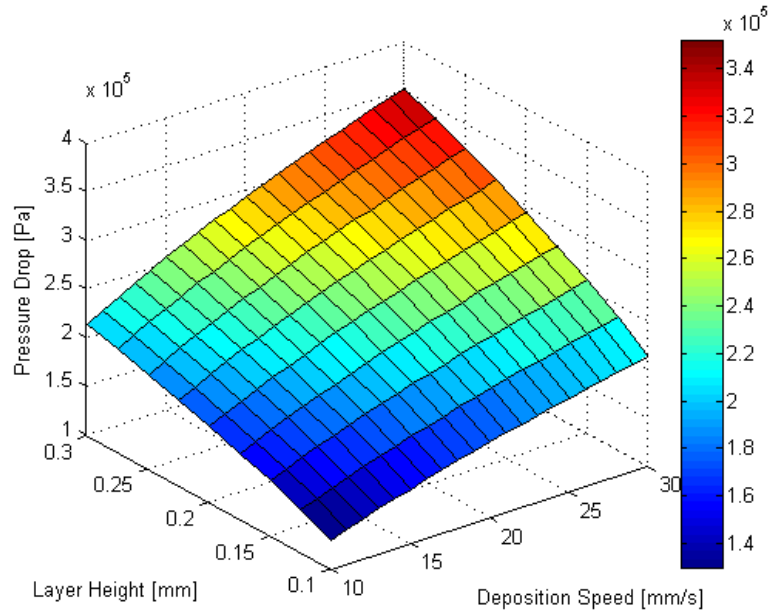
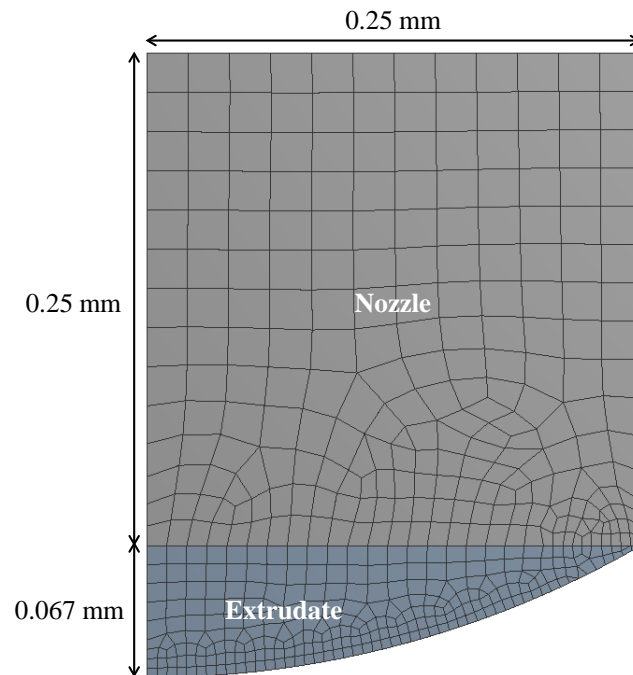


Figure 4.7 Pressure drop in the nozzle from an analytical model

4.2.3 Die Swell at the Nozzle Exit

The third stage of the material extrusion process was die swell at the nozzle exit. The geometry, mesh and boundary conditions are shown in Figure 4.8, which contained 541 nodes and 493 elements. The upper, linear region represented the end of the nozzle, so the top and right boundaries represented the nozzle walls. The lower, curved region represented the extruded filament, so the bottom boundary represented the free surface of the extruded filament. The left boundary was the axis of symmetry. This was a two-dimensional axisymmetric, non-isothermal problem, so the flow and thermal boundary conditions were labeled at every boundary. A time-dependent approach and a remeshing technique were also applied in order to predict the evolution of the geometry and temperature contour plot.

At the top boundary, as previous simulation models, a volumetric flow rate of $2 \times 10^{-9} \text{ m}^3/\text{s}$ was applied as the flow boundary condition. A constant temperature of $220 \text{ }^\circ\text{C}$ was applied as the thermal boundary condition, as it was determined from the liquefier simulation model shown in Figure 4.4. At the nozzle wall, zero wall velocity was selected as the flow boundary condition due to the adherence of melt to the nozzle wall. Again, a constant temperature of $220 \text{ }^\circ\text{C}$ was applied as the thermal boundary condition. At the free surface, the forces acting on the extruded filament were gravity and surface tension. The value of critical surface tension of polypropylene was 30.5 mJ/m^2 and this was used on the simulation model [44]. The free surface was also subjected to heat convection with air at $20 \text{ }^\circ\text{C}$. A typical range of convective heat transfer coefficient of air was 2 and $25 \text{ W/(m}^2\text{-}^\circ\text{C)}$ according to Incropera et al. [45], and the value was estimated to be $20 \text{ W/(m}^2\text{-}^\circ\text{C)}$ in the simulation model.



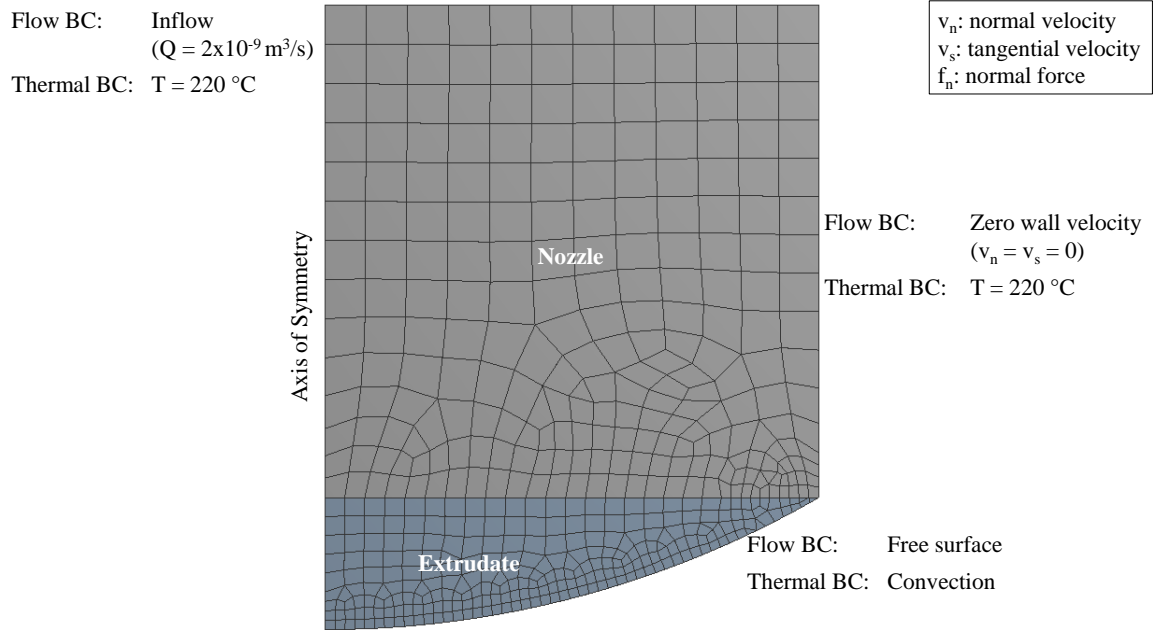


Figure 4.8 Geometry, mesh and boundary conditions of die swell at the nozzle exit

The evolution of the geometry as well as the temperature contour plot of the extruded filament is shown in Figure 4.9. The temperature contour plots were captured at various instants from 0.001 to 0.25 seconds.

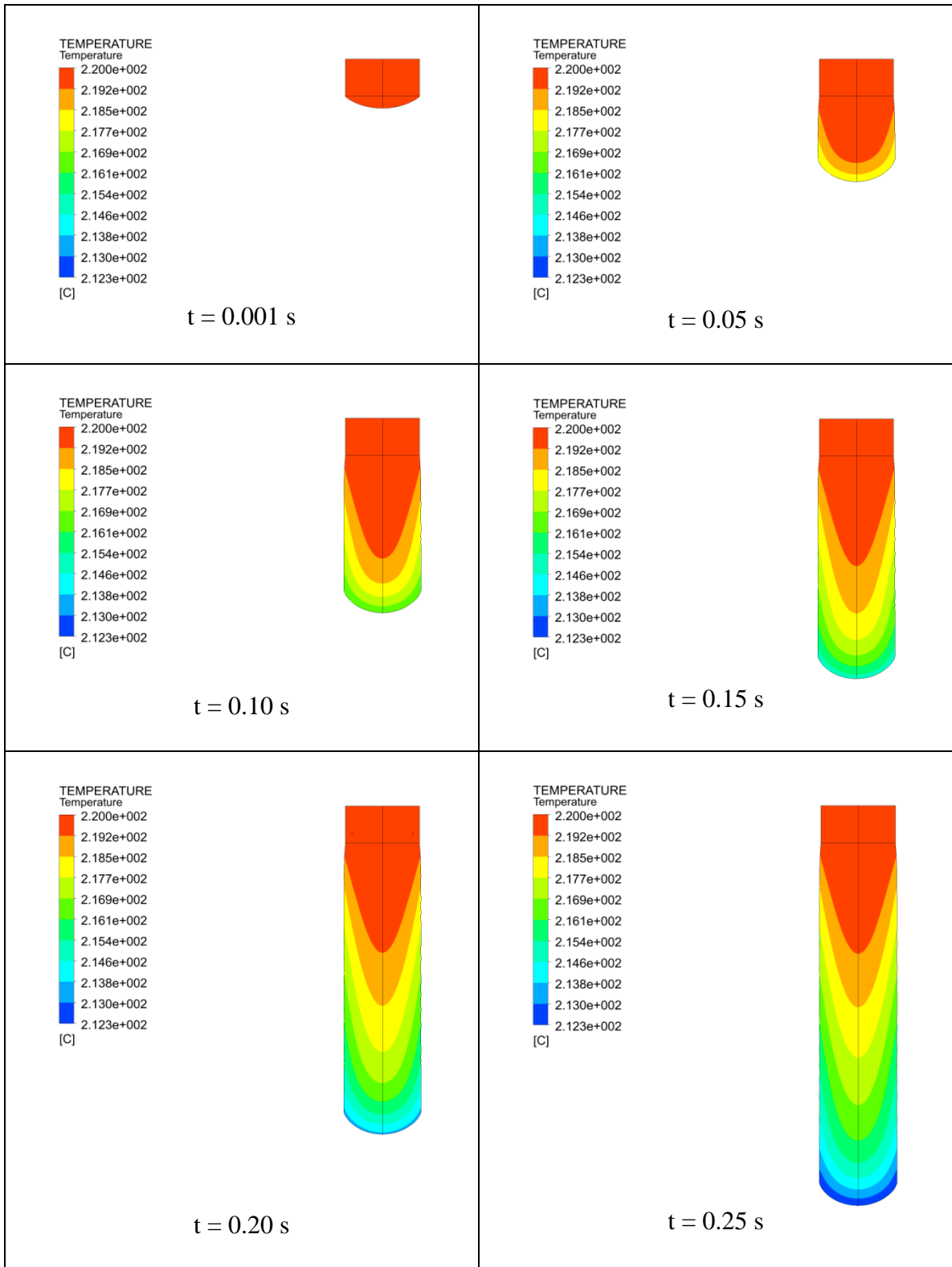


Figure 4.9 Temperature contour plot of die swell at the nozzle exit

Die swell, which refers to the expansion of the thermoplastic as it is extruded from the nozzle, is observed in Figure 4.9. The exit region of the nozzle and the extruded filament do not match exactly in shape and dimensions due to this phenomenon. The amount of die swell is expressed by the die swell ratio, B , defined as the ratio of the extrudate diameter to the nozzle diameter [46].

$$B = \frac{\text{Extrudate diameter}}{\text{Nozzle diameter}} \quad (4.2)$$

In order to confirm the validity of the model, the die swell ratios determined from the simulation model and experiments were compared. Figure 4.10 represents the die swell simulation model at 0.10 seconds. From the known nozzle diameter, the extrudate diameter was calculated to be 0.537 mm, and the die swell ratio was determined to be 1.074 as shown in Equation (4.3).

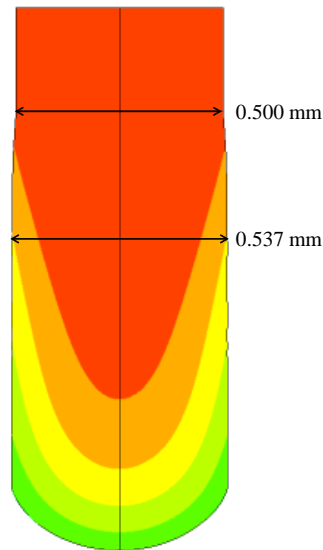


Figure 4.10 Die swell ratio calculation from a simulation model

$$B = \frac{0.537 \text{ mm}}{0.500 \text{ mm}} = 1.074 \quad (4.3)$$

Three images of filaments that were extruded on the HYREL System 30M machine are shown in Figures 4.11 a through c. While keeping the vertical distances between the nozzle diameter and extrudate diameter measurements the same as that in Figure 4.10, the extrudate diameters were calculated to be 0.568 mm, 0.551 mm and 0.561 mm, and the die swell ratios were determined to be 1.136, 1.102 and 1.122 as shown in Equations (4.4) through (4.6), respectively. The average die swell ratio of 1.120 was obtained from the experimental measurements, and this resulted in a percent difference of 4.1% between the simulation model and experiments. The die swell ratios calculated from the two models matched well and showed the validity of the simulation model.

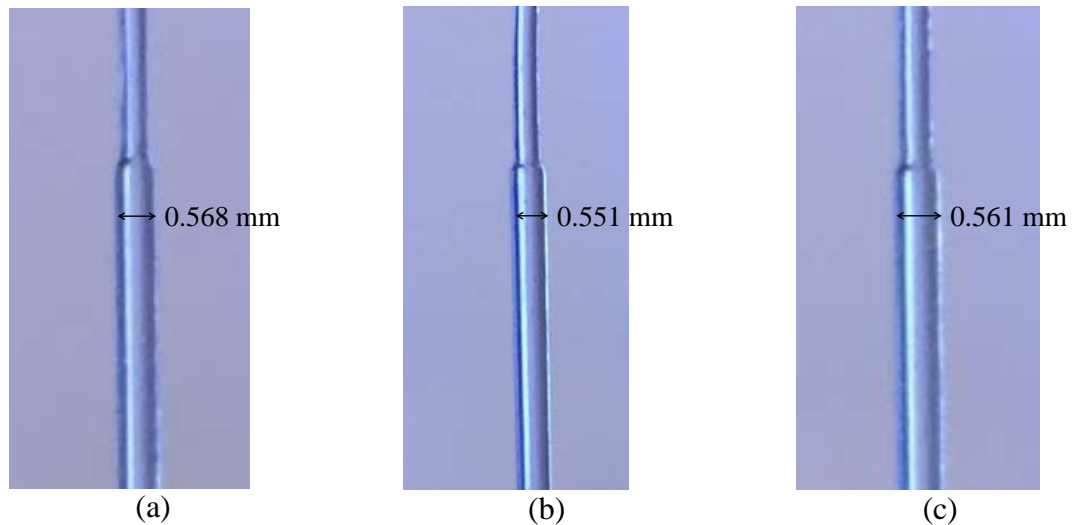


Figure 4.11 Die swell ratio calculations from experiments

$$B = \frac{0.568 \text{ mm}}{0.500 \text{ mm}} = 1.136 \quad (4.4)$$

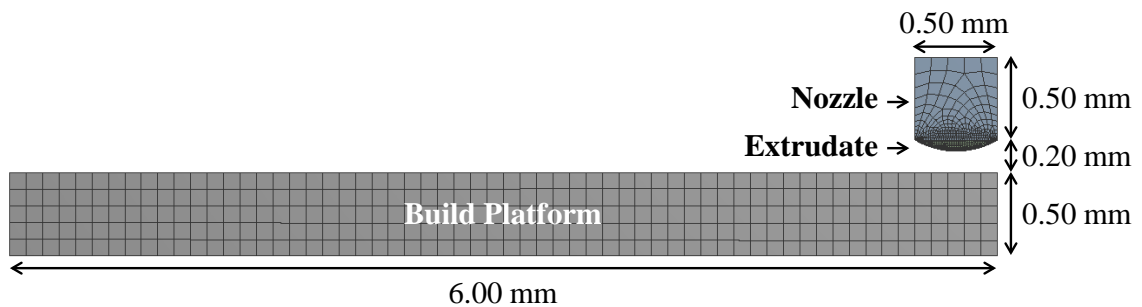
$$B = \frac{0.551 \text{ mm}}{0.500 \text{ mm}} = 1.102 \quad (4.5)$$

$$B = \frac{0.561 \text{ mm}}{0.500 \text{ mm}} = 1.122 \quad (4.6)$$

4.2.4 First Layer Deposition and Cooling

The fourth stage of the material extrusion additive manufacturing process was the deposition and cooling of the first layer of filament. In the first stage of this simulation model, the first layer was deposited onto a build platform. One of the differences between this simulation model and the die swell simulation model presented in Section 4.2.3 was that contact points needed to be defined between the extruded filament and build platform. In this case, the build platform was defined as a mold with constant and uniform temperature of 80 °C. The geometry, mesh and boundary conditions before the deposition are shown in Figure 4.12, which contained a total of 1,262 nodes and 1,140 elements. The top, right and left boundaries of the nozzle represented the nozzle walls, and the bottom boundary of the extrudate represented the free surface. This was a two-dimensional planar, time-dependent, non-isothermal problem, so the flow and thermal boundary conditions were labeled at every boundary. Since this was not an axisymmetric model, the cross sections of the entire nozzle, extrudate and build platform were modeled. A remeshing technique was also applied in order to predict the evolution of the temperature distribution and deposited filament shape.

At the top boundary, a volumetric flow rate of $4 \times 10^{-6} \text{ m}^3/\text{s}$ was applied as the flow boundary condition. This value was calculated using Equation (2.2) as the previous simulations. However, the width of the deposited road was assumed to be 1 m in this case because a simulation model with two-dimensional planar geometry was performed considering one-unit width geometry. A constant temperature of $220 \text{ }^\circ\text{C}$ was applied as the thermal boundary condition. The nozzle walls as well as the free surface were treated the same as the die swell simulation model. However, since there was no axis of symmetry in this case, the same flow and thermal boundary conditions were applied to the right and left nozzle walls. Also, in this simulation model, the filament was extruded through the nozzle in the vertical direction, while the deposition velocity was applied in the horizontal direction. In order to simulate the relative motion between the nozzle and the build platform, the nozzle was maintained in a fixed position, while the build platform translated in the horizontal direction with a deposition velocity.



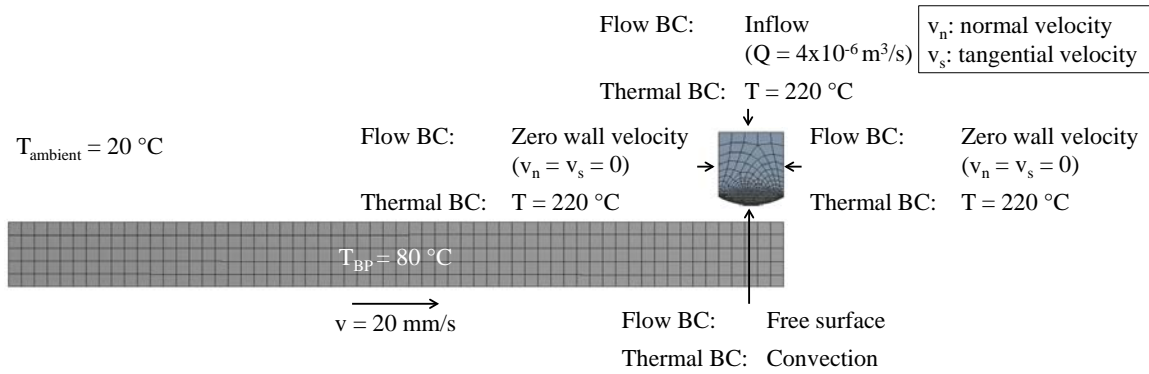


Figure 4.12 Geometry, mesh and boundary conditions before the first layer deposition

The second stage of this simulation model was the cooling of the first layer of filament. The geometry, mesh and boundary conditions before the cooling are presented in Figure 4.13, which contained a total of 11,739 nodes and 11,115 elements. In this case, the nozzle was removed and the extrudate was replaced by the first layer of filament, compared to the geometry presented in Figure 4.12. The temperature distribution and deposited filament shape after the first layer deposition were exported from the previous stage of the simulation model. Again, this was a two-dimensional planar, time-dependent, non-isothermal problem, so the flow and thermal boundary conditions were labeled at every boundary.

At the bottom surface of the first layer, zero wall velocity was selected as the flow boundary condition due to the adherence of the first layer to the build platform, and the build platform temperature of $80 \text{ }^\circ\text{C}$ was applied as the thermal boundary condition. The top, right and left surfaces represented free surfaces and they were subjected to cooling due to convection with air. In addition, since the cooling of the first layer of filament was simulated, the build platform was maintained in a fixed position in this model.

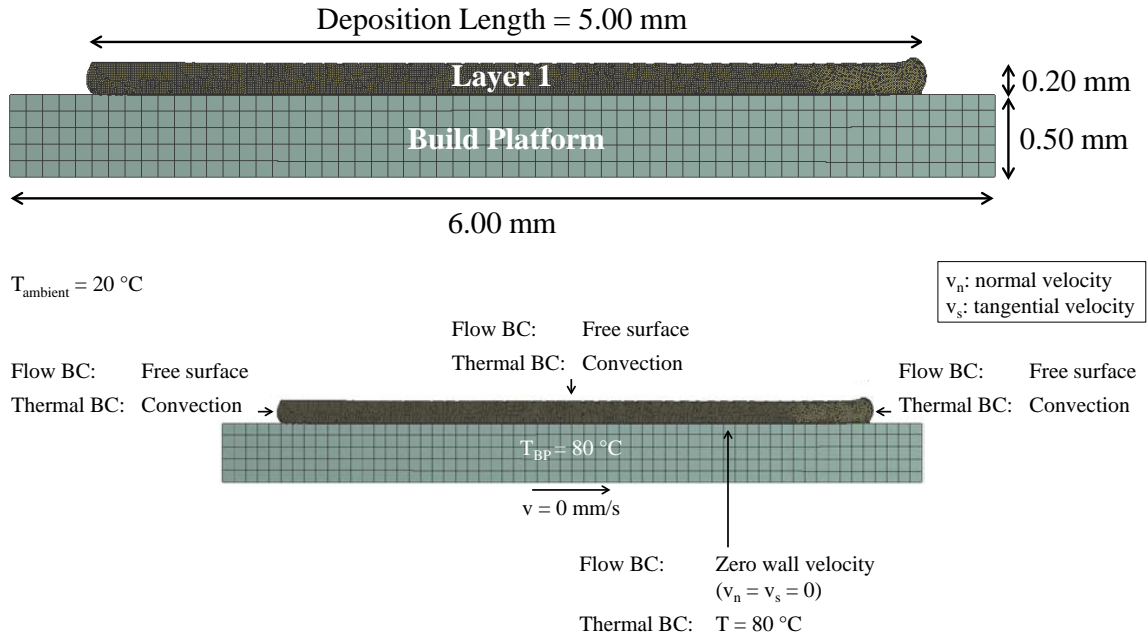


Figure 4.13 Geometry, mesh and boundary conditions before the first layer cooling

The evolution of temperature distribution and deposited filament shape during the first layer deposition is shown in Figure 4.14. The heat transfer coefficient of the build platform that was used in this simulation was $100\text{ W}/(\text{m}^2\text{-}^{\circ}\text{C})$. The results were captured at various instants from 0.001 to 0.25 seconds.

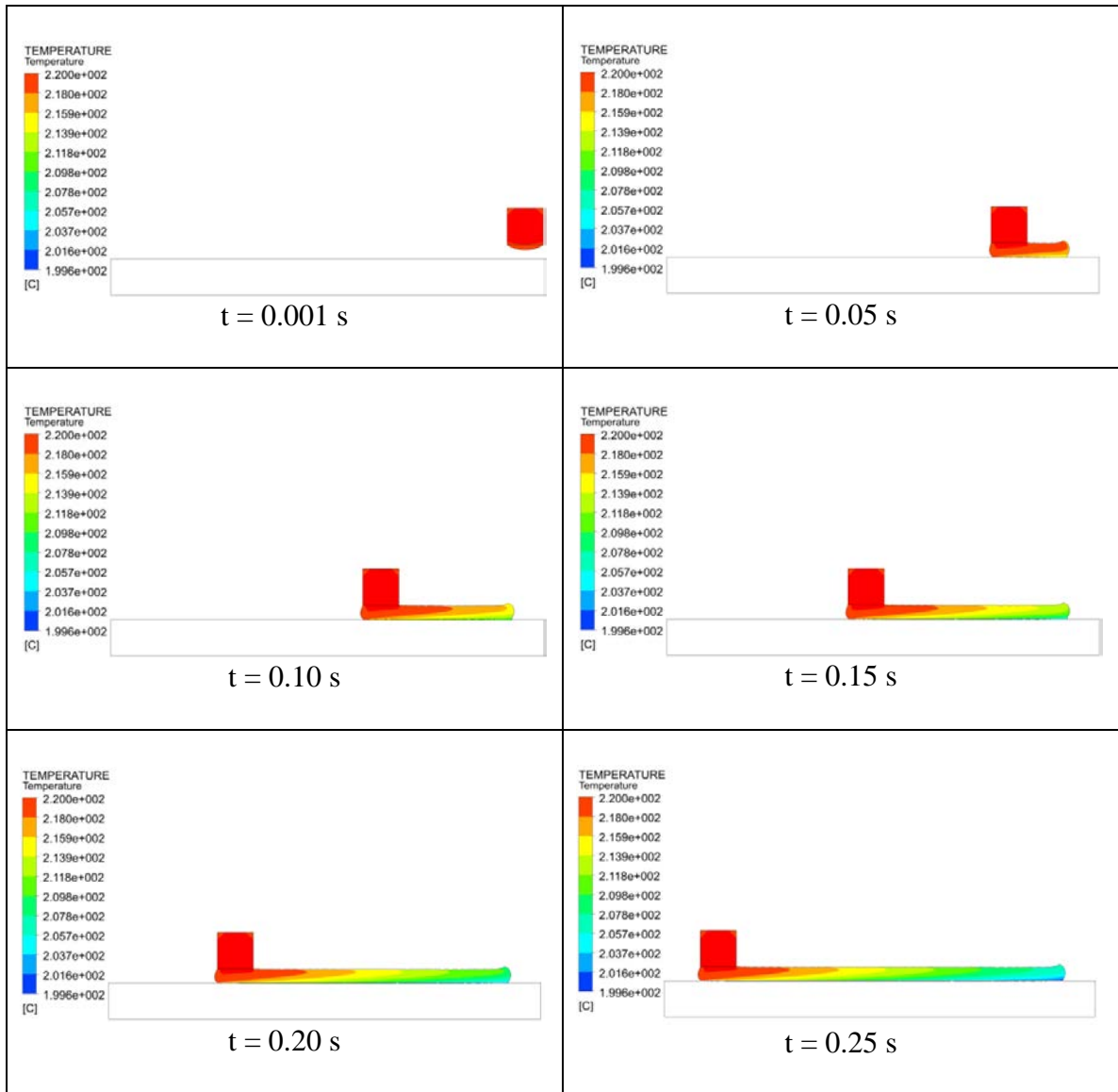


Figure 4.14 Temperature distribution and deposited filament shape during the first layer deposition

This model was compared to material extrusion of ceramics conducted by Bellini to confirm its validity [29]. As previously stated, the build platform heat transfer coefficient of $100 \text{ W}/(\text{m}^2 \cdot ^\circ\text{C})$ was used in the simulation in Figure 4.14. However, $10 \text{ W}/(\text{m}^2 \cdot ^\circ\text{C})$ was used for validation purposes, which was the value used in Bellini's model. A lower heat transfer coefficient was used in Bellini's model due to the

differences in the build platform material between the two models. The build platform was assumed to be made of insulated foam in Bellini's model, whereas a glass build platform was used in this study.

The temperature distributions and deposited filament shapes of the first layer obtained from this study and from Bellini's model are shown in Figure 4.15. Two temperature contour plots from this study were presented with two sets of process variable settings. For each contour plot, the deposition speed, deposition time, deposition length, maximum temperature, minimum temperature and temperature difference were listed. The top temperature contour plot from this study was the result after 0.0875 seconds in order to match the deposition length as Bellini's model, which was 1.75 mm. The bottom temperature contour plot from this study was the result after 0.25 seconds to facilitate the comparison of the contours since Bellini's model was run for 0.35 seconds.

Figure 4.15 depicts that the contours of the three simulation models are similar. However, the contours from this study seemed more extended compared to that of Bellini's model. This was most likely due to the difference in deposition speed. A typical deposition speed on material extrusion additive manufacturing machines was approximately 20 mm/s, but Bellini used 5 mm/s to facilitate the convergence of the simulation. The differences between the maximum and minimum temperatures were also compared. The temperature difference in Bellini's model was 2.0 °C, and those in the current study after 0.0875 seconds and 0.25 seconds were 4.8 °C and 10.2 °C, respectively. The temperature differences were close to each other between Bellini's model and the simulation model in this study, when the results were compared between the same deposition lengths. In addition, an increase in temperature difference was

expected with an increase in deposition time, and therefore deposition length, because the filament was subjected to cooling due to convection with air for a longer period of time. All of these comparisons were used to support the validity of the first layer deposition simulation model developed in this study.

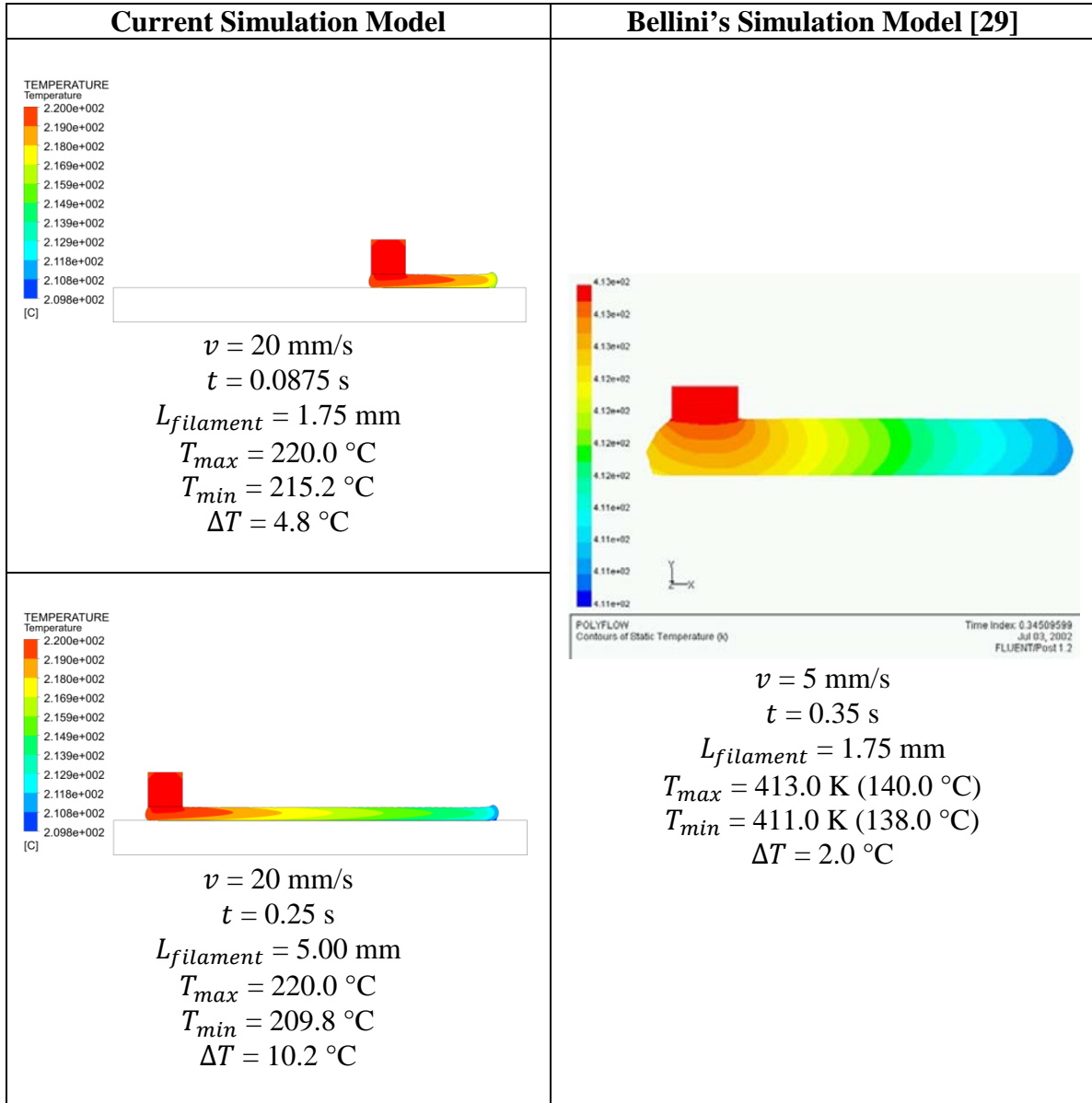


Figure 4.15 Differences between the current and Bellini's simulation models

The evolution of temperature distribution during the first layer cooling is shown in Figure 4.16. This step in the material extrusion process was simulated for 1.25 seconds to account for the horizontal movement of the printhead to its original location and the vertical movement of the build platform. In this simulation model, it was observed that the temperature of the first layer decreased from 220.0 °C to approximately 122.0 °C in 0.25 second, which was a 44.5% decrease.

The results were compared to the temperature profile of an ABS part measured using an infrared camera at Oak Ridge National Laboratory by Dinwiddie et al. as shown in Figure 4.17 [47]. In that study, a five-layer four-inch (101.6 mm) square was printed using a commercially available material extrusion additive manufacturing machine. The first layer was deposited at 170.0 °C and the temperature decreased to approximately 118.0 °C after 0.25 seconds, which was a 30.6% decrease. One of the reasons for the difference in percentage decrease could be due to the fact that the build platform in the simulation model was set to a slightly lower temperature than that at Oak Ridge National Laboratory. Since other critical information, such as the chamber temperature and deposition speed, were not provided in that study, it was difficult to determine other sources that caused the difference in percentage decrease. However, in both cases, exponential temperature decays were observed, and it only took a fraction of a second for the temperature of the first layer to reach steady state during the cooling process.

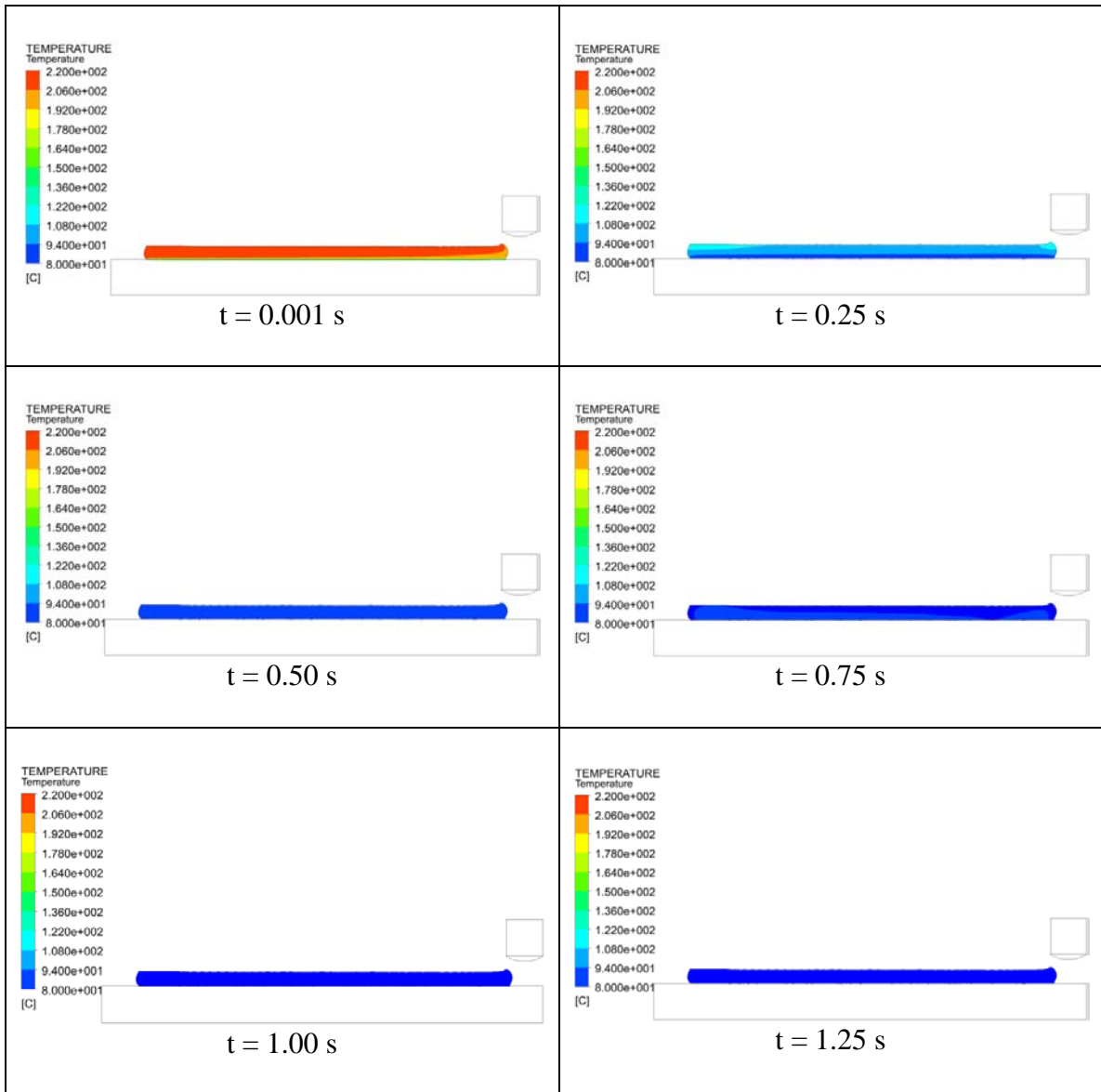


Figure 4.16 Temperature distribution during the first layer cooling

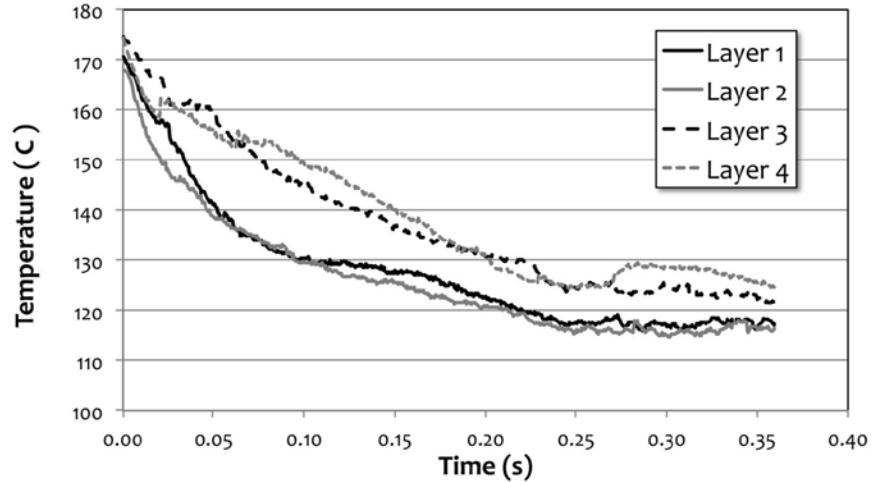


Figure 4.17 Temperature profiles of an ABS part measured using an infrared camera [47]

4.2.5 Second Layer Deposition and Cooling

The fifth stage of the material extrusion additive manufacturing process was the deposition of the second layer of filament on top of the first layer and the cooling of both layers. Once again, the temperature distribution after the first layer cooling was exported from the previous simulation. The geometry, mesh and boundary conditions before the second layer deposition are shown in Figure 4.18, which contained a total of 12,613 nodes and 11,931 elements. In this case, the nozzle and extrudate were added to the geometry presented in Figure 4.13 to allow for the second layer deposition. This was a two-dimensional planar, time-dependent, non-isothermal problem, so the flow and thermal boundary conditions were labeled at every boundary. The boundary conditions applied to the nozzle and extrudate were similar to those during the first layer deposition simulation model, and those applied to the first layer of filament were similar to those during the first layer cooling simulation model. The only difference in this model was

that the conduction heat transfer between the two layers was simulated in this stage. This was accomplished using the fluid-to-fluid contact capability in ANSYS® Polyflow.

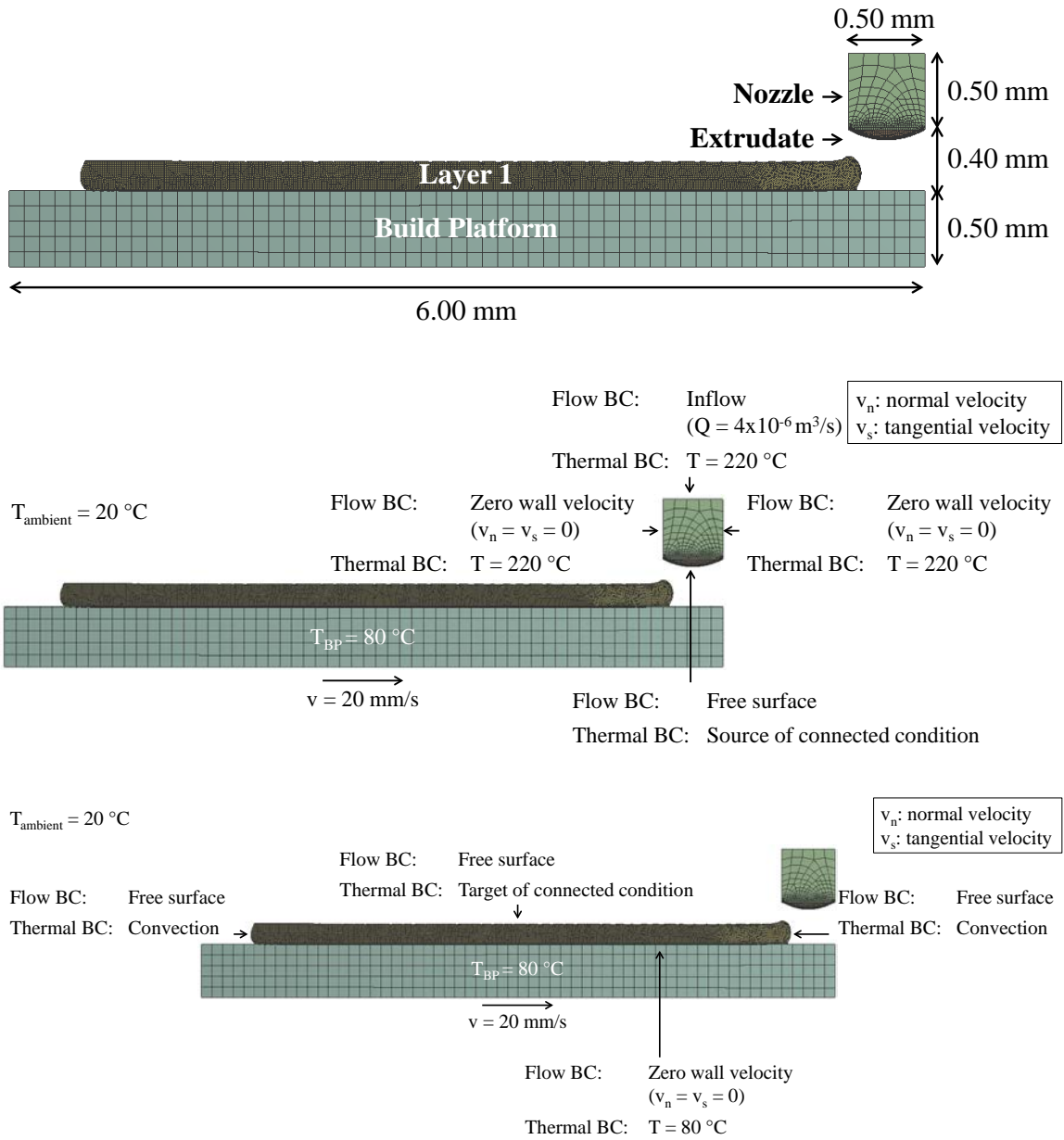


Figure 4.18 Geometry, mesh and boundary conditions before the second layer deposition

The temperature distributions and deposited filament shapes after the second layer deposition on top of the first layer were exported from the previous stage to accomplish the simulation model of the cooling of both layers. The geometry, mesh and boundary conditions before the cooling are presented in Figure 4.19, which contained a total of 66,563 nodes and 21,448 elements. In this case, the nozzle was removed and the extrudate was replaced by the second layer of filament, compared to the geometry presented in Figure 4.18. The transition from ANSYS® Polyflow to ANSYS® Mechanical occurred during this simulation model, so only thermal boundary conditions were applied at every boundary. The same thermal boundary conditions used in the first layer cooling simulation model were used in this case, which were the build platform temperature of 80 °C at the bottom surface of the first layer, and the top, right and left surfaces were subjected to cooling due to convection with air.

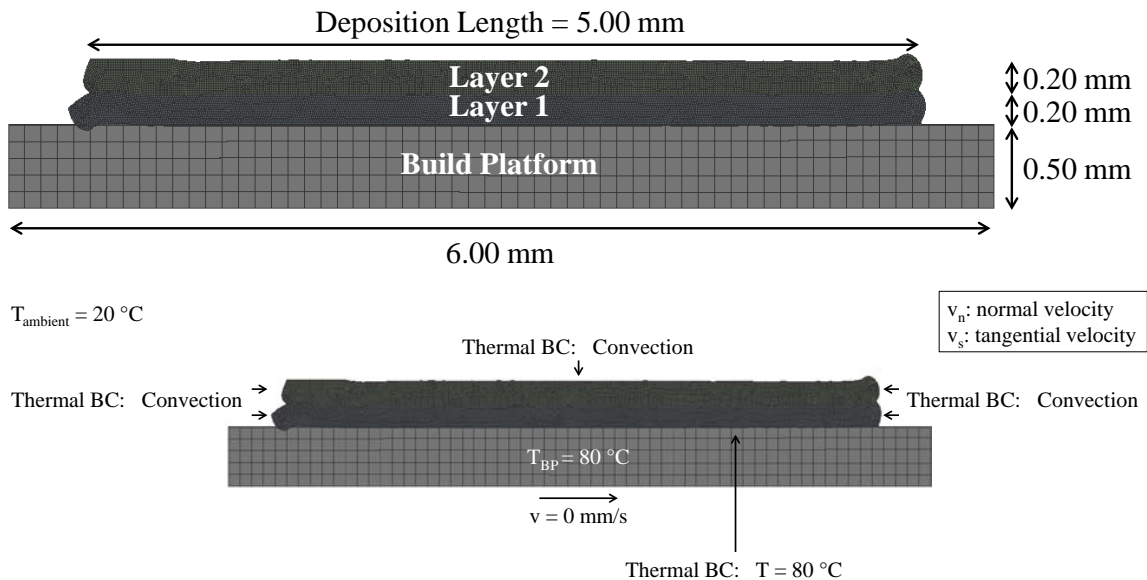


Figure 4.19 Geometry, mesh and boundary conditions before the first and second layer cooling

The evolutions of temperature distributions and deposited filament shapes during the second layer deposition and the two-layer cooling are shown in Figure 4.20 and Figure 4.21, respectively. As previously stated, the procedure for this simulation model was similar to that for the first layer deposition and cooling. However, the conduction heat transfer between the two layers was simulated using the fluid-to-fluid contact capability in ANSYS® Polyflow.

From Figure 4.21, it was observed that the temperature of the two layers decreased from 220.0 °C to approximately 169.1 °C in 0.25 seconds, which was a 23.1% decrease. As it was done for the first layer cooling simulation model, this result was compared to the temperature profile of an ABS part as shown in Figure 4.17 [47]. In an experiment conducted at Oak Ridge National Laboratory, the second layer was deposited at 170.0 °C and the temperature decreased to approximately 117.0 °C after 0.25 seconds, which was a 31.2% decrease. In addition, exponential temperature decays were once again observed in both the simulation model developed in this study and the experiment conducted at Oak Ridge National Laboratory.

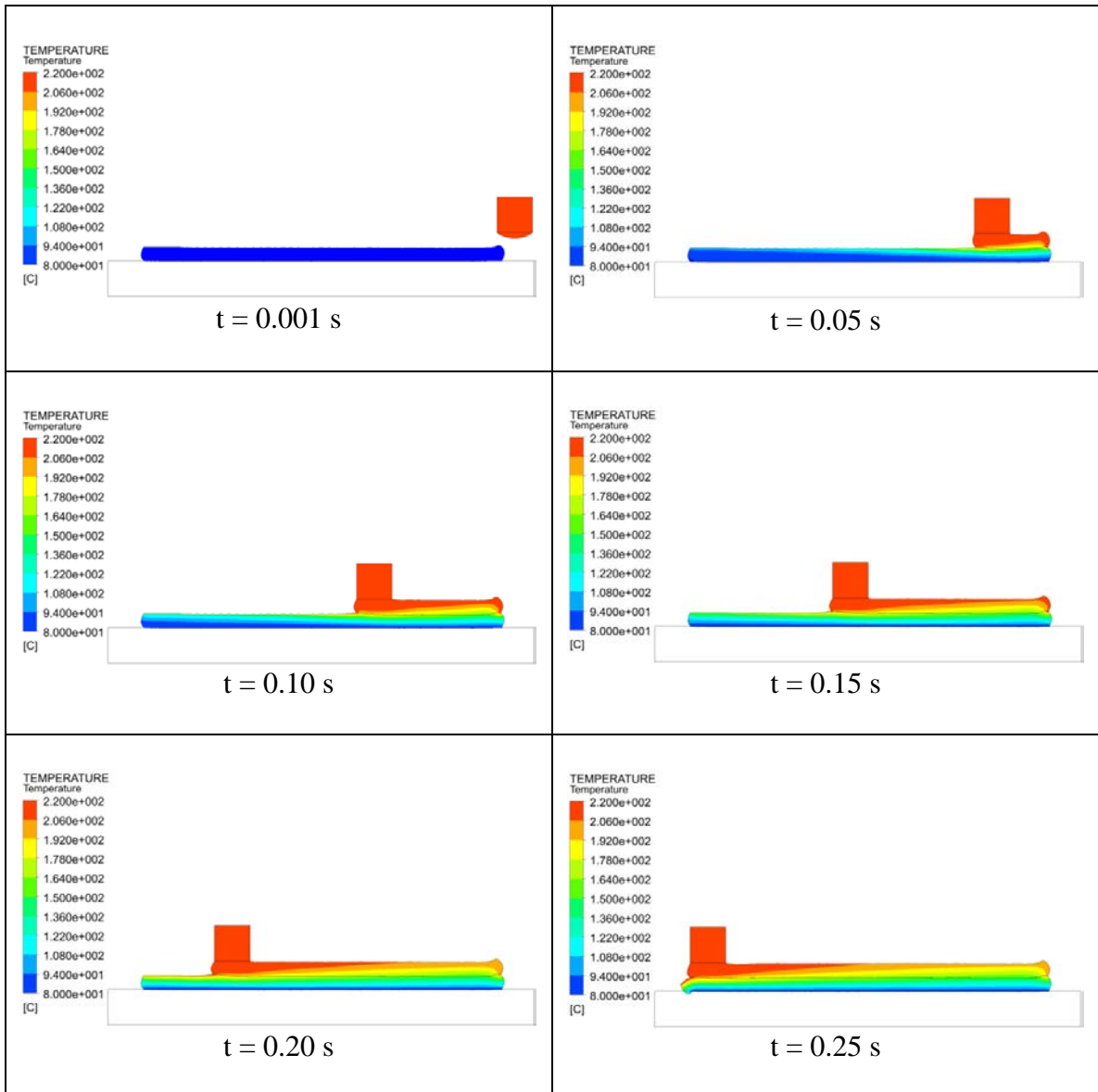


Figure 4.20 Temperature distribution and deposited filament shape during the second layer deposition

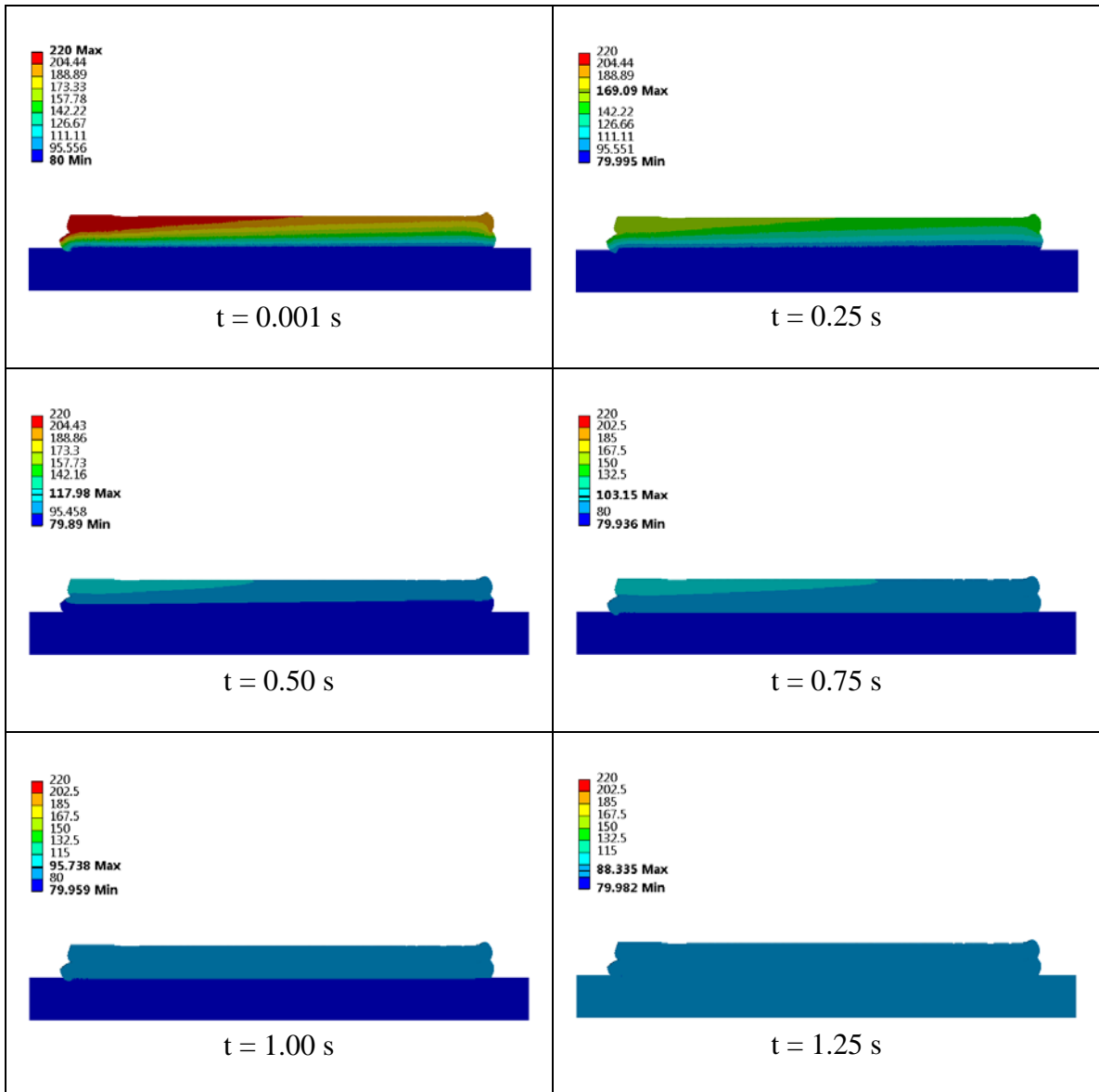
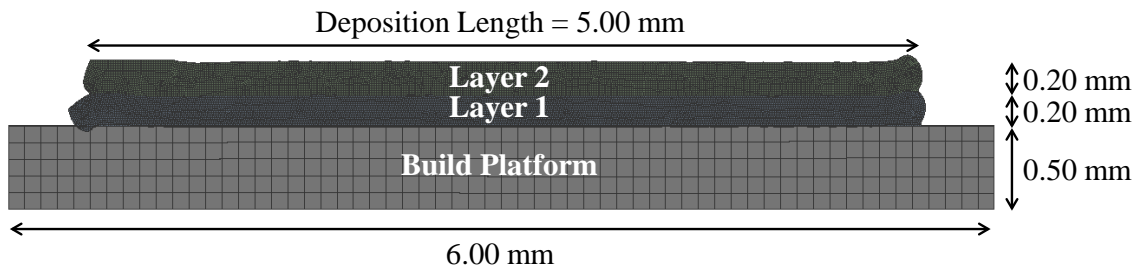


Figure 4.21 Temperature distribution during the two-layer cooling

4.2.6 Residual Stress/Warpage

The last process simulation model determined the residual stress and warpage/deformation of the deposited two layers of filaments. During the material extrusion process, the part goes through a repetition of heating and cooling as the filament is liquefied in the liquefier chamber and is deposited onto a build platform to

fabricate a three-dimensional part. This layer-by-layer fabrication procedure causes residual stresses to accumulate in the part. This simulation model focused on predicting thermally-induced residual stress caused by the crystallization of the material during the cooling process, which led to part warpage. Therefore, the temperature distributions obtained from the two-layer cooling simulation model were linked to this simulation model in ANSYS® Mechanical to conduct structural analyses. The geometry and mesh for the two-layer cooling simulation model, which contained a total of 66,563 nodes and 21,448 elements, were also used for the residual stress/warpage simulation model. They are shown in Figure 4.22 along with the boundary conditions. When the geometry was imported into ANSYS® Mechanical, the nodes at the bottom surface of the first layer and those at the top surface of the build platform were in contact. These nodes were first decoupled then only coupled at the mid-point of the bottom surface of the first layer. By fixing this node to the build platform and applying zero force everywhere else, the residual stress and warpage similar to experimentally fabricated parts during the cooling process were computed.



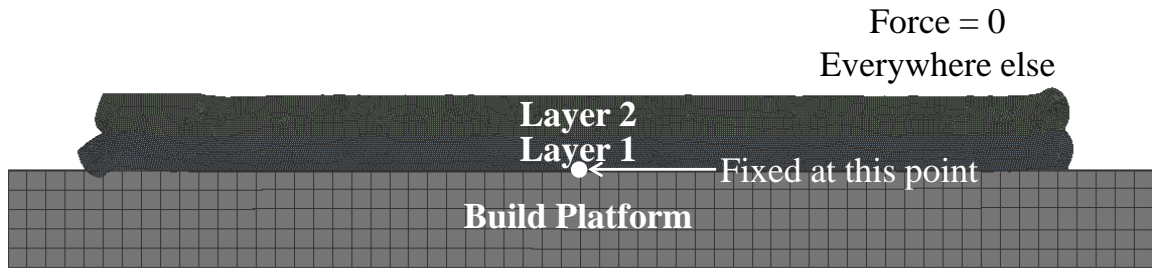


Figure 4.22 Geometry, mesh and boundary conditions before the residual stress/warpage simulation

The residual stress and warpage of the deposited two layers of filaments at steady state are presented in Figure 4.23 and Figure 4.24, respectively. These simulation model results were validated with experimental results as shown in Figure 4.24 b, which will be discussed in Section 4.3.

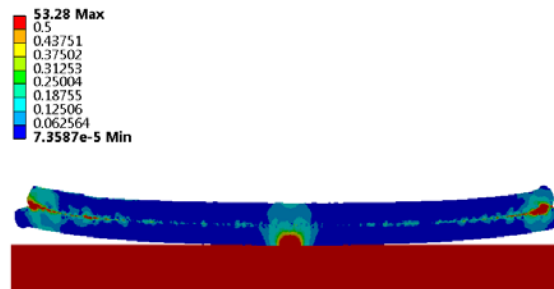


Figure 4.23 Residual stress at steady-state

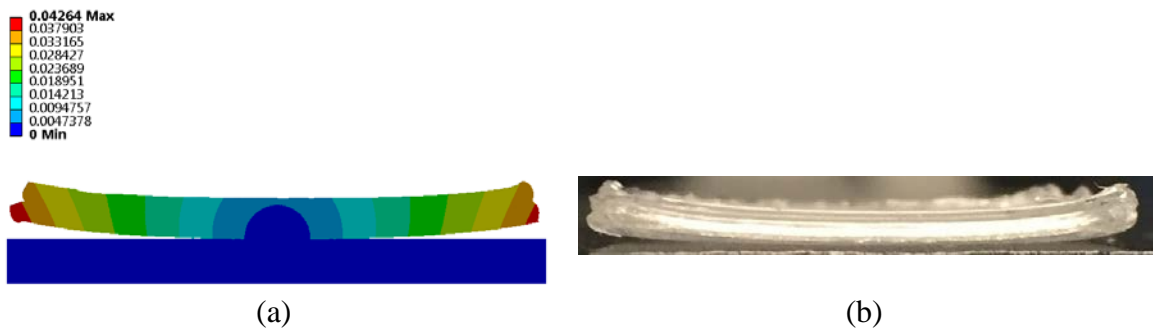


Figure 4.24 Warpage at steady-state from (a) a simulation model and (b) an experiment

4.3 Parametric Studies and Validations of Warpage Process Simulation Model

In this section, parametric studies of warpage process simulation model were conducted in order to determine which process variable settings on material extrusion additive manufacturing machines and which material properties of polypropylene-based composite materials affect the warpage characteristics of the fabricated parts. The effects of adjusting process variable settings, such as deposition temperature, deposition speed and layer height, on part warpage were analyzed computationally and validated with experimental results. Similarly, the effects of varying material properties, such as coefficient of thermal expansion and thermal conductivity, on part warpage were investigated computationally.

4.3.1 Geometry Discrepancies between Simulation Models and Experiments

Two different geometries were used for the simulation models and experiments as shown in Figure 4.25. Since the simulation models were computationally intensive, two layers of filaments that were 5 mm in length were simulated, whereas five layers of filaments that were 20 mm in length were fabricated in the experiments. The fabrication of a larger part in experiments also facilitated the part warpage measurement using a caliper. However, these geometry differences led to differences in part warpage values between the simulation models and experiments as well. The experiment measurements, therefore, needed to be extrapolated in order to account for the geometry differences. The parametric studies of the warpage simulation model were conducted by applying the extrapolation methods to determine the effects of adjusting process variable settings and material properties on part warpage.

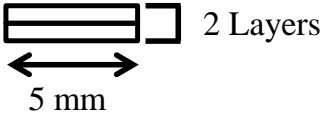
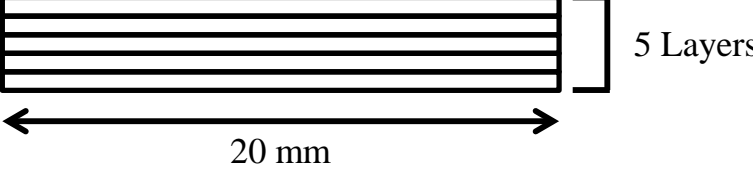
Simulation Models (2-D)	Experiments (3-D)
	

Figure 4.25 Geometry differences in simulation models and experiments

First, in order to account for the differences in deposition length, the radius of curvature was considered. The radius of curvature, r , was calculated using Equation (4.7):

$$r = \frac{H}{2} + \frac{W^2}{8H} \quad (4.7)$$

where W is the deposition length and H is the measured warpage. Assuming the radius of curvature to be a constant, the warpage was then extrapolated by decreasing the deposition length to match with that of the simulation models. This extrapolation method is described using an example in Figure 4.26. In this example, the measured warpage from experiments was assumed to be 1 mm. The radius of curvature was calculated and plotted in blue. When the deposition length was decreased from 20 mm to 5 mm as in experiments to simulation models, the extrapolated warpage was calculated to be 0.06 mm, which was 94% less than the original value. The extrapolated warpage was plotted in red.

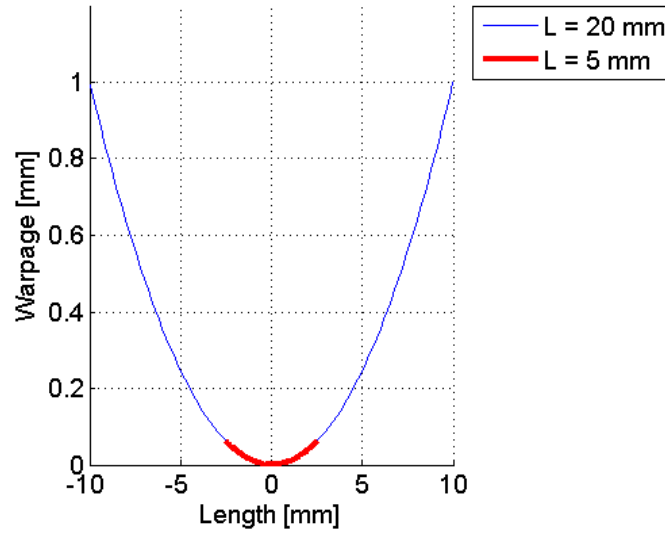


Figure 4.26 Example plot of warpage vs. deposition length

In addition, the number of layers also affected the warpage since it was related to the number of repetition of heating and cooling the part experienced during the material extrusion process. Using the simulation models presented in Section 4.2, the warpage values were simulated by varying the number of layers from one to five. The results are plotted in Figure 4.27. As the number of layers decreased from five to two as in experiments to simulation models, the warpage decreased by 6% from 0.0452 mm to 0.0426 mm.

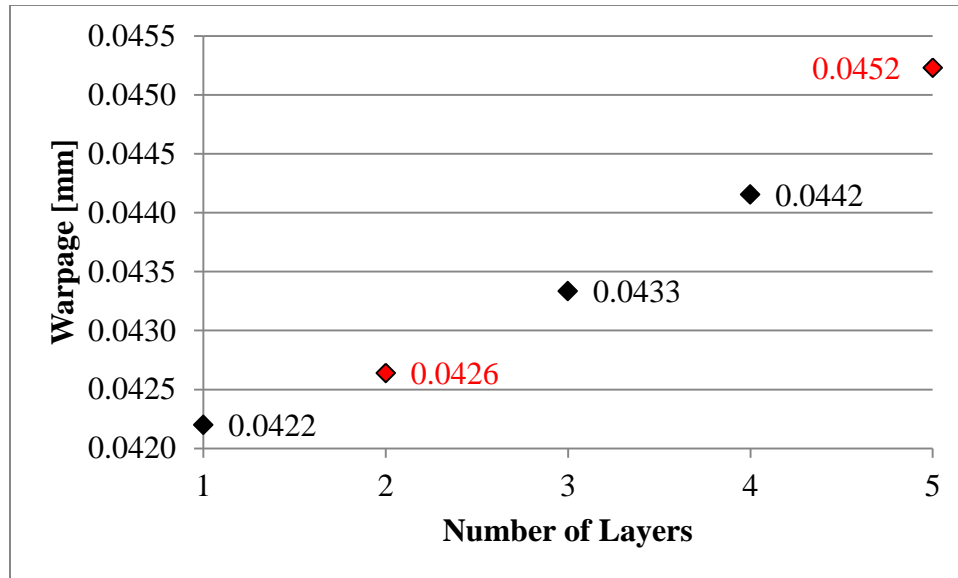


Figure 4.27 Plot of warpage vs. number of layers from simulation models

4.3.2 Process Variable Settings

The process variable settings, such as deposition temperature, deposition speed and layer height, that are representative of the material extrusion process were selected and used on the parametric studies of warpage simulation model. These values are presented in Table 4.2.

Table 4.2 Process variable settings for parametric studies

Process Variable Settings	Simulation Model Input Values		
	Deposition Temperature	200 °C	220 °C
Deposition Speed	10 mm/s	20 mm/s	30 m/s
Layer Height	0.1 mm	0.2 mm	0.3 mm

4.3.2.1 Deposition Temperature

The effect of increasing the deposition temperature from 200 °C to 240 °C on part warpage was first determined. The plot of experimentally measured warpage at various deposition temperatures is shown in Figure 4.28, and the experimental and simulation model warpage values are summarized in Table 4.3. The extrapolated experimental results and simulation model results were comparable in values and followed the same trend. However, varying deposition temperature did not have significant effects on warpage. One of the reasons for this could be due to a small range of temperature representative of the material extrusion process. Part warpage was related to the temperature difference between deposition temperature and build platform temperature, which was calculated to be 120 °C using the minimum deposition temperature and 160 °C using the maximum deposition temperature. The difference between the two temperature differences was 40 °C and the percent difference was only 25.0%.

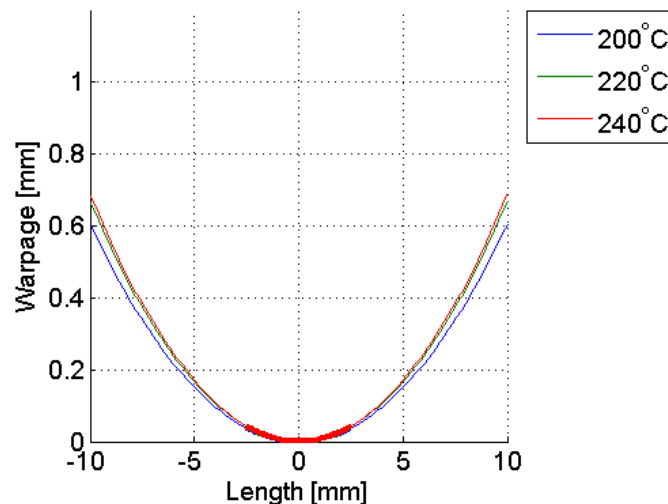


Figure 4.28 Plot of experimental warpage with varying deposition temperature

Table 4.3 Experimental and simulation model warpage with varying deposition temperature

Process Variable Settings	Deposition Temperature		200 °C	220 °C	240 °C
	Deposition Speed		20 mm/s		
	Layer Height		0.2 mm		
Warpage	Experiment	Measured	0.61 ± 0.10 mm	0.67 ± 0.30 mm	0.69 ± 0.31 mm
		Extrapolated	0.0355 mm	0.0391 mm	0.0403 mm
	Process Simulation Model		0.0410 mm	0.0426 mm	0.0437 mm

The experimentally measured values in Table 4.3 represents those measured using a caliper. In order to verify the accuracy of these values, the part warpage was also measured using an optical comparator (Starrett HB400 Horizontal Benchtop Optical Comparator [48]), as shown in Figure 4.29. The caliper measurements were compared to the optical comparator measurements and the data are summarized in Table 4.4. In all cases, the optical comparator values were slightly higher than the caliper measurements. The difference between the two methods could be due to the amount of force applied to the test specimens, since a small amount of force on the test specimens was inevitable using a caliper, whereas no force was applied when measured using an optical comparator. However, the results were reasonably similar and the difference between the average caliper and optical comparator measurements were within 10% at each deposition temperature. In addition, the optical comparator results also showed that varying deposition temperature did not have significant effects on part warpage. As previously stated, this was most likely due to a small deposition temperature range representative of this process, and the results validated the caliper part warpage measurements.



Figure 4.29 Part warpage measurement using an optical comparator

Table 4.4 Caliper and optical comparator warpage measurements

Process Variable Settings	Deposition Temperature		200 °C	220 °C	240 °C
	Deposition Speed		20 mm/s		
	Layer Height		0.2 mm		
Warpage	Experiment	Caliper	0.61 ± 0.10 mm	0.67 ± 0.30 mm	0.69 ± 0.31 mm
		Optical Comparator	0.65 ± 0.18 mm	0.72 ± 0.22 mm	0.76 ± 0.35 mm

4.3.2.2 Deposition Speed

The effect of increasing the deposition speed from 10 mm/s to 30 mm/s on part warpage was also determined. The plot of experimentally measured warpage at various deposition speeds is shown in Figure 4.30, and the experimental and simulation model warpage values are summarized in Table 4.5. The extrapolated experimental results and

simulation model results showed good correlations and followed the same trend, which was an increase in deposition speed led to a decrease in warpage. This phenomenon was likely related to the temperature gradient within each layer of filament. With a lower deposition speed, a longer time was required for the deposition process to be completed for one layer. This led to a larger temperature gradient within that layer, and therefore higher warpage. In contrast, with a higher deposition speed, it took a shorter time to complete the deposition of one layer. This led to a smaller temperature gradient within the layer, and therefore, a lower warpage.

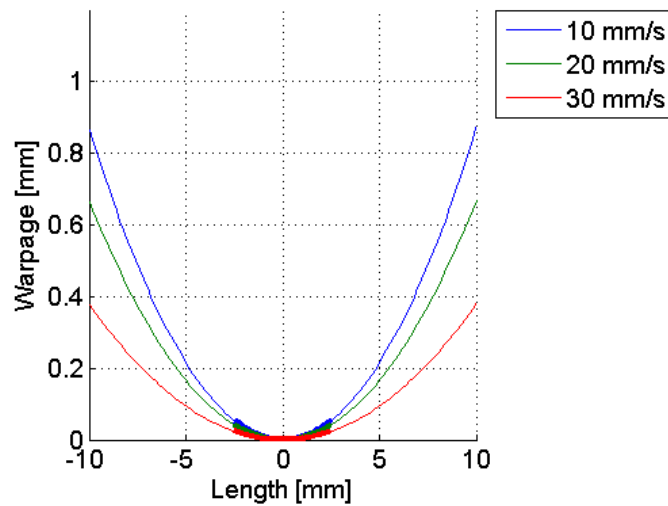


Figure 4.30 Plot of experimental warpage with varying deposition speed

Table 4.5 Experimental and simulation model warpage with varying deposition speed

Process Variable Settings	Deposition Temperature		220 °C		
	Deposition Speed		10 mm/s	20 mm/s	30 mm/s
	Layer Height		0.2 mm		
Warpage	Experiment	Measured	0.87 ± 0.28 mm	0.67 ± 0.30 mm	0.38 ± 0.19 mm
		Extrapolated	0.0510 mm	0.0391 mm	0.0223 mm
	Process Simulation Model		0.0532 mm	0.0426 mm	0.0323 mm

4.3.2.3 Layer Height

Finally, the effect of increasing the layer height from 0.1 mm to 0.3 mm on part warpage was determined. The plot of experimentally measured warpage at various layer heights is shown in Figure 4.31, and the experimental and simulation model warpage values are summarized in Table 4.6. Once again, the extrapolated experimental results and simulation model results showed good correlations and followed the same trend, which was an increase in layer height led to a decrease in warpage. This phenomenon was likely related to the temperature gradient within multiple layers of filaments. Since the number of layers was kept constant, a lower layer height resulted in a thinner fabricated part. This meant that a part with a lower layer height cooled more quickly compared to that with a higher layer height, which led to higher warpage.

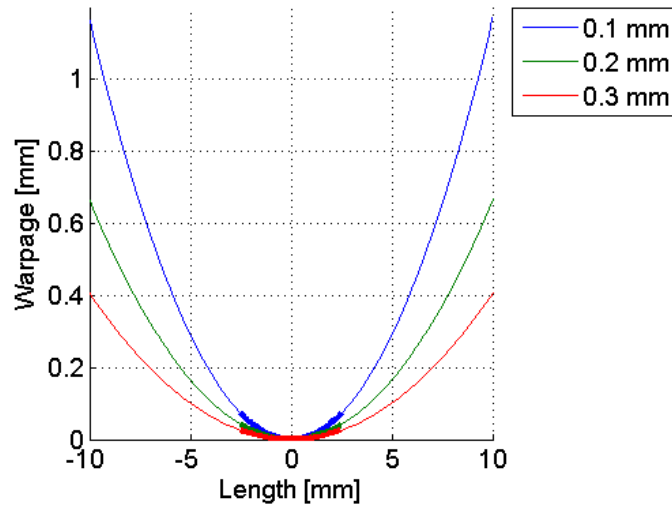


Figure 4.31 Plot of experimental warpage with varying layer height

Table 4.6 Experimental and simulation model warpage with varying layer height

Process Variable Settings	Deposition Temperature		220 °C		
	Deposition Speed		20 mm/s		
	Layer Height		0.1 mm	0.2 mm	0.3 mm
Warpage	Experiment	Measured	1.17 ± 0.59 mm	0.67 ± 0.30 mm	0.41 ± 0.20 mm
		Extrapolated	0.0682 mm	0.0391 mm	0.0240 mm
	Process Simulation Model		0.0621 mm	0.0426 mm	0.0314 mm

4.3.3 Material Properties

The material properties, such as coefficient of thermal expansion and thermal conductivity, of a neat polypropylene-based polymer and polypropylene-based composite materials were selected and used on the parametric studies of warpage simulation model. These values are presented in Table 4.7. In order to determine the effects of a specific material property on part warpage, that material property of the reference material, Polypropylene C, was replaced with that of another material. For example, in order to see the effect of coefficient of thermal expansion on part warpage, that of Polypropylene C1 and other material properties of Polypropylene C were combined in one simulation model. However, there exists no such material in reality, so the simulation model results in this section could not be validated with experiments. Nonetheless, these results will be beneficial in understanding which material properties to take into considerations during the new composite material development process in order to reduce part warpage.

Table 4.7 Material properties for parametric studies

Material Properties	Simulation Model Input Values	
Coefficient of Thermal Expansion	CTE of Polypropylene C (Figure 3.8)	CTE of Polypropylene C1 (Figure 3.8)
Thermal Conductivity	Thermal conductivity of Polypropylene C (0.24 W/(m-°C))	Thermal conductivity of Polypropylene D3 (0.57 W/(m-°C))

4.3.3.1 Coefficient of Thermal Expansion

The effect of varying coefficient of thermal expansion on part warpage was determined. The CTE values of Polypropylenes C and C1 were applied to the simulation model, and the warpage values are summarized in Table 4.8. In Section 3.4.2, the CTE experimental data as a function of temperature were presented for a temperature range between 20 °C and 90 °C. The results could not be obtained above this temperature using a dilatometer since the test specimens were softened and deformed. Howe et al. reported a constant coefficient of thermal expansion of $6.7 \times 10^{-4} \text{ m}/(\text{m}\cdot^\circ\text{C})$ for polypropylene in the melt [42]. Therefore, for the CTE values of Polypropylene C in this simulation model, a linear interpolation method was applied from the experimental value at 90 °C to $6.7 \times 10^{-4} \text{ m}/(\text{m}\cdot^\circ\text{C})$ at the melting temperature, and this constant CTE value was applied above the melting temperature. A similar approach was used for Polypropylene C1 except the constant CTE value in the melt was estimated to be $3.35 \times 10^{-4} \text{ m}/(\text{m}\cdot^\circ\text{C})$. A half of the melt CTE of Polypropylene C was calculated because the experimental CTE data of Polypropylene C1 were about a half of those of Polypropylene C.

The results showed that by decreasing the CTE values by a factor of two, the part warpage decreased by 60.8%. As discussed in Section 2.3, the warping decreased

drastically by the addition of carbon fiber into ABS due to a decrease in the coefficient of thermal expansion. A decrease in CTE led to a decrease in the strain that the part experienced as it cooled from the deposition temperature to ambient temperature. This agreed with the simulation model results, and confirmed that coefficient of thermal expansion is a critical material property to consider in order to reduce part warpage.

Table 4.8 Simulation model warpage with varying coefficient of thermal expansion

Material Properties	Coefficient of Thermal Expansion	CTE of Polypropylene C (Figure 3.8)	CTE of Polypropylene C1 (Figure 3.8)
	Thermal Conductivity	Thermal conductivity of Polypropylene C (0.24 W/(m·°C))	
Warpage	Process Simulation Model	0.0426 mm	0.0167 mm

4.3.3.2 Thermal Conductivity

The effect of varying thermal conductivity on part warpage was also determined. The thermal conductivity values of Polypropylenes C and D3 were applied to the simulation mode, and the warpage values are summarized in Table 4.9. Polypropylene D3 was selected because it was the only polypropylene-based composite material with a significantly higher thermal conductivity compared to neat polypropylene-based polymers, Polypropylenes C and D, as shown in Figure 3.13 and Figure 3.14. Although the experimental data showed thermal conductivity as a function of temperature, it stayed fairly consistent so the average temperature of each material was applied to the simulation models.

The results showed that by increase the thermal conductivity by approximately 137.5%, the part warpage decreased by 10.1%. Another reason for a decrease in warping with the addition of carbon fiber into ABS, as discussed in Section 2.3, was an increase in thermal conductivity. An increase in thermal conductivity led to a decrease in thermal gradients throughout the part. Although the result was not as significant in this case with a change in thermal conductivity as it was with a change in CTE, thermal conductivity still plays a critical role in warpage reduction.

Table 4.9 Simulation model warpage with varying thermal conductivity

Material Properties	Coefficient of Thermal Expansion	CTE of Polypropylene C (Figure 3.8)	
	Thermal Conductivity	Thermal conductivity of Polypropylene C (0.24 W/(m-°C))	Thermal conductivity of Polypropylene D3 (0.57 W/(m-°C))
Warpage	Process Simulation Model	0.0426 mm	0.0383 mm

4.4 Summary

Material extrusion process simulation models that are capable of predicting temperature distributions, deposited filament shapes, residual stresses and warpages of fabricated parts were presented in this chapter. These models consisted of six stages of the material extrusion process: melt flow in the liquefier chamber, extrusion through the nozzle, die swell at the nozzle exit, first layer deposition and cooling, second layer deposition and two-layer cooling and warpage. Each process simulation model was

presented and validated by comparison with analytical models, experiments or literature results.

In addition, parametric studies of the warpage simulation model were conducted to determine the effects of process variable settings and material properties on part warpage. For process variable settings, deposition temperature, deposition speed and layer height were considered, and for material properties, coefficient of thermal expansion and thermal conductivity were investigated. The results were as follows:

- No significant effects on part warpage as deposition temperature increased
- Part warpage decreased as deposition speed increased
- Part warpage decreased as layer height increased
- Part warpage decreased as coefficient of thermal expansion decreased
- Part warpage decreased as thermal conductivity increased

The proposed material extrusion process simulation models provided promising results as the basis for screening new materials computationally.

CHAPTER 5

MECHANICAL PROPERTY ANISOTROPY AND BONDING

STRENGTH

5.1 Introduction

Chapter 5 focuses on mechanical property anisotropy and its relationship to the bonding quality of the extruded filaments. Section 5.2 presents the scanning electron microscope (SEM) images of two polypropylene-based composite materials. Since the surface finish and bonding quality of one of the composite materials is better, this becomes the material of interest of this chapter. Section 5.3 introduces the methods to determine the mechanical property anisotropy and how process variable settings affect this phenomenon. The experimental results were also compared to the material extrusion process simulation results, and they are discussed in this section.

5.2 Scanning Electron Microscope (SEM)

Although test specimens with polypropylene-based composite materials showed no significant differences in warpage with respect to each other, differences in surface finish were observed, which was related to the bonding between the extruded filaments. The surface topography of test specimen was examined for each composite material using a SEM. The two extreme cases of surface finish are shown in Figure 5.1. The topographies of the top surface and the cross section of the test specimens fabricated with Polypropylenes D2 and D1 are shown in Figures 5.1 a and b, respectively. The surface

finish and bonding quality of Polypropylene D2 were remarkable as all of the extruded filaments seemed to have coalesced. The lumps on the top surface indicated each extruded filament, but no voids were visible from the SEM image. In contrast, the surface finish and bonding quality of Polypropylene D1 were poor as each extruded filament could be distinguished in the SEM image and broke during SEM specimen preparation.

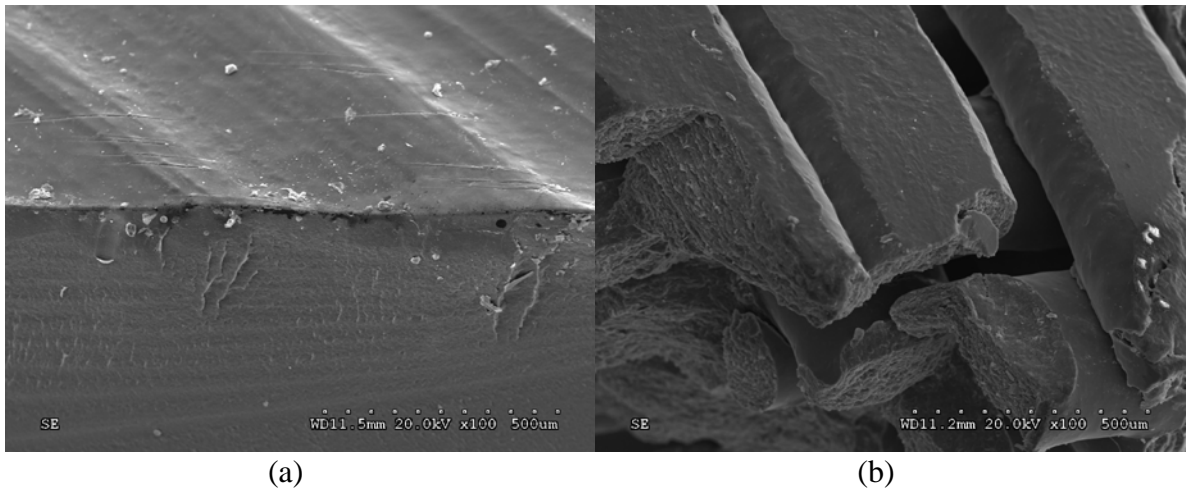


Figure 5.1 SEM images of (a) Polypropylene D2 and (b) Polypropylene D1

One of the disadvantages of material extrusion additive manufacturing is known to be the pronounced anisotropy of mechanical properties of fabricated parts that is caused by incomplete bonding between the extruded filaments as well as preferred orientation of polymer chains and crystals due to the imposed flow [30, 49]. However, no voids were observed in the test specimen fabricated with Polypropylene D2, which meant that a complete bonding was accomplished between the extruded filaments and a solid part was created. This suggested that anisotropy was perhaps reduced with this composite

material. In order to investigate this phenomenon further, tensile tests were conducted using Polypropylene D2.

5.3 Mechanical Property Anisotropy

Anisotropy is the property of being dependent on directions. Therefore, by producing tensile property data of Polypropylene D2 with different fill angles, the filament bonding performance can be tested and a reduction in anisotropy can be shown. Thin flat strips of material having a constant rectangular cross section were fabricated with two fill angles, 0° and 90° , and were tested following a method similar to ASTM D3039/D3039M-14 [50]. The 0° fill angle specimens were fabricated without perimeters, but the 90° fill angle specimens required three perimeters since the fabrication process was unsuccessful without them. The test specimen dimensions are shown in Figure 5.2, and the schematics of fill angles are shown in Figure 5.3. Five specimens were tested using Instron 5566 at a speed of 20 mm/min in order to produce failure within approximately 1 to 10 minutes.

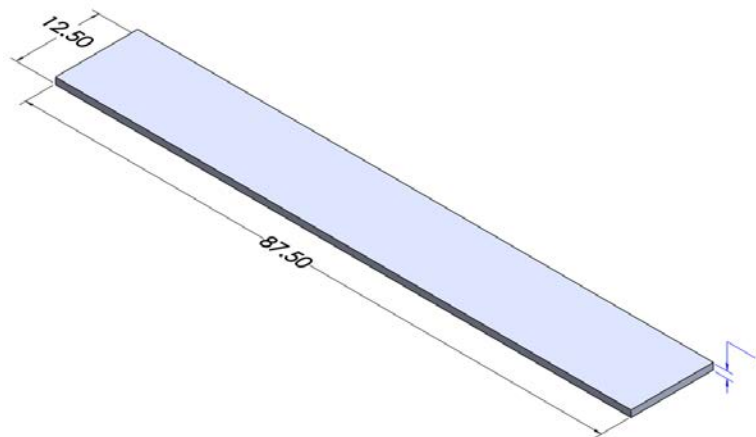


Figure 5.2 Anisotropy test specimen with dimensions (Units in mm)

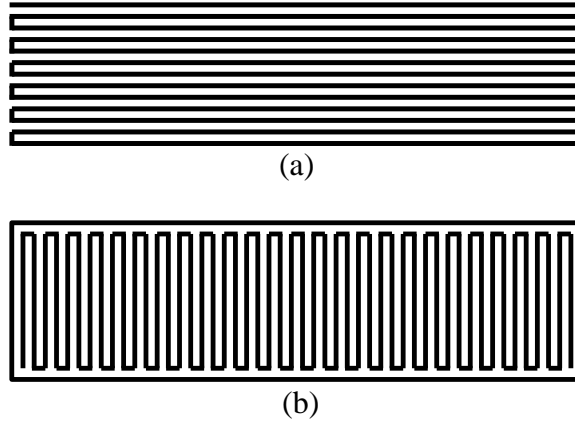


Figure 5.3 Anisotropy test specimens: (a) 0° fill angle and (b) 90° fill angle

Representative stress-strain curves with yield and filament failure points with 0° and 90° fill angles are shown in Figure 5.4 and Figure 5.5, respectively. Yield point was defined according to the testing standard as the first point on the stress-strain curve at which an increase in strain occurs without an increase in stress. The filament failure point was estimated to be the point where filaments began to fail during the test. Since these test specimens deformed differently over the entire length of the sample between the grips, the nominal strain was calculated and was used as the domain on the stress-strain curves. The nominal strain was calculated by dividing the crosshead extension by the distance between grips, which was 62.5 mm. It should be noted that the test specimens with a 0° fill angle never failed during this test. Instead, the specimens continued to extend until they were too thin for the Instron machine to grip.

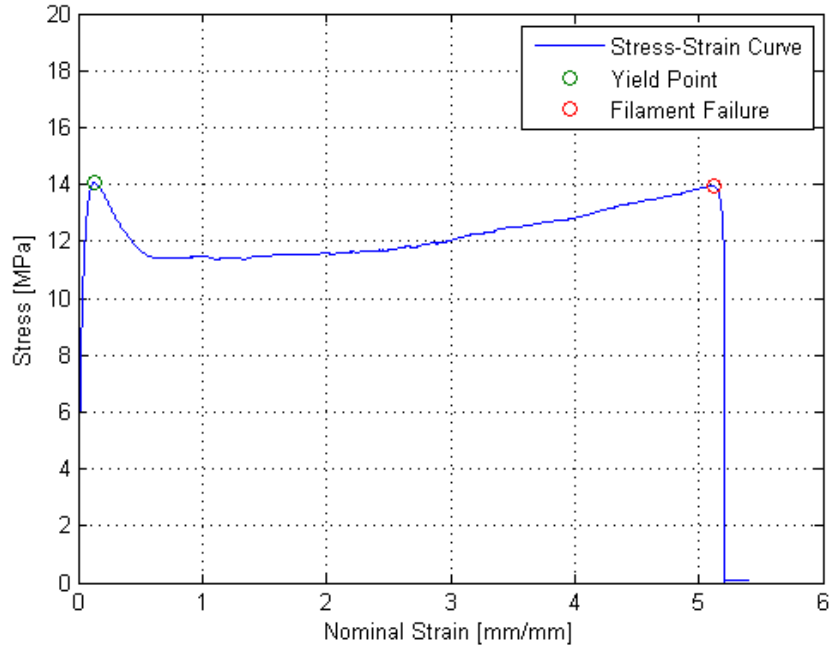


Figure 5.4 Stress-strain curve of Polypropylene D2 with a 0° fill angle

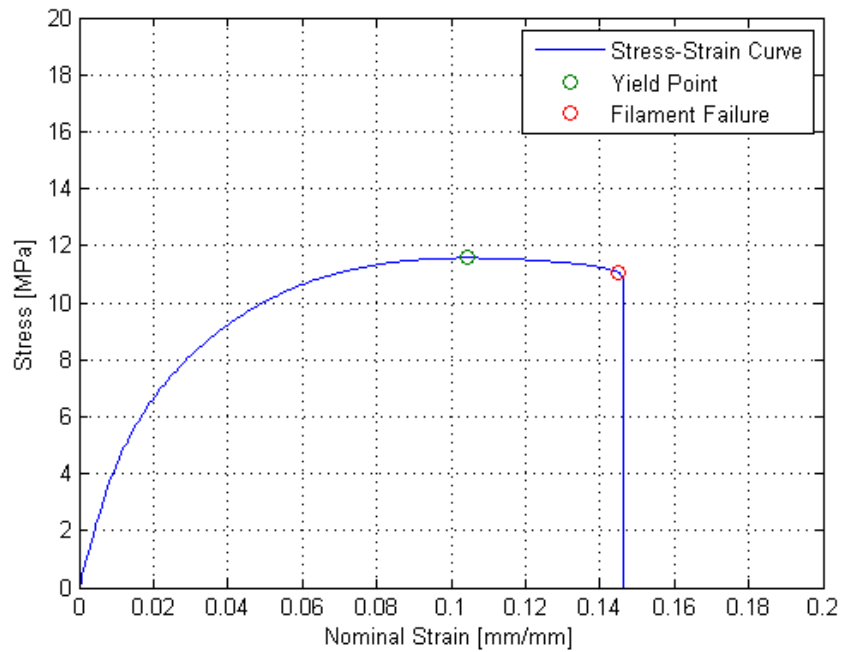


Figure 5.5 Stress-strain curve of Polypropylene D2 with a 90° fill angle

Various deposition temperatures and layer heights were also explored to see if these process variable settings affect mechanical property anisotropy and filament bonding performance. The settings are summarized in Table 5.1.

Table 5.1 Process variable settings for mechanical property anisotropy

Process Variable Settings	Values		
Deposition Temperature	240 °C	260 °C	280 °C
Layer Height	0.1 mm	0.2 mm	-

5.3.1 Deposition Temperature

From the stress-strain curves, tensile stress at yield point, tensile stress and nominal strain at filament failure point and modulus of elasticity were determined with various deposition temperatures, and are shown in Figure 5.6 through Figure 5.9, respectively. In this case, the layer height was kept constant at 0.2 mm. Since there were overlaps of the error bars, statistical analyses were performed on these experimental results. Single factor analysis of variance (ANOVA) was run to test the null hypothesis that the means are all equal. For all four plots, the means were determined to be statistically equal for each fill angle. Tensile stress, nominal strain and modulus of elasticity with a 0° fill angle were not dependent on temperature, and those with a 90° fill angle were not dependent on temperature.

The focus of this chapter is mechanical property anisotropy, so the tensile stresses with two different fill angles were also compared at each temperature. At 240 °C, the tensile stress at yield point was higher with a 0° fill angle than with a 90° fill angle,

which implied that anisotropy existed at this temperature. When the deposition temperature was increased to 260 °C and 280 °C, the tensile stresses at yield point were determined to be statistically equal. A similar trend was observed with the tensile stress at filament failure point in Figure 5.7. At 240 °C and 260 °C, the tensile stresses were higher with a 0° fill angle compared to a 90° fill angle. However, statistical analysis showed that they are equal at 280 °C. Therefore, a reduction in anisotropy was accomplished by increasing the deposition temperature. In addition, the typical value of tensile stress at yield point of Polypropylene D is 15.8 MPa. The experimental data showed that of Polypropylene D2 is slightly lower than the base polypropylene.

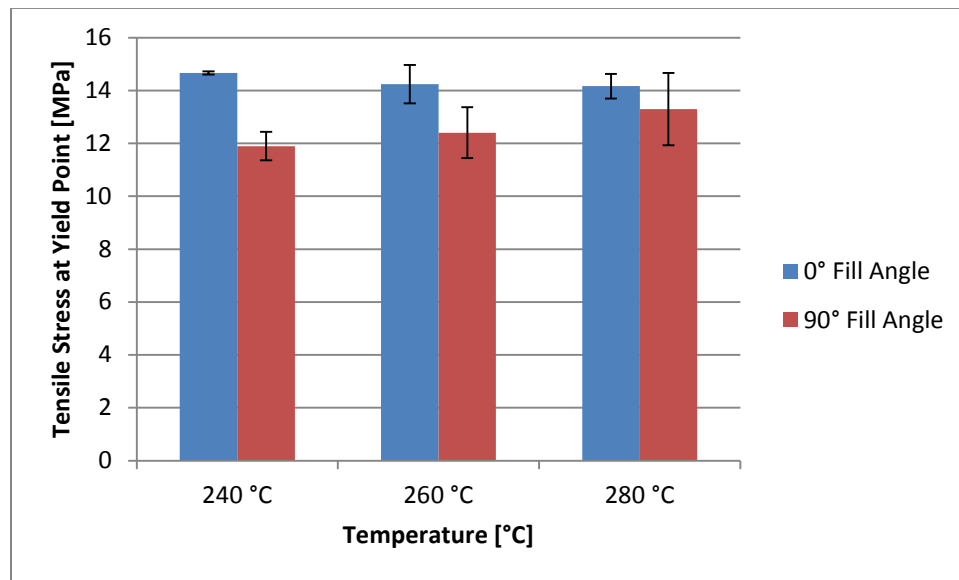


Figure 5.6 Tensile stress at yield point with various deposition temperatures

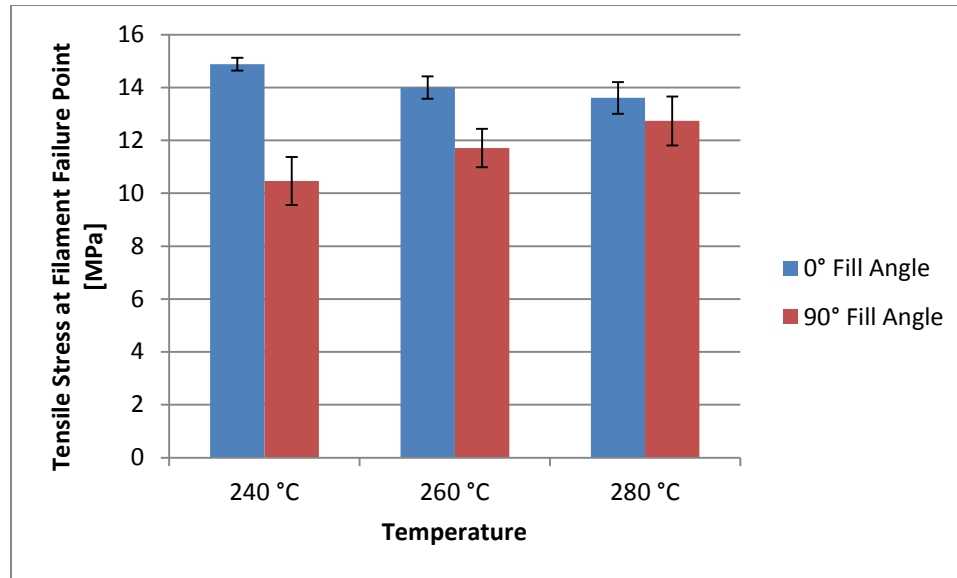


Figure 5.7 Tensile stress at filament failure point with various deposition temperatures

It can be observed from Figure 5.8 that tensile nominal strain at filament failure point is highly dependent on fill angle. The nominal strain with 0° fill angle was approximately 5.1 mm/mm, and that with 90° fill angle was approximately 0.2 mm/mm. Stratasys reported elongation results for ABS-M30 is 7% for 0° fill angle, while 90° fill angle exhibited elongation of only 2%. Although there are differences between the strain values, those with a 0° fill angle are significantly higher compared to those with a 90° fill angle. In addition, the typical value of elongation at break of Polypropylene D is reported to be 617%. The experimental data showed that of Polypropylene D2 with 0° fill angle is approximately 17% lower than the base polypropylene.

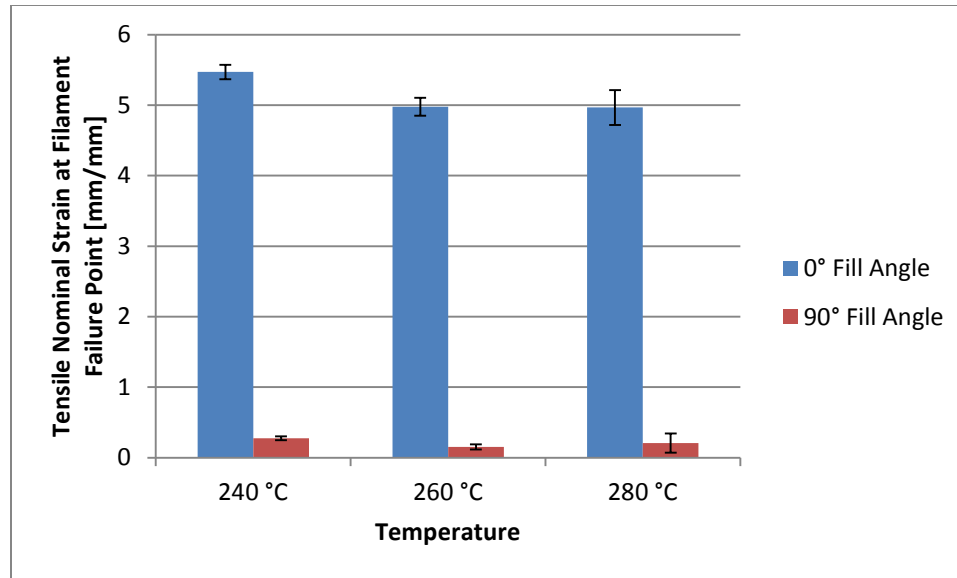


Figure 5.8 Tensile nominal strain at filament failure point with various deposition temperatures

Figure 5.9 shows that the modulus of elasticity is fairly uniform and is not dependent on fill angle, although tensile nominal strain at filament failure point is highly dependent on fill angle as previously stated. It was determined that the moduli of elasticity with different fill angles were statistically equal at each temperature as well. The modulus of elasticity was calculated from the stress-strain data in the elastic region as shown in Figure 5.4 and Figure 5.5. For test specimens with a 0° fill angle, a typical range of tensile stress in the elastic region was 2.7 and 6.5 MPa over the strain range of 0.005 and 0.015 mm/mm. For test specimens with a 90° fill angle, a typical range of tensile stress in the elastic region was 2.7 and 6.1 MPa over the strain range of 0.005 and 0.015 mm/mm. Both the tensile stress and strain ranges were similar in values, and the difference between the maximum stress values was 6.2%. These results validated that the modulus of elasticity was not dependent on fill angle. However, when the average values were compared, the modulus of elasticity with a 0° fill angle was approximately 383

MPa, and that with a 90° fill angle was approximately 357 MPa, which was a 7% decrease. These experimental data of fabricated test specimens were also compared to those prepared using compression molding. Type V dogbone-shaped test specimens were tested following procedures described in ASTM D638-14 [51]. The specimen geometry is shown in Figure 5.10. Five specimens were tested using an Instron 5566 at a speed of 20 mm/min. The modulus of elasticity of the molded test specimens was determined to be 413 ± 21 MPa, which was 7.8% higher than that of the fabricated test specimens with a 0° fill angle and 15.7% higher than that with a 90° fill angle. The differences seen are qualitatively similar to trends observed for ABS when comparing the mechanical properties of bulk specimens and printed parts. Stratasys reported the tensile modulus of ABS-M30 was 2,230 MPA for 0° fill angle, while 90° fill angle exhibited tensile modulus of 2,180 MPa, which was a 2% difference [36]. A typical value of modulus of elasticity of ABS was 2,300 MPa [52], which was also slightly higher than those reported by Stratasys for the printed parts.

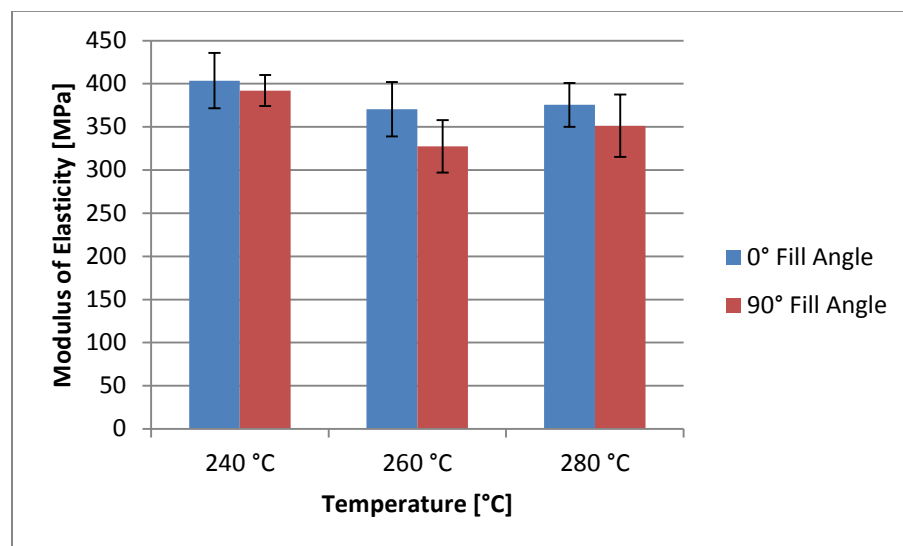


Figure 5.9 Modulus of elasticity with various deposition temperatures

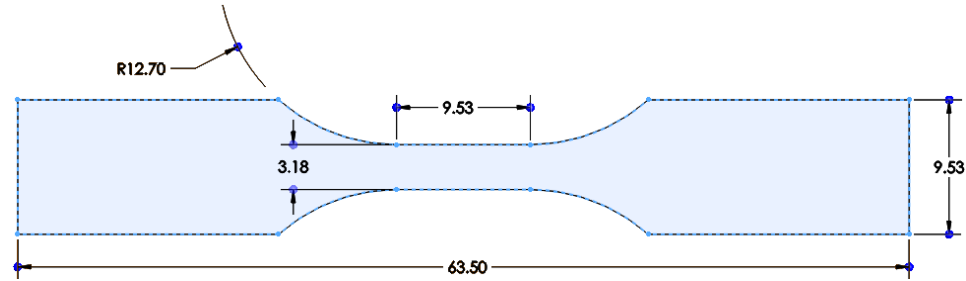


Figure 5.10 Type V test specimen dimensions (Units in mm)

Using the material extrusion process simulation models introduced in Section 4.2, the temperature distributions of two layers of filaments were determined and are shown in Figure 5.11. The difference in fill angles was simulated by changing the deposition length. In order for the deposition length to be directly proportional to the anisotropy test specimen dimensions shown in Figure 5.2, it was set to 5.0 mm for 0° fill angle and 0.7 mm for 90° fill angle. The temperature contour plots are shown in two colors only, in which green represents below melting temperature (108°C) and red represents above melting temperature. In all cases, the temperature at the interface between the first and second layers is above melting temperature, which means that good bonding is achieved. In addition, no significant differences in the contour plots can be observed at different temperatures. This agrees with the experimental results that tensile stress, nominal strain and modulus of elasticity were not dependent on temperature.

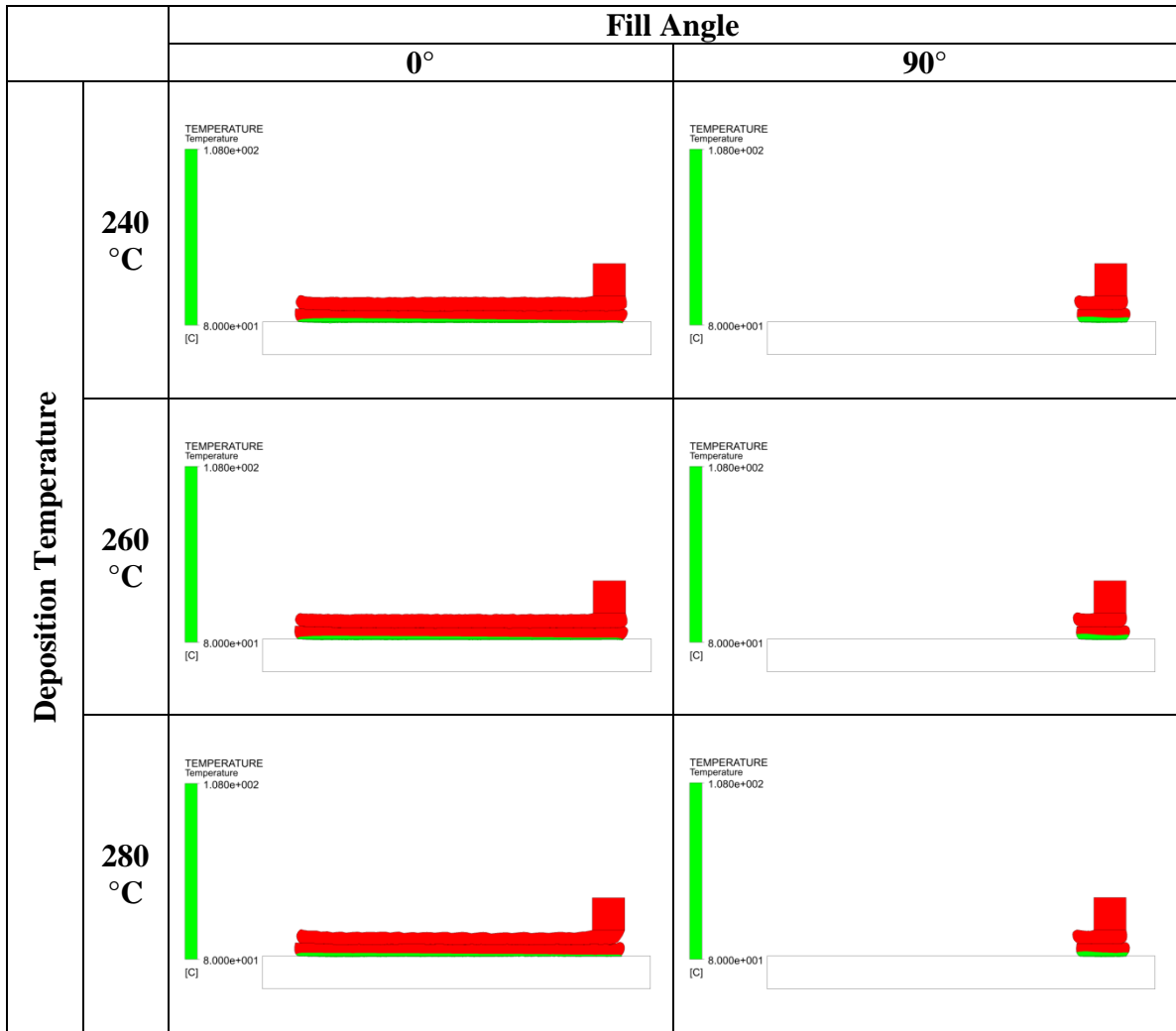


Figure 5.11 Temperature distributions from process simulation models with various fill angles and deposition temperatures

5.3.2 Layer Height

Tensile stress at yield point, tensile stress and nominal strain at filament failure point and modulus of elasticity were determined with various layer heights, and are shown in Figure 5.12 through Figure 5.15, respectively. In this case, the deposition temperature was kept constant at 260 °C. Statistical analyses were performed on these experimental results as well due to the error bar overlaps. For all four plots, the means

were determined to be statistically equal for the 0° fill angle. However, for all four plots, the means were determined to be statistically not equal for the 90° fill angle. In fact, the values with a layer height of 0.1 mm were determined to be higher than those with a layer height of 0.2 mm in all cases. Tensile stress, nominal strain and modulus of elasticity with a 0° fill angle were not dependent on layer height, but those with a 90° fill angle were dependent on layer height.

The tensile stresses with two different fill angles were also compared at each layer height. From the experimental results shown in Figure 5.12, the tensile stresses at yield point with a layer height of 0.1 mm were statistically equal, and those with a layer height of 0.2 mm were statistically equal. The same trend was observed with the tensile stresses at filament failure point, which implied that statistical anisotropy did not exist at each layer height. However, slightly larger differences in the average tensile stress values were observed with a 0.2 mm layer height from the two plots. Therefore, a reduction in anisotropy was perhaps accomplished by decreasing the layer height.

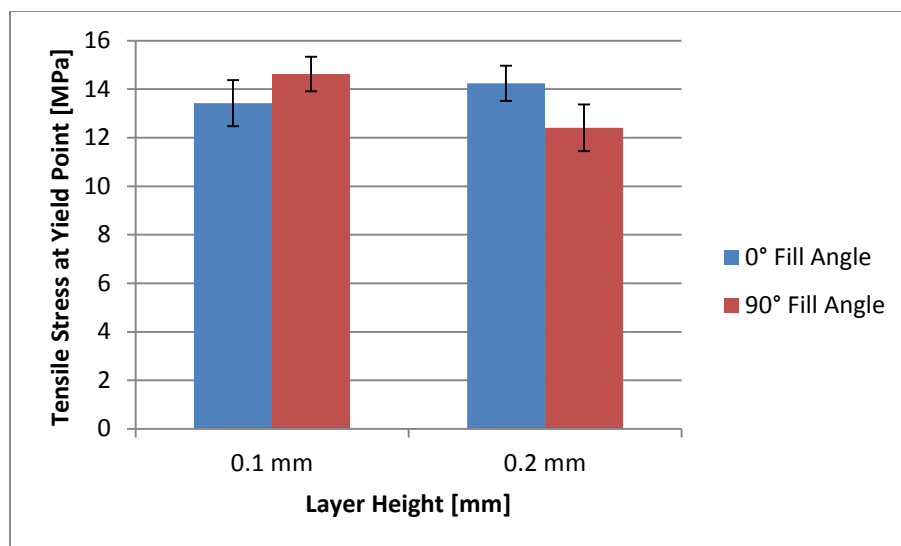


Figure 5.12 Tensile stress at yield point with various layer heights

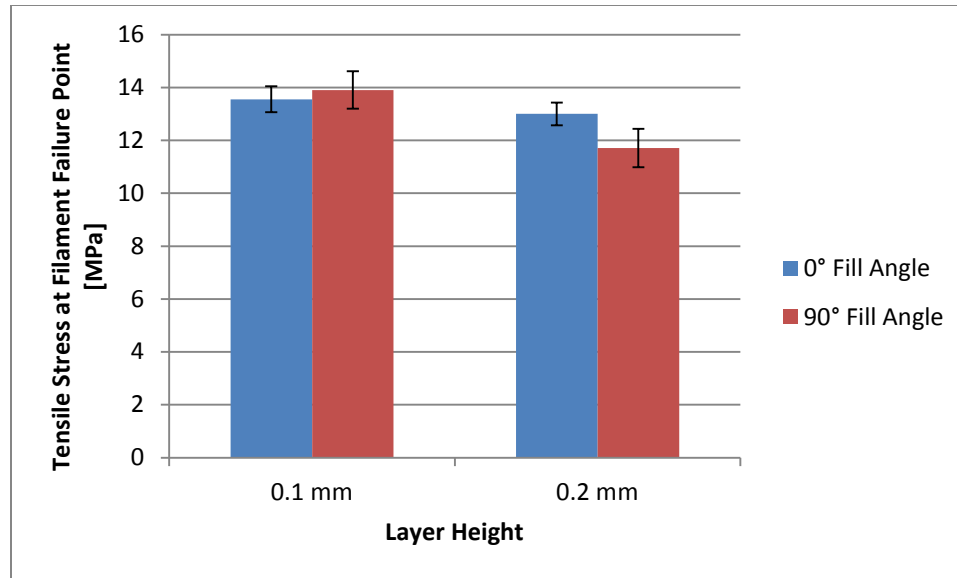


Figure 5.13 Tensile stress at filament failure point with various layer heights

It can be observed from Figure 5.14 that tensile nominal strain at filament failure point is highly dependent on fill angle. Although the nominal strains for the 0° fill angle specimens were higher than those for the 90° fill angle for both layer heights, the value with a 0.1 mm layer height was significantly higher than that with a 0.2 mm layer height for the 90° fill angle specimens. This indicated that a reduction in anisotropy in nominal strain was achieved by decreasing the layer height.

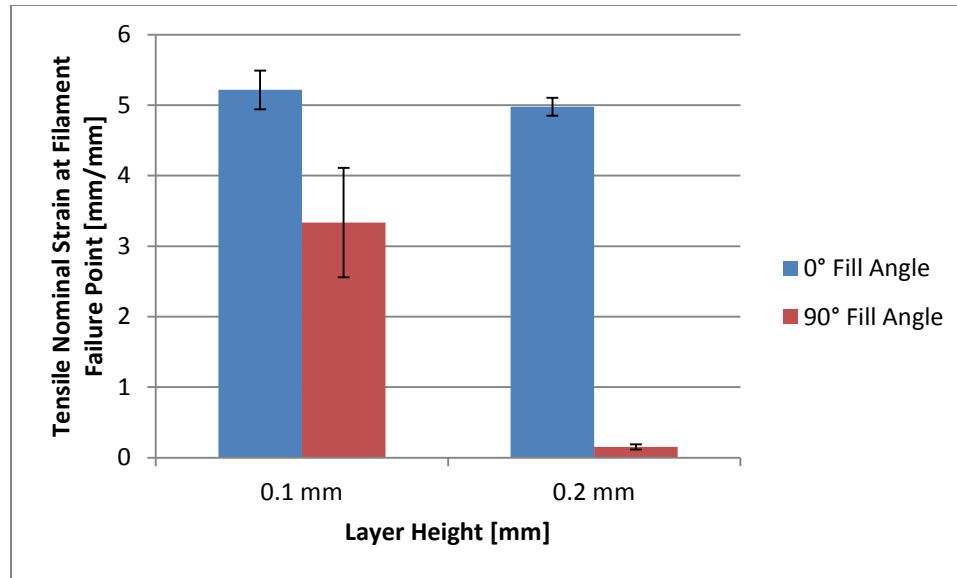


Figure 5.14 Tensile nominal strain at filament failure point with various layer heights

The moduli of elasticity with two different fill angles were compared at each layer height. From the experimental results shown in Figure 5.15, the moduli of elasticity with a layer height of 0.1 mm were statistically equal, and those with a layer height of 0.2 mm were statistically equal. This suggested that the modulus of elasticity was fairly uniform and was not dependent on fill angle. However, once again, the difference between the average modulus of elasticity with a 0.2 mm layer height was larger compared to that with a 0.1 mm layer height. This supported the hypothesis that anisotropy could be reduced with a lower layer height.

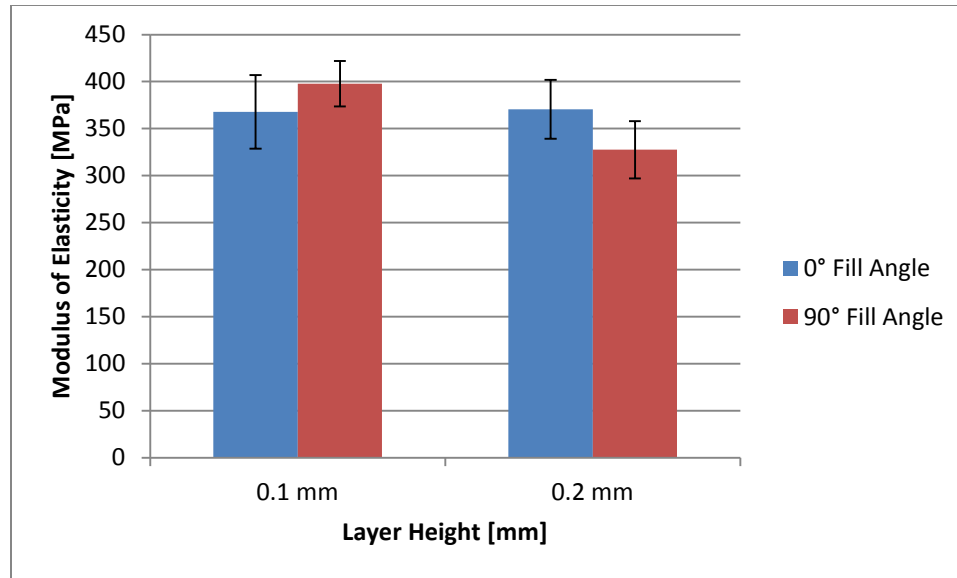


Figure 5.15 Modulus of elasticity with various layer heights

The temperature distributions of two layers of filaments with different layer height values were determined from the process simulation models, and the results are shown in Figure 5.16. As it was stated previously, the green region of the contour plot represented below melting temperature (108 °C) and the red region represented above melting temperature. Since the number of layers was kept constant, this led to differences in part thickness. Therefore, when comparing the red region in the vertical direction, the results needed to be normalized to the part thickness. It was determined that a larger percentage of the thickness was at a higher temperature with a lower layer height. This meant that a greater portion of the first layer with a 0.1 mm layer height was re-liquefied and a better diffusion across the interface was obtained. It can be concluded that a better bonding was achieved with filaments with a lower layer height. This agreed with the experimental results that tensile stress, nominal strain and modulus of elasticity with a layer height of 0.1 mm were higher than those with a layer height of 0.2 mm for the 90°

fill angle specimens. It can also be observed from Figure 5.16 that there is a large green region for the 0° fill angle specimen with a layer height of 0.1 mm. This was most likely due to this specimen being thinner than the specimen with a layer height of 0.2 mm. The simulation result indicated that the green region had cooled down at this instant but a good bonding between the layers had already been achieved as it can be observed from the red region in the current time step.

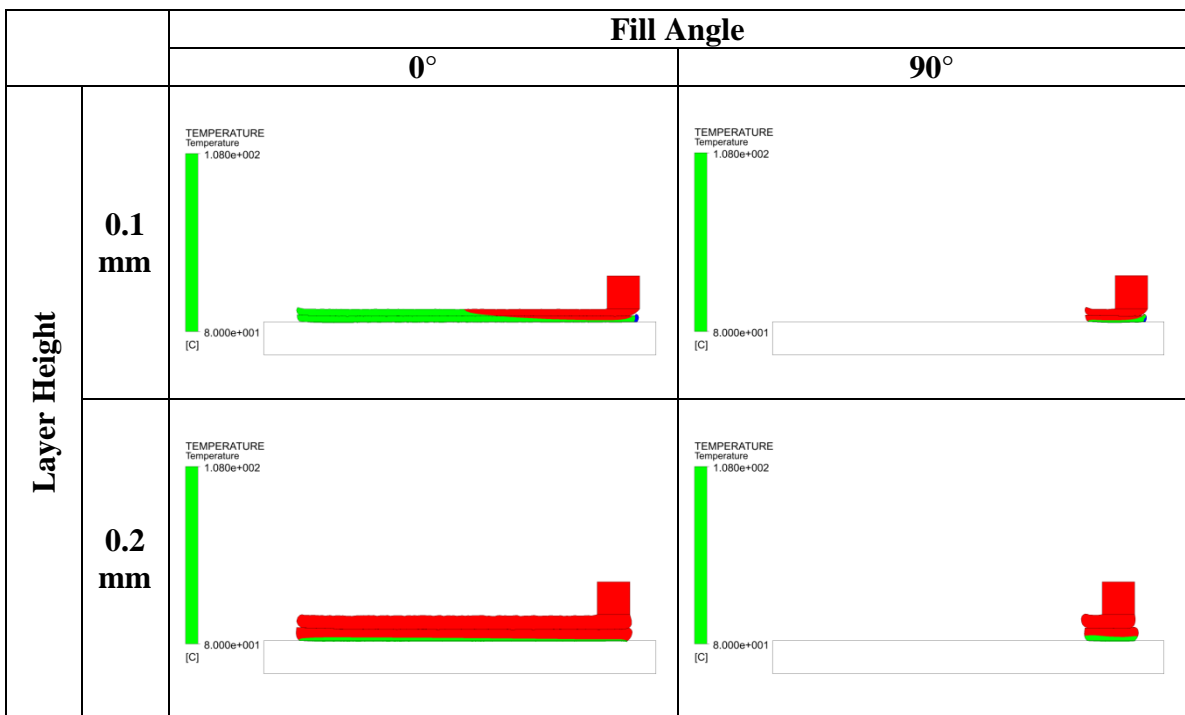


Figure 5.16 Temperature distributions from process simulation models with various fill angles and deposition temperatures

5.4 Summary

Polypropylene D2 was selected as the material of interest for the mechanical property anisotropy study due to its remarkable surface finish and bonding quality

observed from the SEM images. The 0° and 90° fill angle test specimens were fabricated with various deposition temperatures and layer heights. By producing tensile property data of Polypropylene D2, its mechanical property anisotropy and filament bonding performance were compared. Tensile stress, nominal strain and modulus of elasticity were not dependent on temperature with both the 0° and 90° fill angle specimens. However, it was determined that anisotropy in tensile stress is reduced by increasing the deposition temperature. In addition, the tensile properties were not dependent on layer height with the 0° fill angle specimens, but they were dependent on layer height with the 90° fill angle specimens. The experimental results also showed that anisotropy in tensile properties is reduced by decreasing the layer height. The comparisons between the experimental results and process simulation results were discussed as well. It was observed that there is a larger region with higher temperature in the vertical direction with a smaller layer height. This likely leads to reduced mechanical property anisotropy due to better bonding between the extruded filaments.

CHAPTER 6

CLOSURE AND CONTRIBUTIONS

6.1 Introduction

Chapter 6 is the concluding chapter of this thesis. Section 6.2 reviews the research questions and hypotheses presented in Chapter 1. Section 6.3 presents the contributions resulting from this thesis. Section 6.4 outlines the suggestions for future work.

6.2 Answering the Research Questions

The objective of this thesis was to investigate the capability of polypropylene-based polymers in material extrusion additive manufacturing, computationally and experimentally, to support the advancements in developing new material formulations and reducing the cost of existing material productions. Material extrusion process simulation models were developed in order to be able to examine both the quality and performance of fabricated parts, such as warpage and mechanical property anisotropy, respectively. These process simulation models are capable of predicting the temperature distributions, deposited filament shapes, residual stresses and warpages of fabricated parts. In order to achieve this objective, this thesis sought to answer two research questions.

6.2.1 Research Question 1

The first research question that was addressed in this thesis was as follows:

Research Question 1:

Which process variable settings on material extrusion additive manufacturing machines and material properties of polypropylene-based composite materials affect the warpage and deformation characteristics of the fabricated parts?

Hypothesis 1:

By developing material extrusion process simulation models, the correlations between process variable settings and material properties, and warpage and deformation characteristics can be determined.

Two-dimensional material extrusion process simulation models that can be exercised on process variable settings and new material formulations were developed using ANSYS® Polyflow and Mechanical and were presented in Chapter 4. The material extrusion process was divided up into six stages: melt flow in the liquefier chamber, extrusion through the nozzle, die swell at the nozzle exit, first layer deposition and cooling, second layer deposition and two-layer cooling and warpage. A process simulation model was developed in each stage, and the sequential simulation models were linked to one another through the temperature profiles developed in previous stages. All of these process simulation models were validated by comparisons with analytical models, experimental data and literature results.

The correlations between process variable settings and material properties on part warpage were determined by conducting parametric studies of the warpage simulation model. The process variable settings that were selected for the parametric studies were deposition temperature, deposition speed and layer height. The results showed that varying the deposition temperature within a representative range of material extrusion

process did not have a significant effect on part warpage. However, part warpage decreased as both deposition speed and layer height increased. The material properties that were selected for the parametric studies were coefficient of thermal expansion and thermal conductivity. The results showed that part warpage decreased as coefficient of thermal expansion decreased and as thermal conductivity increased. In conclusion, process variable settings and material properties that affect part warpage were indeed determined from the process simulation models. The first research question has been answered and the hypothesis was validated.

6.2.2 Research Question 2

The second research question that was addressed in this thesis was as follows:

Research Question 2:

Which process variable settings on material extrusion additive manufacturing machines affect the bonding quality of the extruded filaments?

Hypothesis 2:

Producing tensile property data of fabricated parts with different fill angles will allow mechanical property anisotropy and filament bonding performance to be correlated. The experimental results are compared to process simulation model results to determine the models' efficacy.

The tensile test specimens with 0° and 90° fill angles were fabricated with various process variable settings, and tensile property data were produced. The process variable settings that were investigated to determine if they affect mechanical property anisotropy and filament bonding performance were deposition temperature and layer height. Tensile stress, nominal strain and modulus of elasticity were not dependent on temperature with both the 0° and 90° fill angle specimens. However, a reduction in tensile stress anisotropy was achieved with an increase in deposition temperature. In addition, the tensile properties with a 0° fill angle test specimens were not dependent on layer height, but those with a 90° fill angle test specimens were dependent on layer height. The experimental results also showed that a reduction in tensile property anisotropy was accomplished with a decrease in layer height.

The experimental results were compared to the simulation model results as well. The temperature contour plots from the simulation models at various deposition temperatures depicted no significant differences, which agreed with the experimental results that tensile properties were not dependent on temperature. In addition, the temperature contour plots from the simulation models with various layer heights showed that there is a greater region with higher temperature in the vertical direction with a lower layer height. This represented that a better bonding was achieved between the extruded filaments with a lower layer height, which leads to a reduction in mechanical property anisotropy. This agreed with the experimental results that tensile properties with a lower layer height were higher than those with a higher layer height for the 90° fill angle specimens. In conclusion, process variable settings that affect the filament bonding quality were indeed determined by producing tensile property data with 0° and 90° fill

angle test specimens. The second research question has been answered and the hypothesis was validated.

6.3 Contributions

The primary contribution of this thesis is the development of material extrusion process simulation models that are capable of predicting temperature distributions, deposited filament shapes, residual stresses and warpages of fabricated parts. Although polypropylene is inexpensive compared to materials that are currently being used in material extrusion additive manufacturing, the fabricated parts with polypropylene have tendencies to warp. An alternative to reduce warpage is to create polypropylene-based composite materials by combining polypropylene with additives. This will also support the advancements in developing new material formulations, while reducing the cost of existing material productions. However, computational methods are required in order to avoid the iterative experiments of creating new materials. The process simulation models developed and presented in this thesis are beneficial in this case since they can be exercised on new material formulations to determine the part warpage without actually creating the new materials. In addition, these models can be utilized to explore the trade-offs among the objectives, such as part warpages and mechanical properties, to identify a favorable combination of process variable settings and materials properties. For example, from this research, it was concluded that an increase in layer height led to a reduction in part warpage, but a decrease in layer height led to a reduction in anisotropy and a better filament bonding quality. The process variable settings are limited on additive manufacturing machines, whereas they are not limited on simulation models. Therefore,

it is possible to explore various combinations of the simulation model inputs until desired objectives are achieved. All of the proposed process simulation models were also validated by comparisons with analytical models, experiments and literature results, and they provided promising results as the basis for screening new materials computationally.

6.4 Future Work

The following directions for future work have been identified.

The material extrusion process simulation models presented in this thesis could be investigated further to develop a model that is capable of predicting the mechanical properties of the fabricated parts, such as tensile and flexural properties. In order to accomplish this, an intermediate step of predicting the filament bond strength is necessary. An early stage of investigating and correlating mechanical property anisotropy and filament bonding quality was presented in Chapter 5 of this thesis, which might be beneficial when relating the bond strengths to mechanical properties. In addition, the mechanical property simulation model would be validated by conducting mechanical testing of fabricated parts on Instron machines.

Another suggestion for future work is to convert all of the process simulation models presented in this thesis to three-dimensional simulation models. Currently, the models are two-dimensional and only simple filament extrusions can be simulated. Although unique geometries and features could be simulated with three-dimensional models, the two-dimensional process models are already very computationally intensive, and this will be worsen with three-dimensional models.

REFERENCES

1. Gibson, I., D.W. Rosen, and B. Stucker, *Additive Manufacturing Technologies: Rapid Prototyping to Direct Digital Manufacturing*. 2010, New York, NY: Springer. 459.
2. *Align Technology, Inc.* 2000 [cited 2014 November]; Available from: <http://www.aligntech.com/>.
3. *Siemens Hearing Aids, Wireless Accessories & Other Products*. 2016 [cited 2014 November]; Available from: <https://usa.bestsoundtechnology.com/siemens-hearing-products/>.
4. Turner, B.N., R. Strong, and S.A. Gold, *A Review of Melt Extrusion Additive Manufacturing Processes: I. Process Design and Modeling*. *Rapid Prototyping Journal*, 2014. **20**(3): p. 192-204.
5. *Stratasys FDM Technology*. 2016 [cited 2014 September 28]; Available from: <http://www.stratasys.com/3d-printers/technologies/fdm-technology>.
6. *All3DP: 28 Great 3D Printer Filament Types (A Guide)*. 2016 [cited 2016 September 18]; Available from: <https://all3dp.com/best-3d-printer-filament-types-pla-abs-pet-exotic-wood-metal/>.
7. *HYREL System 30*. 2014 [cited 2014 December]; Available from: <http://www.hyrel3d.com/>.
8. Fischer, F., *Thermoplastics: The Strongest Choice for 3D Printing*, 2015: Eden Prairie, MN. p. 1-12.
9. *Stratasys: FDM Thermoplastics*. 2016 [cited 2015 April 10]; Available from: <http://www.stratasys.com/materials/fdm>.
10. Novakova-Marcincinova, L. and I. Kuric, *Basic and Advanced Materials for Fused Deposition Modeling Rapid Prototyping Technology*. *Manuf. and Ind. Eng.*, 2012. **11**(1): p. 24-27.

11. *3D Printer Filament Types Overview*. 2016 [cited 2016 August 10]; Available from: <http://3dprintingfromscratch.com/common/3d-printer-filament-types-overview/#pet>.
12. *3D Printer Filament Comparison Guide*. 2016 [cited 2016 August 10]; Available from: <https://www.matterhackers.com/3d-printer-filament-compare>.
13. *Plastics Resin Pricing*. 2016 [cited 2016 September 22]; Available from: <http://www.plasticsnews.com/resin/>.
14. Lin, C.B. *High Polymer Prices Make PLA an Attractive Alternative - NatureWorks*. ICIS News, 2011.
15. Grande, J.A., *Biopolymers Strive to Meet Price/Performance Challenge*, in *Plastics Technology*2007, Gardner Business Media, Inc.: Cincinnati, Ohio.
16. Schut, J.H., *Starting Up: Resin Prices Bottom Out*, in *Plastics Technology*2009, Gardner Business Media, Inc.: Cincinnati, Ohio.
17. *ULTEM PEI Filament*. 3DXTech 2016 [cited 2016 September]; Available from: <http://www.3dxtech.com/ultem-pei-filament/>.
18. *Acrylonitrile Styrene Acrylate (ASA)*. ResMart 2014 [cited 2016 September]; Available from: <http://www.resmart.com/our-products/asa.html>.
19. *E3D Premium - Acrylic PMMA*. E3D-Online Limited 2014 [cited 2016 September]; Available from: <http://e3d-online.com/All-Filament/F-E3D-175-PMMA-CLEAR>.
20. *FlexiFil*. Formfutura 2016 [cited 2016 September]; Available from: <http://www.formfutura.com/formfutura-175mm-flexifil-white.html>.
21. *Engineering Plastics - Nylon's, Acetal & Delrin*. 2014 [cited 2016 September]; Available from: <http://www.bayplastics.co.uk/engineeringplastics.htm>.
22. Covert, A. *3-D Printing 'Ink' is Way Too Expensive*. CNN Money, 2014.

23. Karian, H.G., *Handbook of Polypropylene and Polypropylene Composites*. Second ed. 2003, New York, NY: Marcel Dekker, Inc. 741.
24. Strong, A.B., *Plastics: Materials and Processing*. 2000, Upper Saddle River, New Jersey: Prentice Hall. 811.
25. *Shrinkage Values for Miscellaneous Resins*. [cited 2015 April 27]; Available from: <http://www.stelray.com/reference-tables.html>.
26. Love, L.J., et al., *The Importance of Carbon Fiber to Polymer Additive Manufacturing*. *Journal of Materials Research*, 2014. **29**(17): p. 1893-1898.
27. Agarwala, M.K., et al., *Structural Quality of Parts Processed by Fused Deposition*. *Rapid Prototyping Journal*, 1996. **2**(4): p. 4-19.
28. Bellini, A., S. Guceri, and M. Bertoldi, *Liquefier Dynamics in Fused Deposition*. *Journal of Manufacturing Science and Engineering*, 2004. **126**(2): p. 237-246.
29. Bellini, A., *Fused Deposition of Ceramics: A Comprehensive Experimental, Analytical and Computational Study of Material Behavior, Fabrication Process and Equipment Design*, 2002, Drexel University. p. 297.
30. Sun, Q., et al., *Effect of Processing Conditions on the Bonding Quality of FDM Polymer Filaments*. *Rapid Prototyping Journal*, 2008. **14**(2): p. 72-80.
31. Crockett, R.S. and P.D. Calvert. *The Liquid-to-Solid Transition in Stereodeposition Techniques*. in *Solid Freeform Fabrication Symposium*. 1996. Austin, TX.
32. Yardimci, M.A. and S. Guceri, *Conceptual Framework for the Thermal Process Modelling of Fused Deposition*. *Rapid Prototyping Journal*, 1996. **2**(2): p. 26-31.
33. Rodriguez, J.F., J.P. Thomas, and J.E. Renaud, *Mechanical Behavior of Acrylonitrile Butadiene Styrene (ABS) Fused Deposition Materials: Experimental Investigation*. *Rapid Prototyping Journal*, 2001. **7**(3): p. 148-158.

34. Rodriguez, J.F., J.P. Thomas, and J.E. Renaud, *Characterization of the Mesostucture of Fused-Deposition Acrylonitrile-Butadiene-Styrene Materials*. Rapid Prototyping Journal, 2000. **6**(3): p. 175-185.
35. Durgun, I. and R. Ertan, *Experimental Investigation of FDM Process for Improvement of Mechanical Properties and Production Cost*. Rapid Prototyping Journal, 2014. **20**(3): p. 228-235.
36. *Stratasys ABS-M30*. 2016 [cited 2015 May 27]; Available from: <http://www.stratasys.com/materials/fdm/abs-m30>.
37. Shenoy, A.V., *Rheology of Filled Polymer Systems*. 1999, Dordrecht, The Netherlands: Kluwer Academic Publishers. 475.
38. *Capillary Rheometer (LCR7000 Series)*. Dynisco 2016 [cited 2015 April]; Available from: <http://www.dynisco.com/capillary-rheometer-lcr-7000-series->.
39. *L75 PT Vertical Dilatometer*. Linseis Thermal Analysis 2012 [cited 2016 September]; Available from: <http://www.linseis.com/en/our-products/dilatometer/l75-pt-vertical/>.
40. *Standard Test Method for Linear Thermal Expansion of Solid Materials With a Push-Rod Dilatometer*, 2011, ASTM International: West Conshohocken, PA. p. 1-9.
41. *Hot Disk Sensors for Thermal Conductivity Measurements*. 2015 [cited 2016 January 14]; Available from: <http://www.hotdiskinstruments.com/products/sensors-for-thermal-conductivity-measurements.html>.
42. Mark, J.E., *Polymer Data Handbook*. Polypropylene, Isotactic, ed. D.V. Howe and A. Dimeska. 2009, New York: Oxford University Press. 1250.
43. Spakovszky, Z.S. *Heat Exchangers*. Thermodynamics 2008 [cited 2015 November]; Available from: <http://web.mit.edu/16.unified/www/FALL/thermodynamics/notes/node131.html>.

44. *Critical Surface Tension and Contact Angle with Water for Various Polymers*. [cited 2015 May 8]; Available from: http://www.accudynetest.com/polytable_03.html.
45. Incropera, F.P. and D.P. DeWitt, *Introduction to Heat Transfer*. 3rd ed. 1996, New York: John Wiley & Sons.
46. Tanner, R.I., *A Theory of Die-Swell*. *Journal of Polymer Science*, 1970. **8**: p. 2067-2078.
47. Dinwiddie, R.B., et al. *Infrared Imaging of the Polymer 3D-Printing Process*. in *SPIE*. 2014. Baltimore, Maryland.
48. *Starrett Optical Comparators*. HB400 Horizontal Benchtop Optical Comparator [cited 2016 December 1]; Available from: <http://www.starrett.com/metrology/product-detail/metrology/metrology-products/metrology-equipment/optical-comparators/HB400>.
49. Schrauwen, B.A.G., et al., *Structure, Deformation, and Failure of Flow-Oriented Semicrystalline Polymers*. *Macromolecules*, 2004. **37**(23): p. 8616-8633.
50. *Standard Test Method for Tensile Properties of Polymer Matrix Composite Materials*, 2014, ASTM International: West Conshohocken, PA. p. 1-13.
51. *Standard Test Method for Tensile Properties of Plastics*, 2014, ASTM International: West Conshohocken, PA. p. 1-17.
52. *Tensile Property Testing of Plastics*. 1996 [cited 2015; Available from: <http://www.matweb.com/reference/tensilestrength.aspx>.